Polarization-Resolved, Oblique Incidence Terahertz Spectroscopy of Highly Uniform 2D Hybrid Perovskite Films

Thesis by
Kyle Virgil

In Partial Fulfillment of the Requirements for
the degree of
Doctor of Philosophy

CALIFORNIA INSTITUTE OF TECHNOLOGY
Pasadena, California

2024
(Defended August 28, 2023)

ACKNOWLEDGEMENTS

ABSTRACT

This thesis details the development and optimization of thin film THz transmission measurements to extract spectrally resolved vibrational anisotropy in high quality layered hybrid perovskite materials. After an introduction in Chapter 1, Chapter 2 details the design, construction, and characterization of a terahertz time-domain spectrometer from scratch. Generalized THz propagation models are presented which enable accurate and diverse implementation of THz analysis. In Chapter 3, hybrid perovskite materials are introduced and our efforts towards reliably synthesizing high quality thin film perovskites using spin coating techniques are discussed. We find that optimized thin films are achieved from tailored synthetic conditions which depend on perovskite composition. In Chapter 4, we present our investigation into the elusive yet highly influential THz vibrational properties of 2D hybrid perovskite systems. A novel implementation of oblique-incidence THz transmission measurements reveals previously unseen vibrational excitations which provide valuable insight into the fundamental photodynamics that govern perovskite optoelectronics. We conclude in Chapter 5. This thesis serves to enhance the accessibility of powerful THz spectroscopic techniques as well as support the realization of promising perovskite renewable energy technologies.

TABLE OF CONTENTS

C h a p t e r   1

INTRODUCTION

The fascinating world of organohalide perovskite materials has captured the imagination of scientists and engineers alike, permeating myriad facets of research in science and engineering, and promising to shape the future of technology. As a versatile class of compounds, perovskites have proven their indispensability in a range of applications.[1-5] With their distinctive crystal structure and remarkable optoelectronic properties, organohalide perovskites have garnered widespread attention as a cornerstone of innovative advancements. Among their diverse derivatives, hybrid perovskites have emerged as a particularly compelling avenue of exploration, ushering in new perspectives at the intersection of light-matter interactions and fundamental charge behaviors.

Deeply embedded in these new perspectives is the intriguing realm of terahertz (THz) energy dynamics — a domain that has shown to intricately modulate the charge transport and electronic properties of hybrid perovskite semiconductors. The ever-evolving landscape of technology demands a thorough understanding of the fundamental mechanisms underlying these materials, which is precisely where terahertz time-domain spectroscopy (THz-TDS) emerges as a pivotal analytical tool. This thesis endeavors to unravel the intricate terahertz excitations in materials known as 2D hybrid perovskite semiconductors, paving the way for crucial photodynamic advancements to guide future design.

Electromagnetic Spectrum

| 1 GHz | 300 GHz | 30 THz | 384 THz | 789 THz | 30 PHz | 30 EHz |
| 0.3 m | 1 mm | 10 μm | 780 nm | 380 nm | 10 nm | 10 pm |

λ

Radio | Microwave | **Terahertz** | Infrared | Visible | Ultraviolet | X-Ray | Gamma-Ray

$10 - 1000 \text{ cm}^{-1}$
$1.24 - 124 \text{ meV}$
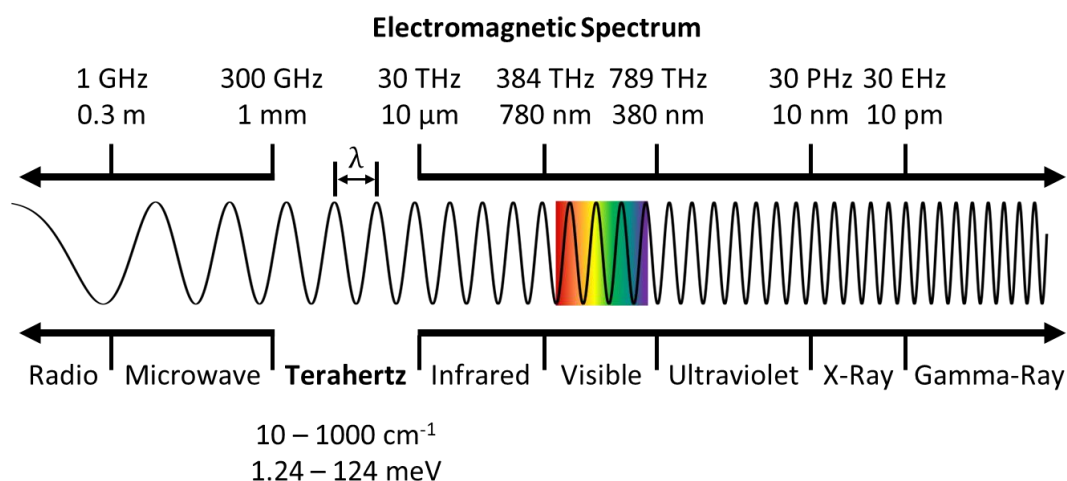
Figure 1. Representative overview of the electromagnetic spectrum.

Terahertz photons possess a unique ability to interact with a variety of materials and molecular vibrations, making their use a powerful tool for studying both the structural and dynamic properties of matter.[6-10] Terahertz time-domain spectroscopy exploits the properties of THz energy to study the interaction between materials and electromagnetic waves, providing windows into their composition, crystalline structures, and charge carrier behaviors. This spectral region holds great potential for technological applications such as imaging, sensing, communication, and material characterization, and it plays a pivotal role in revealing hidden dynamics within materials such as hybrid perovskite semiconductors.

In the chapters that follow, this thesis delves into the construction of a Blake lab femtosecond terahertz spectrometer that is used to characterize elusive vibrational properties of hybrid perovskite semiconductors fabricated in the Atwater lab. A novel implementation of oblique incidence terahertz transmission in high quality thin film

perovskites elucidates previously unknown anisotropic behavior that holds direct implications for phonon coupling. This thesis simultaneously serves to expand the capability of oblique incidence THz spectroscopy for sensitive material characterization and to support the development of perovskite optoelectronics through insights into their phononic behavior.

CHAPTER 1 BIBLIOGRAPHY

1. Mitzi, D. B. Introduction: Perovskites. *Chem. Rev.* **2019**, *119* (5), 3033–3035. https://doi.org/10.1021/acs.chemrev.8b00800.

2. Ortega-San-Martin, L. Introduction to Perovskites: A Historical Perspective; Arul, N. S., Nithya, V. D., Eds.; Materials Horizons: From Nature to Nanomaterials; *Springer Singapore: Singapore* **2020**, 1–41. https://doi.org/10.1007/978-981-15-1267-4_1.

3. Magnetic Perovskites: Synthesis, Structure and Physical Properties Asish K. Kundu. *MRS Bull.* **2016**, *41* (12), 1018–1020. https://doi.org/10.1557/mrs.2016.289.

4. Wu, G.; Liang, R.; Zhang, Z.; Ge, M.; Xing, G.; Sun, G. 2D Hybrid Halide Perovskites: Structure, Properties, and Applications in Solar Cells. *Small* **2021**, *17* (43). https://doi.org/10.1002/smll.202103514.

5. Handa, T.; Yamada, T.; Nagai, M.; Kanemitsu, Y. Phonon, Thermal, and Thermo-Optical Properties of Halide Perovskites. *Phys. Chem. Chem. Phys.* **2020**, *22* (45), 26069–26087. https://doi.org/10.1039/D0CP04426A.

6. Neu, J.; Schmuttenmaer, C. A. Tutorial: An Introduction to Terahertz Time Domain Spectroscopy (THz-TDS). *J. Appl. Phys.* **2018**, *124* (23). https://doi.org/10.1063/1.5047659.

7. Greco, M.; Leccese, F.; Doria, A.; Taschin, A.; De Francesco, E.; Giovenale, E.; Senni, L.; Gallerano, G. P. Studies of Leaf Water Content in Smart Agriculture Using THz Technologies: A Review. *J. Smart Environ. Green Comput.* **2022**, *2* (2), 46–57. https://doi.org/10.20517/jsegc.2022.12.

8. Krimi, S.; Klier, J.; Jonuscheit, J.; von Freymann, G.; Urbansky, R.; Beigang, R. Highly Accurate Thickness Measurement of Multi-Layered Automotive Paints Using Terahertz Technology. *Appl. Phys. Lett.* **2016**, *109* (2). https://doi.org/10.1063/1.4955407.

9. Yoshioka, K.; Wakamura, T.; Hashisaka, M.; Watanabe, K.; Taniguchi, T.; Kumada, N. Tracking Ultrafast Photocurrent Generation and Transport in HBN-Encapsulated Graphene Using On-Chip THz Spectroscopy. In *2022 47th International Conference on Infrared, Millimeter and Terahertz Waves (IRMMW-THz)*; IEEE, 2022; pp 1–2. https://doi.org/10.1109/IRMMW-THz50927.2022.9895641.

10. Jin, Z.; Peng, Y.; Fang, Y.; Ye, Z.; Fan, Z.; Liu, Z.; Bao, X.; Gao, H.; Ren, W.; Wu, J.; Ma, G.; Chen, Q.; Zhang, C.; Balakin, A. V.; Shkurinov, A. P.; Zhu, Y.; Zhuang, S. Photoinduced Large Polaron Transport and Dynamics in Organic–Inorganic Hybrid Lead Halide Perovskite with Terahertz Probes. *Light Sci. Appl.* **2022**, *11* (1), 209. https://doi.org/10.1038/s41377-022-00872-y.

Chapter 2

POLARIZATION-RESOLVED, ARBITRARY INCIDENCE
TERAHERTZ SPECTROMETER

2.1 Motivation

Optoelectronic technologies, which generally convert light into electricity and electricity into light, underpin our global society through their application as LEDs, light sensing photodiodes, solar cells, lasers, and more. The heart of every optoelectronic is a semiconducting material whose intrinsic ability to generate and conduct charge governs overall device performance. While characterizing and understanding these fundamental semiconductor properties is necessary for development, conventional techniques to do so often require mechanical contact to metallic pads deposited on top of the semiconductor.[1-2] These characterization methods yield conductivity information which can be highly influenced by the choice of metal for the contact, chemical and electric field effects of semiconductor-metal pad interface, the mechanical force of the contact probe, and more.[1-2] In contrast, terahertz time-domain spectroscopy (THz-TDS) provides a non-contact, non-ionizing technique for investigating crucial charge carrier dynamics in both standalone semiconductors as well as full optoelectronic devices.[3-5] The powerful capabilities of THz spectroscopy inspired the design and construct of a THz spectrometer in the Blake lab for interrogation of novel semiconductor materials and optoelectronic devices made in the Atwater lab. Specifically, we develop and optimize a terahertz transmission spectrometer for the purpose of investigating thin

film perovskite semiconductors with subtle, yet critical anisotropic properties. In constructing this phase coherent, ultrafast instrument, we incorporate state-of-the-art emission, detection, and analytical methods. After employing essential, yet under-reported, calibration procedures, we extract broadband THz properties in standard materials that provide a necessary foundation for original measurements in promising perovskite semiconductors.

2.2 Framework of THz Time-Domain Spectroscopy

2.2.1 Probing Electric Susceptibility with THz Pulses

Optical properties in non-magnetic materials are governed by the complex-valued parameters known as conductivity, dielectric permittivity, and refractive index. These parameters represent intrinsic charge behavior of the material in the presence of an applied electric field, and, for non-magnetic media, are related at specific frequencies through the following relations:

$$\tilde{\sigma}(\omega) = \sigma_1(\omega) + i\sigma_2(\omega)$$

$$\tilde{\varepsilon}(\omega) = \tilde{\varepsilon}_r(\omega)\varepsilon_o + i\frac{\tilde{\sigma}}{\omega} = \varepsilon_1(\omega) + i\varepsilon_2(\omega)$$

$$\sqrt{\tilde{\varepsilon}(\omega)} = \tilde{n}(\omega) = n(\omega) + i\kappa(\omega)$$

where $\omega = 2\pi\nu$, or angular frequency, $\tilde{\sigma}$ is the complex-valued conductivity, $\tilde{\varepsilon}$ is the complex dielectric permittivity, $\tilde{n}$ is the complex refractive index, ε_o is the

permittivity of free space (or vacuum, 8.854×10^{-12} F/m), and $\tilde{\varepsilon}_r$ is the complex

relative permittivity. The real (σ_1) and imaginary parts (σ_2) of conductivity describe

the amplitude and phase of an electric current density under an applied electric field.

The real (ε_1) and imaginary parts (ε_2) of the dielectric permittivity represent how

well the material can store and dissipate charge. Lastly, the real part (n) of the

refractive index represents how much light is slowed in the material while the

imaginary part (κ) is related to how much light is absorbed. The dielectric

permittivity is introduced through the famous Maxwell's equations and constitutive

relations, where the electric susceptibility χ_e is used to describe how easily bound

charges in a material can be displaced by an external electric field. The electric

susceptibility, χ_e, is related to the relative dielectric permittivity as:

$$P = \varepsilon_0 \chi_e^{(1)} E + \varepsilon_0 \chi_e^{(2)} E^2 + \varepsilon_o \chi_e^{(3)} E^3 + \cdots$$

$$\vec{D} = \varepsilon_0 \left(1 + \chi_e^{(1)} \right) \vec{E} = \varepsilon_0 \varepsilon_r \vec{E}$$

$$\varepsilon_r = 1 + \chi_e$$

where P is the electric polarization and $\vec{D}$ is the electric flux density of a material in

the presence of an external electric field. These relations show the relative dielectric

permittivity for a material with an isotropic and linear response to an electric field.

Some materials can also exhibit a nonlinear response to an electric field, which is

represented by additional susceptibility terms with corresponding dependence on the

electric field strength. Moreover, a given material can possess *anisotropic*

parameters, where the electric field response along one direction in the material is

different than another. In this case, the full permittivity is a tensor made up of multiple parameters from each spatial axis. The work in this thesis will include discussion of nonlinear THz electric field responses involved in the spectrometer setup, and linear THz field responses for both isotropic and anisotropic materials.

In THz time-domain spectroscopy, we generate a terahertz electromagnetic wave packet and send it through various media, each with distinct material parameters, before collecting the transmitted or reflected THz waves after the interaction. We then measure the amplitude and phase of the electric field component of these THz waves, which we can represent as a time-harmonic plane wave traveling in some direction z over some time t:

$$\vec{E}(z,t) = \vec{E}_0 e^{\left(-\frac{\kappa \omega z}{c}\right)} e^{j\left(\frac{\omega n z}{c} - \omega t\right)}$$

where $\vec{E}_0$ is the initial electric field amplitude. We see that the time-varying amplitude and phase of the THz electric field is directly affected by the relative permittivity, and therefore electric susceptibility, of the medium through which it is traveling. Before further analysis, the time-domain spectra are converted into the frequency-domain by fast Fourier transform. When using a phase-sensitive detection method, and known thicknesses of each medium, we can directly extract the full complex-valued material parameters of virtually any sample. Additionally, through the frequency-dependent parameter relations above, we can easily transform our complex refractive index data, for example, into dielectric permittivity or conductivity. This measurement capability exists in stark contrast to conventional

frequency-domain spectroscopic techniques like UV-Visible transmission and FT-IR, where only the imaginary component of material parameters associated with light absorption are experimentally measured.[6-7] To recover the real component of material parameters from these methods, significant approximations of the data must first be made before applying Kramers-Kronig relations.[6-7] Lastly, throughout this thesis we will narrow our discussion to non-magnetic media.

2.2.2 Isolating the THz Response

The goal of the THz-TDS spectrometer is to capture a spectrum which represents only the sample's response to THz light. As with most spectroscopic techniques, we must deconvolve the instrument response and any additional background signal from the sample measurement. To do so, we can employ the useful mathematical relationship that a deconvolution in the time-domain is equal to a division in the frequency-domain.[8] After collecting a suitable reference measurement, we simply divide the sample frequency spectrum by the reference to obtain the pure THz frequency response of our sample. The resulting spectrum will be either a transmission or reflection spectrum depending on the experimental configuration of the measurement. While a variety of THz probe configurations exist, each one has advantages and disadvantages depending on the sample material properties. For example, optically thick and/or highly conductive samples are better suited for reflection mode measurements, but at the cost of large phase errors due to micron-scale misalignment between the sample and reference surfaces.[9] Transmission

measurements, on the other hand, are often less sensitive to small deviations in sample/reference placement, but require weakly absorbing, weakly reflecting, or appropriately thin substances.[10] It is worth emphasizing, however, that this variety of possible experiment configurations makes THz-TDS a powerfully capable technique. For instance, one can investigate in situ biological and solution-based samples through an attenuated total reflection setup, or capture nanoscale spatially resolved THz dynamics through coupled scanning tunneling microscopy (STM) setups.[11] Though still an active area of research, the inherent flexibility of THz methods affords the ability to design experiments which take advantage of the sample characteristics, instead of trying to make the sample fit a maladapted spectrometer configuration. Our transmission configuration takes advantage of the intrinsic structure of our thin film samples and provides the ability to measure transmission at multiple angles of incidence with full polarization control of the input light and detection system.

2.2.3 Generalized Transfer Functions from Plane Wave Propagation

The frequency-dependent THz transmission (or reflection) spectrum is converted into complex-valued material parameters through a mathematical function which models the output frequency response from an input THz plane wave. This function is commonly termed the transfer function, and it forms the basis of all THz-TDS analysis. To model the isolated THz transmission spectra of a sample system, we consider the propagation of an initial electric field $E_0(\omega, \tilde{n}, d)$ as it travels through each layer of media with some refractive index $\tilde{n}$ and thickness d. The sequence of

this field propagation determines the form of the transfer function, which is dictated by the experiment and sample configuration. For instance, we will first consider the situation of a thin film sample on a thick substrate in transmission geometry. To accurately analyze the sample layer, though, THz material parameters of the substrate must first be known. Estimations of material parameters from independent experimental or theoretical characterization methods can be sufficient for substrates with non-dispersive, or flat, THz features. It is often the case, however, that a separate THz-TDS measurement of the substrate must first be performed. We therefore begin by building the THz transfer function for a general single slab with arbitrary thickness and refractive index before leading up to a multilayer thin film transmission function.

Typical derivations of the THz transfer functions in literature have primarily employed assumptions of weakly absorbing, or non-absorbing, samples at normal incidence.[8] To accurately extract material parameters in our anisotropic thin film perovskite samples, it was necessary to derive generalized transfer functions which consider electric field polarization, oblique incidence angle, and absorption strength of each experimental medium.[12-14] Although rarely reported in THz studies, these comprehensive propagation models yield higher accuracy parameter extraction and enable analysis of more nuanced experiment configurations for challenging sample investigations.[14]

We form the generalized slab transfer function, representing the isolated THz response of the substrate, through consideration of numerous terms and coefficients.
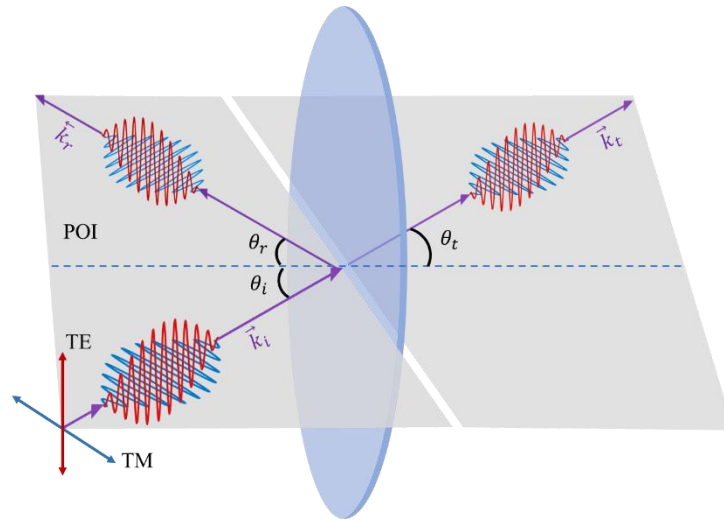
Figure 2.1. Plane-of-Incidence (POI) diagram for an input electric field which can be polarized either parallel (TM) or perpendicular (TE) to the POI.

The experimental stage is set according to the plane-of-incidence (POI), defined as the plane which is both normal to the incident interface and includes the incident electromagnetic wavevector ($\vec{k} = \omega n / c$) (Figure 2.1).

The electromagnetic wave is described as transverse magnetic (TM) polarized, also known as p-polarized, when its electric field is linearly aligned parallel to the POI. Conversely, an electromagnetic wave is transverse electric (TE) polarized, also known as s-polarized, when its electric field is linearly aligned perpendicular to the POI. The specific interaction of the electric or magnetic field component parallel to the POI leads to many interesting consequences in light-matter interactions, such as the existence of a polarizing angle (known as Brewster's angle).[13] In anisotropic matter, moreover, the polarization state of light can be used to isolate a specific

component of the relative dielectric permittivity. For our immediate purposes, we next define the polarization- and angle-dependent Fresnel coefficients.

Specifically, the Fresnel coefficients represent the relative amplitude of the incident field which is reflected or transmitted at an interface between two distinct media, each with refractive index $\tilde{n}_j = n_j + i\kappa_j$. Following a recent derivation from Oughstun and Palombini[13], the generalized Fresnel coefficients r_{TE}, t_{TE} and r_{TM}, t_{TM} may be written in the form:

$$r_{TE_{jk}} = \frac{(n_j \cos(\theta_j) + i\kappa_j \sin(\psi_j)) - (n_k \cos(\theta_k) + i\kappa_k \sin(\psi_k))}{(n_j \cos(\theta_j) + i\kappa_j \sin(\psi_j)) + (n_k \cos(\theta_k) + i\kappa_k \sin(\psi_k))}$$

$$t_{TE} = 1 + r_{TE}$$

$$r_{TM_{jk}} = \frac{\epsilon_j(n_k \cos(\theta_k) + i\kappa_k \sin(\psi_k)) - \epsilon_k(n_j \cos(\theta_j) + i\kappa_j \sin(\psi_j))}{\epsilon_j(n_k \cos(\theta_k) + i\kappa_k \sin(\psi_k)) + \epsilon_k(n_j \cos(\theta_j) + i\kappa_j \sin(\psi_j))}$$

$$t_{TM} = 1 - r_{TM}$$

where $\tilde{\theta} = \theta + i\psi$ from Snell's complex law of refraction.[13] We see that these coefficients are both polarization and incidence angle dependent, simplifying greatly in the case of non-absorbing media at normal incidence. In the transfer function, we also consider the propagation coefficient:

$$P_j = e^{i\omega l_j n_j/c} e^{-\omega l_j \kappa_j/c} = e^{\omega l_j (in_j - \kappa_j)/c}$$

where, at oblique incidence, the optical thickness l_j is determined from the incidence angle dependent phase propagation[12], or:

$$l_j = \frac{d_j}{\cos{(\theta_j)}}$$

Lastly, we must consider the inclusion of any internal reflections in the general slab which make it into the time-domain scan of the signal. These reflections are often called Fabry-Perot etalons and their time-domain coefficient has the form:

$$FP_{ijk} = \sum_{m=0}^{M} (r_{jk}P_j r_{ji}P_j)^m$$

where we sum all the etalons m arriving to the detector after reflecting off both the front and back interfaces of the general slab.[8] The FP coefficient is also polarization and angle sensitive when using the preceding Fresnel terms. Figure 2.2 shows a diagram of the modeled THz wave propagation through the general (i.e., substrate) layer, where an inert atmosphere layer (nitrogen in our case) is the first and last medium with indices $\tilde{n}_1$ and $\tilde{n}_4$. The corresponding reference pulse only interacts with the nitrogen layer as it travels from emitter to detector. Accounting for only the relevant parameters, we can finally construct the substrate transfer function for THz transmission:

$$\tilde{T}(\omega, \tilde{n}, d, \theta, pol.) = \frac{\tilde{E}_{substrate}(\omega)}{\tilde{E}_{nitrogen}(\omega)} = \frac{t_{12} t_{23} P_2 FP_{123}}{1}$$
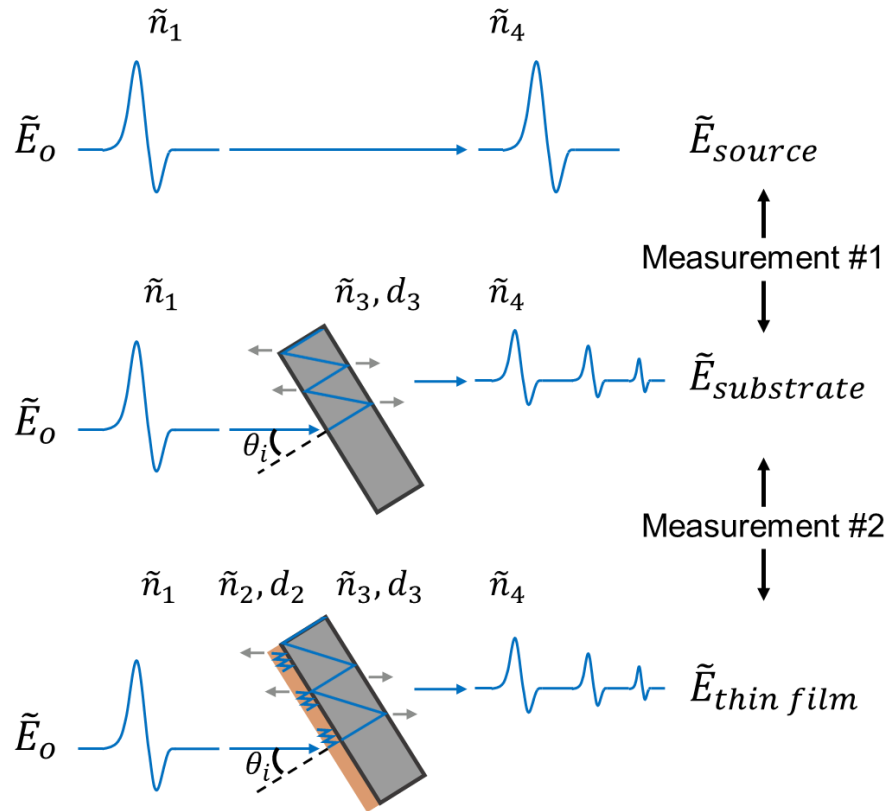
Figure 2.2. Depiction of THz pulse transmission through inert atmosphere (top), a general slab or substrate (middle), and a thin film supported by a substrate (bottom). The THz propagation begins with a source pulse ($\tilde{E}_o$) traveling through an initial media with refractive index $\tilde{n}_1$, which is often equal to the last media ($\tilde{n}_1 = \tilde{n}_4$). Reflections off sample interfaces lead to etalons in the detected time-domain waveform and spectra generated by Fourier transform.

Using this formula, we can perform fitting routines, described in section 2.7, to extract the complex refractive index of our substrate. Further, we can also exclude the FP terms in our measurement by only scanning the time-domain window with the main THz pulse. These material parameters will be directly used in the measurements of the thin film sample refractive index, where the transfer function takes more shape. When a generalized slab approaches a thickness far below the wavelength of the electric field, the main transmitted THz pulse becomes

superimposed with all possibly detectable FP etalons. In typical spectroscopic THz

bandwidths (0.3 – 10 THz), this "thin film" limit exists for sample thicknesses below

approximately 1 – 2 µm depending on the sample refractive index.[8-9] At this point,

we can represent the FP coefficient as "Thin Fabry-Perot" coefficients by taking its

limit upon approaching infinity:

$$TFP_{ijk} = \frac{1}{1 - r_{jk}r_{ji}P_jP_j}$$

where now we can more accurately construct the transfer function for a thin film

sample on a thick substrate. For this formula, it is assumed that the substrate is

sufficiently thick so that only the sample etalons are captured in the scan.

Specifically, the thin film is facing the incident THz beam in our experiment, so the

refraction from the sample layer into substrate layer becomes distinct in the

generalized transfer function compared to refraction in the substrate layer from the

THz source:

$$\tilde{T}(\omega, \tilde{n}, d, \theta, pol.) = \frac{\tilde{E}_{thin\,film}}{\tilde{E}_{thick\,substrate}} = \frac{t_{12}t_{23}t'_{34}P_2P'_3 TFP_{123}}{t_{13}t_{34}P_3}$$

This distinct refraction is represented by the prime terms, where, at oblique

incidences, the THz field incident into the substrate after the thin film is different

than the field incident from nitrogen. Depending on the material, it is also possible to

measure stand-alone thin films, where the transfer function simplifies to:

$$\tilde{T}(\omega, \tilde{n}, d, \theta, pol.) = \frac{\tilde{E}_{thin\,film}}{\tilde{E}_{nitrogen}} = \frac{t_{12}t_{23}P_2P'_3 TFP_{123}}{1}$$

We can additionally explore multilayer thin film stacks through THz transmission. We will focus on a two-layer thin film for this exercise.[15] Due to the presence of interference between the reflecting and transmitting waves in the double layer thin film, we must consider a different form of the FP etalons traveling through the combined sample and substrate thin films:

$$DTFP_{ijkl} = \frac{1}{\left(1 - r_{jk}r_{ji}P_j{}^2\right) - \left(r_{kj} + r_{ji}P_j{}^2\right)\left(r_{kl}P_k{}^2\right)}$$

where DTFP represents the "Double layer Thin film Fabry-Perot" coefficient for a THz wave traveling from nitrogen layer "i" into the sample thin film layer "j" and then the substrate thin film layer "k" and ending in the nitrogen layer "l". Incorporating this new term, we can form the THz transmission transfer function for a bilayer thin film as:

$$\tilde{T}(\omega, \tilde{n}, d, \theta, pol.) = \frac{\tilde{E}_{thin\,film\,sample}}{\tilde{E}_{thin\,film\,substrate}} = \frac{t_{12}t_{23}t'_{34}P_2 P'_3 DTFP_{1234}}{t_{13}t_{34}P_3 FP_{134}}$$

These transfer functions will allow us to rigorously analyze our high-quality thin film semiconductors at arbitrary angles of incidence and with selective polarization control (Figure 2.3). The generalized transfer functions presented here are not meant to be exhaustive, and the reader is encouraged to explore references 8, 14, and 15 for more thorough discussions. Now that we have introduced the relevant concepts for
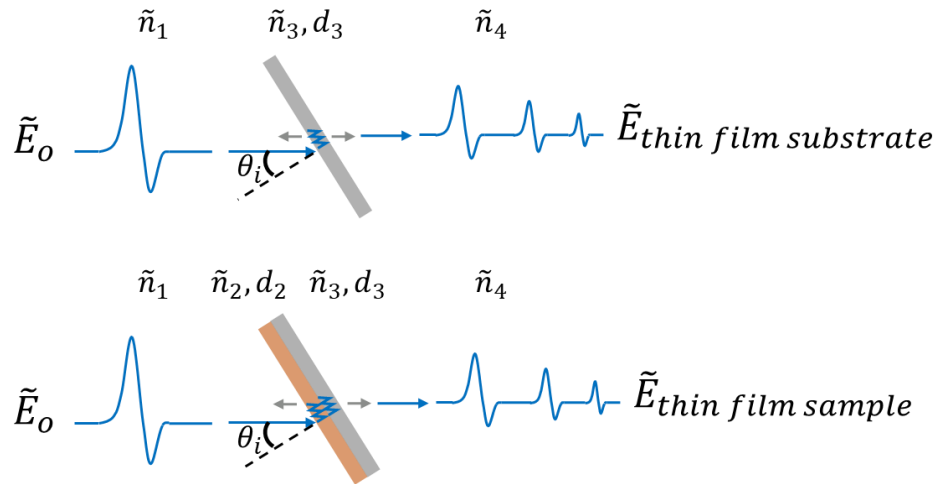
Figure 2.3. Depiction of THz transmission through thin film substrate and multilayer.

the theoretical framework of THz-TDS, we can discuss how the techniques are applied on the optical table.

2.2.4 THz Time-Domain Spectroscopy in Practice

All spectroscopic techniques operate in four broad phases: light emission, sample interaction, light detection, and data analysis. In the following sections, we will cover our developments in each of these phases in detail, but first we will present the general layout of our instrument (Figure 2.4).

We start with an ultrafast titanium doped sapphire (Ti:Sapphire) regenerative amplifier-based laser system which outputs 800 nm pulses. This thesis includes data from two different amplified Ti:Sapphire lasers, a Spectra-Physics Spitfire 2 kHz repetition rate laser with ~100 fs long ~1.75 mJ useable pulse output, and a Coherent
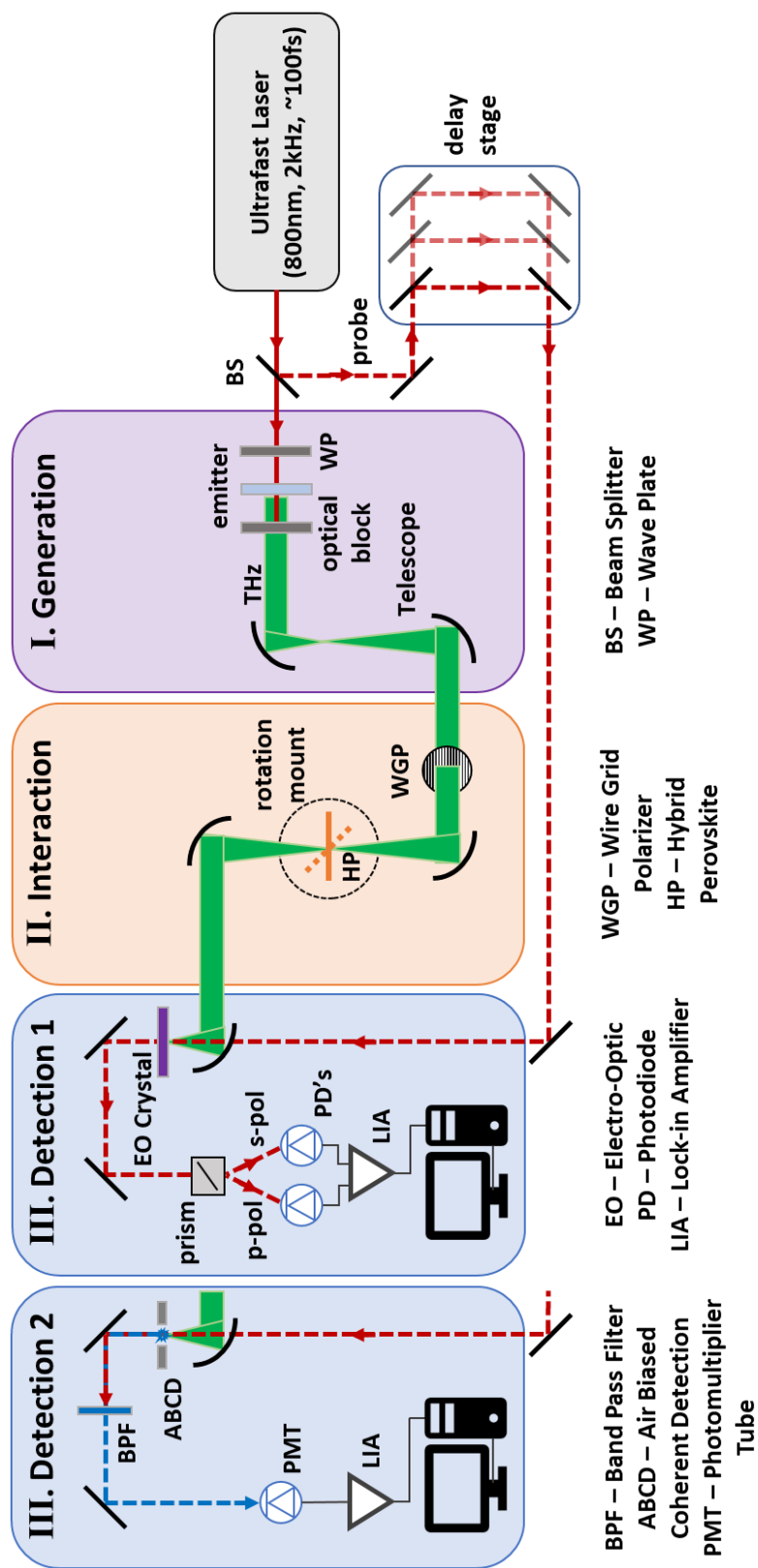
Figure 2.4. Schematic of an example THz time-domain spectrometer displaying both an electro-optic sampling detection (1) and an air-biased coherent detection (2).

Legend 1 kHz laser with ~35 fs long ~2.6 mJ useable pulse output. The process and setup for the THz-TDS spectrometer was the same.

The initial 800 nm laser beam was split into a THz generation line and an optical probe line with a 90:10 beam splitter, and the optical path lengths for both lines were made to match between the beam splitter and the detection point. A nitrogen purge box houses all the terahertz optics to provide an atmosphere free of water vapor for the THz generation, interaction, and detection processes. Along the THz line, the 800 nm beam is sent into a THz emitter which generates <1 ps long THz pulses. The THz beam was then expanded through a reflective telescope to fill the 2-inch off-axis parabolic (OAP) mirrors used to direct the THz pulses to the sample and detector. The THz beam was then made to focus into the sample with a 3-inch focal length OAP before being collimated and focused down again onto the detector with a 2-inch focal length OAP.

The THz path length is made to be static, so that the ~1 ps long THz pulses arrive to the detector at the same relative time with each repetition of the laser output. The THz electric field is then temporally scanned with the optical probe beam by varying the path length of the probe with a mechanical delay stage. We employ heterodyne detection schemes that measures change in the optical probe signal which is linearly proportional to the strength of the THz field interaction. Because the optical probe pulse duration is so much shorter than the THz pulse (~35 fs << 1 ps), we can use the optical pulses as a delta function to measure the THz electric field at precise temporal
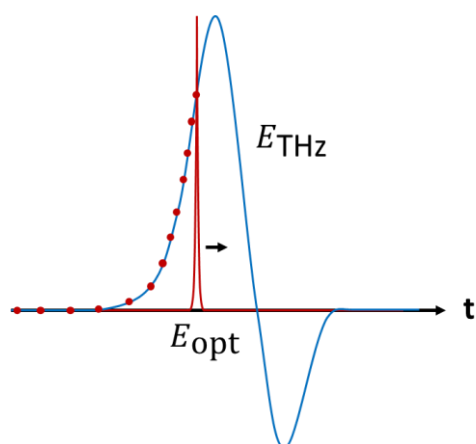
Figure 2.5. Optical sampling of the THz pulse.

overlap positions (Figure 2.5). The detection methods are such that when the probe pulse arrives before the THz pulse, there is no change in the reference signal, and we only see baseline noise. As the probe and THz pulses begin to overlap, there is a quantitative and sign-dependent change in the reference signal which fully represents the THz electric field after scanning an appropriately long time-window. The THz time-domain spectra are then a collection of many temporal data points, the density of which determine the length of the Fourier transformed frequency-domain spectra. Conversely, the length of the time-domain spectra dictates the frequency resolution of the Fourier transformed data.

In our experiments, the probe signal is collected by either a silicon photodiode or a photomultiplier tube (Thorlabs PMM01) which converts the light into a current that is read by a lock-in amplifier (Stanford Research Systems SR830). The lock-in is synced to a modulation frequency of the experiment which is given by either a chopper on the beam line or as a square wave voltage bias on the detector. The frequency-modulated current is converted to a voltage by the lock-in, which is then digitized by a National Instruments data acquisition card (USB-6361). At this point, the time-domain signal can be processed by averaging, apodization, and Fourier transform before analysis.

These steps describe the general experimental framework for an arbitrary THz time-domain spectrometer measuring transmission or reflection of samples. Different optics can be used to generate, transport, and detect THz light, different heterodyne detection schemes or optical probe configurations can be employed to enhance or alter detection efficiency, but the four main phases are still present. As the THz field matures, new and optimized methods will arise to better facilitate both the theoretical and experimental frameworks of this powerful spectroscopy. The following sections give an overview of the methods used throughout this thesis work to capture and interpret terahertz spectra. Among specific references throughout, the reader is highly encouraged to review the thesis of Blake group alum Matthew Kelly for complementary and well-written perspectives on employing terahertz time-domain spectroscopy.

2.3 Development of THz Emission

There are currently four general categories of THz emission mechanisms most popularly used in THz-TDS: optical rectification, photoconductive antennas, plasma emission, and spintronic terahertz emission. Photoconductive antennas were not implemented in this thesis work as they are tailored for oscillator laser systems, though several excellent reports exist on their function.[8,16] The other three methods were each actively implemented in this spectrometer, so we will go over their behavior in more depth.

2.3.1 Optical Rectification (OR)

The first reported opto-electronic method of generating THz beams implemented optical rectification in a quartz crystal.[17] Decades of development have made this emission technique highly accessible and reliable for THz spectrometers.[18] Optical rectification is a second order nonlinear optical effect where light possessing some bandwidth undergoes frequency mixing with itself to generate a DC electric field.[19] When using ultrafast optical pulses, the frequency mixing occurs from the higher and lower ends of the optical bandwidth to produce "low frequency" THz pulses at the difference frequency. Following a derivation from Ingrid Wilke and Suranjana Sengupta[20], the optical rectification for THz emission is performed in electro-optic materials with strong second order electric polarization P controlled by the susceptibility $\chi_e^{(2)}$:

$$P_2^{nl} = \chi_e^{(2)} E^2$$

If we have two electric fields represented as:

$$E_1 = E_0 \cos(\omega_1 t) \,;\; E_2 = E_0 \cos(\omega_2 t)$$

then

$$P_2^{nl} = \chi_2 E_1 E_2 = \chi_2 \frac{E_0^2}{2} [\cos((\omega_1 - \omega_2)\,t) + \cos((\omega_1 + \omega_2)\,t)]$$

Here $(\omega_1 - \omega_2)$ represents the difference frequency mixing responsible for THz generation. Further, phase matching is a crucial part of efficiency in nonlinear optical processes.

Because the optical probe and THz field travel at different speeds inside the electro-optic materials, due to dissimilar refractive indices for these frequencies, there exists a coherence length, l_c, which describes the tolerable amount of phase mismatch in the system, or:

$$l_c(\omega_{THz}) = \frac{\pi c}{\omega_{THz}|n_g(\omega_0) - n_{THz}(\omega_{THz})|}$$

where n_g is the optical group refractive index. Optical rectification is widely used in THz emitters in both semiconducting zincblende crystals which offer weak to moderate field strengths (~10 kV/cm) as well as synthetic organic crystals which offer intense THz field strengths (>1 MV/cm) in tabletop systems.[21] THz field emission is limited in zincblende electro-optic (EO) crystals due to their low damage thresholds from 800 nm optical pulses. Moreover, while the radiated THz beam polarization is easily tunable in the linear regime, circularly polarized THz emission has required either the phase offset combination of two pump pulses or two THz pulses.[22] We go into more detail about the electro-optic (zincblende) crystals used in this work in the detection section.

2.3.2 Two-Color Plasma Emission

Access to the intense peak field strengths of ultrashort optical pulses allows us to use air itself as a nonlinear optical medium for THz generation. The power at the focal point of a converging amplified laser beam is enough to strip electrons off the local gas molecules and generate plasma. In contrast to optical rectification in EO crystals,

air plasmas hold no damage threshold, are capable of extremely wide bandwidths (0.1 – 200 THz) at ~MV/cm field strengths, and support ultrabroadband circularly polarized THz emission.[23-25] Two-color plasma emission specifically involves mixing the fundamental and second harmonic of the laser beam at the focal point to enhance the overall generation process (Figure 2.6). Preceding the recent rise of strong spintronic THz emitters, two-color plasma emission was the most reliable way to carry out THz spectroscopy at and above 10 THz frequencies using a tabletop source.
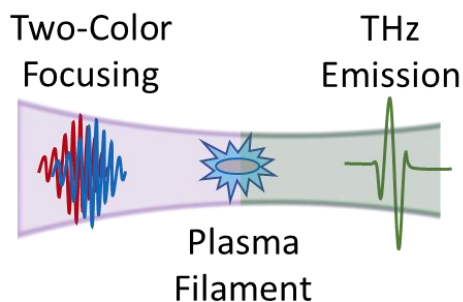

Figure 2.6. Two-color laser focusing to produce THz pulse from plasma filament.

The broad discussion here follows the excellent work described in the thesis of Alessandro Tomasino[26], where he untangles the recently confirmed mechanisms involved in two-color plasma emission. The fundamental wavelength of the laser beam, 800 nm in our case, is sent through a nonlinear BBO (beta barium borate) crystal that generates the second harmonic, which has twice the frequency (and thus half the wavelength) of the original beam. The two pulsed beams then colinearly travel to the focal point of an off-axis parabolic mirror, where they are spatially and temporally overlapped by tuning the BBO crystal orientation. The spatially confined beams at the focus possess intense energy which creates a highly ionized air plasma that includes a mixture of charged ions and free electrons. The process of ionization is initiated by mechanisms

like tunneling ionization, where the strong electric field enables electrons to overcome the binding forces to atoms and nuclei. As the ionization progresses, the interaction between the two pulses and the plasma leads to a phenomenon called plasma filamentation. The plasma filament is balanced by self-focusing from the Kerr effect and de-focusing from the plasma intensity itself. The Kerr effect results from a nonlinear change in the air refractive index at the dense plasma core while de-focusing arises from a near saturation of the pulse peak intensity in the presence of the plasma. The interplay of plasma photocurrents from tunneling ionization, Kerr effect through four-wave rectification, and transverse and longitudinal plasma waves in the filament facilitates THz radiation. Further, the filament can act as a waveguide to produce highly directional emission of the THz beam both parallel as well as perpendicular to the plasma propagation.

The strength of the plasma generated THz beam is influenced by several factors. At fixed optical power, longer plasma filaments tend to linearly increase the resulting THz field strength, while higher optical fluence at fixed focal distances do not necessarily show this effect. That is because high fluences at short focal distances can lead to transverse widening of the filament with little to no longitudinal gains. Shorter optical pulse durations generally lead to broader THz emission bandwidths, while chirping the input pulses can rotate the emitted THz polarization. Longer fundamental wavelengths, or lower input pulse frequencies, also show a significant positive impact on broadband THz power generation. Though two-color plasmas reliably offer useful THz sources, there implementation suffers from sensitivity to
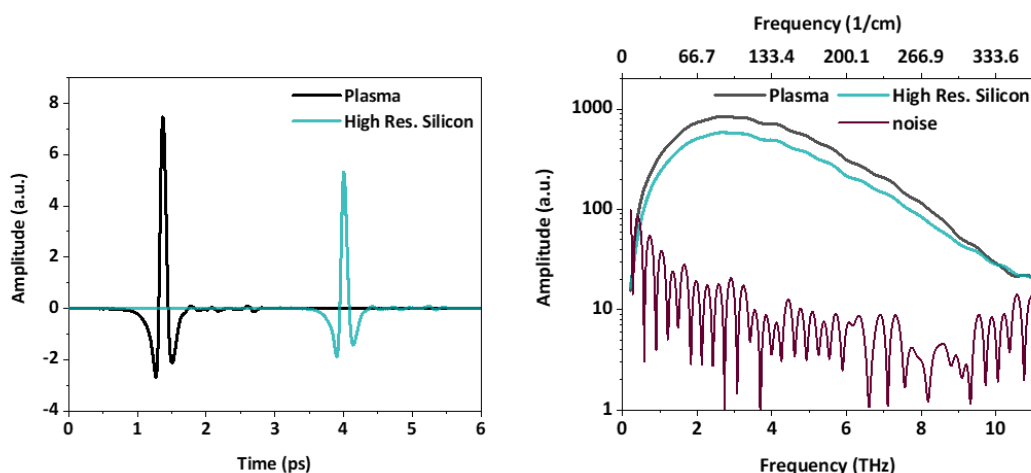
Figure 2.7. Plasma generated THz pulse transmitted through a nitrogen purge atmosphere and through a high resistivity (>10 kOhm, 280 μm thick) silicon wafer in time-domain (left) and frequency-domain (right).

atmospheric pressure, significant laser shot-to-shot noise, as well as the need to access strong optical pulses ($\gtrsim 100\ \mu J/cm^2$).

In our experiments, we utilized 800 nm fundamental beams at fluences ranging from 1 – 8 mJ/cm^2 with various off-axis parabolic mirrors possessing focal distances between 1 - 6 inches long. With a properly inert atmosphere, we could reach >50 kV/cm THz field strengths with bandwidths beyond 12 THz, as shown in Figure 2.7. Though effective for high bandwidths, the plasma emitted THz pulses required extensive averaging times to yield resolvable sample absorptions in this frequency range due to the significant shot-to-shot pulse fluctuations. For this reason, we turned to spintronic THz emitters for access to noise stable, broadband, and strong THz emission.

2.3.3 Spintronic Terahertz Emitters (STEs)

The discussion presented here follows the excellent work and analysis by Seifert and Kampfrath.[27-28] Spintronic terahertz emitters are an exciting new development in the field of THz spectroscopy enabling intense (>1 MV/cm) electric field strengths at ultrabroadband frequencies from single cycle THz pulses.[28] These strong, "clean" pulses contrast the pulses from organic emitters and electro-optic crystals which commonly display lingering amplitude oscillations, known as ringing, due to low energy optical phonon excitations. Moreover, the THz generation occurs in a robust solid-state emitter that greatly enhances power stability in output light compared to the shot-to-shot fluctuations intrinsic to plasma emission. This fascinating technology is already opening new paths to nonlinear THz control of excitations in matter as well as providing feasible routes towards on-chip THz spectroscopy. All the capability of these emitters is accessible through relatively cheap fabrication costs at scale, making them a truly revolutionary technology for the future of THz spectroscopy.

Furthermore, early studies into these devices have revealed a plethora of operational advantages.[27-29] For instance, the achievable bandwidth is only limited by the duration of the pump pulse, and the polarization of emitted THz light is controlled only by the direction of an applied magnetic field, not that of the incident optical/IR pulse.[27-28] With an appropriately linear magnetic field across the emitter, the resulting THz polarization is made to be equally linear with a direction pointing orthogonal to the magnetic bias. Likewise, the emission is found to be unaffected by the input pump

wavelength, enabling a wide range of ultrafast lasers to be used. The implications of these properties make terahertz spintronic emitters extremely adaptable to diverse experimental configurations using various ultrafast systems or that require tunable polarization of the THz beam.

Spintronic terahertz emitters predominately operate on a transient inverse spin Hall effect (ISHE) where a photoinduced spin-current traveling from a ferromagnetic metal into a nonmagnetic metal generates a transverse electron conduction current.[27] By implementing the thorough mechanistic analysis by Kampfrath et al., we can understand that ultrafast demagnetization and terahertz spin transport are the largest physical contributions to this spin-current generation.[27] When a high energy pulse is absorbed by a statically magnetized ferromagnet, ground-state electrons are sent into excited-states with dramatically different lifetime, energy, and velocity than at equilibrium conditions. Additionally, the minority spin-polarized electrons (e.g., spins aligned downward) in the ferromagnet have much lower mobilities than the majority spin-polarized electrons. An imbalance is created in the electron transport across the ferromagnet/nonmagnetic interface which drives a net current flow of majority spin-polarized electrons into the nonmagnetic layer. This terahertz spin transport occurs at approximately the same relaxation rate as the ultrafast demagnetization, which describes transient spin-flips of excited-state electrons scattering off the ferromagnet crystal lattice as equilibrium magnetization is recovered. Furthermore, Kampfrath et al. find that any photoinduced temperature gradient plays a trivial role in the typical THz spintronic emission, due to small values

of the associated Seebeck coefficients as well as thermal relaxation occurring on faster timescales than the spin-current transport.[27] Enhancing the available terahertz strength and bandwidth from these emitters are thus a matter of increasing spin-current amplitude as well as relaxation times associated with spin-dependent electron transport.
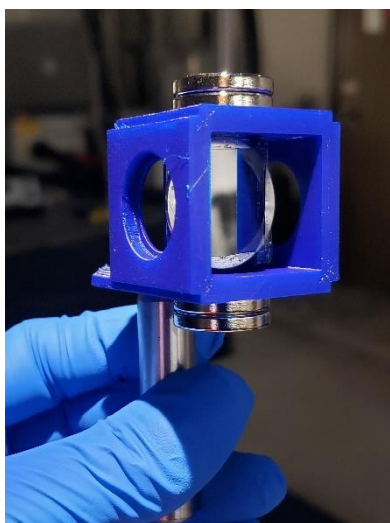

Figure 2.8. Spintronic emitter sitting in 3D printed mount which supports Nd magnets for external bias.

In collaboration with Jared Sisler in Atwater group and Jax Dallas in the Blake group, we have implemented THz spintronic emitters which were fabricated in-house by magnetron sputtering. Specifically, a ~1.8 nm thin ferromagnetic Co layer is deposited between two nonmagnetic metals layers ~2 nm thick (Pt and W). The multilayer stack sits on an optically transparent sapphire substrate and the device is mounted in a custom 3D printed holder which allows for magnets to sit on either side on the device (Figure 2.8). The spintronic stack is placed under a relatively weak magnetic field with Nd magnets to prepare the equilibrium population of spin-polarized electrons before excitation with the 800 nm beam. The transient relaxation process generates THz frequency pulses that are bi-directionally radiated parallel to the pump path. Our trilayer emitters can be pumped with either collimated or diverging light over a maximum active area of ~2 × 2 cm, limited only by the size of magnets used. When pumping the large area with fluences of
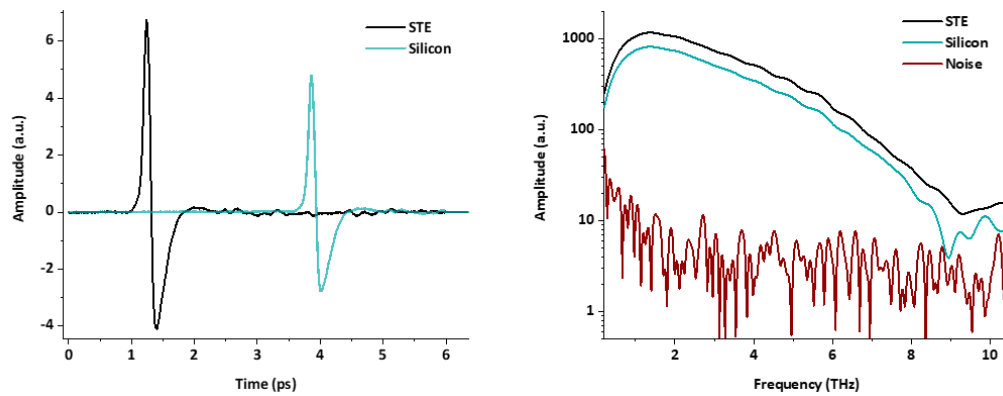
Figure 2.9. Spintronic THz generated pulse transmitted through a nitrogen purge atmosphere and through a high resistivity (>10 kOhm, 280 μm thick) silicon wafer in time-domain (left) and frequency-domain (right).

~820 uJ/cm^2 in the diverging portion of the beam under inert nitrogen atmosphere, we observe single cycle THz pulses with field strengths of order 100 kV/cm (Figure 2.9). Despite this encouraging result we are actively pursuing new device configurations which could improve spintronic performance.

One natural effect of the spintronic emission mechanism is that the THz pulses co-propagate both towards and away from the sample, meaning that we are potentially losing up to half the possible THz field strength. A solution to collect this back-propagating wave is employing emitter substrates which are not only optically transparent for the pump, but also THz reflective. For example, ITO coated glass (SiO$_2$) was used recently to demonstrate how the back-reflected THz pulse can improve amplitude of the measured signal. In this study by Matsunaga et al., a microfilm (~30 μm) of glass was used as a spacer layer between the spintronic stack and the substrate to engineer a λ/2 reflection path distance, where λ is the wavelength

of THz being enhanced.[30] More precisely, it is necessary to consider the refractive

index in the spacer layer for this reflective distance matching through the relation:

$$\frac{\lambda}{2} = n \cdot l$$

where l is the spacer thickness and n is the refractive index of the spacer. Although

a good experimental proof-of-concept, the THz reflection will be limited in this

configuration due to the imperfect reflectivity of the ITO substrate as well as the THz

absorptive properties in SiO_2. Instead, we are actively developing spintronic emitters

with silicon nitride spacer layers, which show excellent optical transmission and

almost no absorption through 10 THz.

The silicon nitride based spintronic emitters will be tested with ITO coated glass

back-reflection as well as with gold wire grid arrays deposited onto transparent

sapphire substrates. (Figure 2.10) The metal grid design follows the theoretical
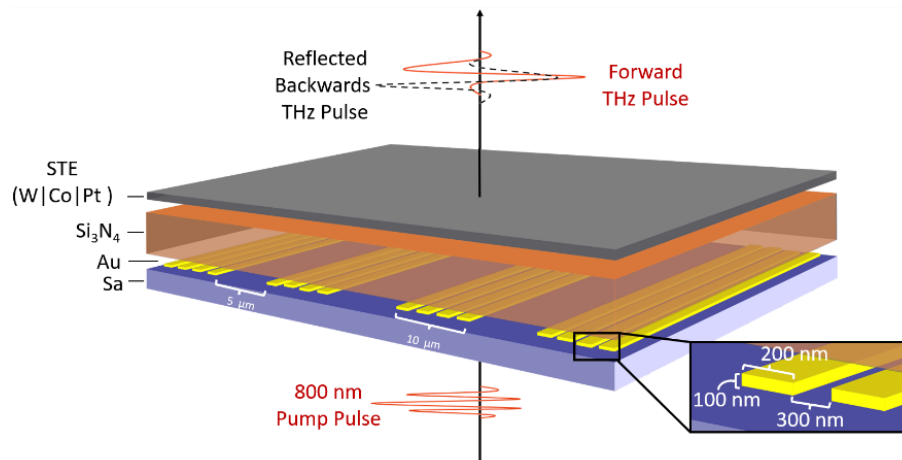

Figure 2.10. Spintronic THz emitter in development. Plasmonic gold arrays act as THz back reflector to enhance forward propagating signal. The spacer (Si_3N_4) is ~4-8 μm thick.

predictions by Zhang et al. who model near perfect THz reflectivity in simulations with a vacuum layer between the THz emitter and reflector.[31] This metal-based reflection layout is a commonly used method for terahertz polarizer optics, for example, where free-standing metal wires selectively transmit THz light that is orthogonally polarized to the wire alignment. Comparing multiple back-reflector designs will allow us to examine relevant advantages and disadvantages, while various silicon nitride spacer thicknesses will allow us to test the tunability of THz field enhancement. Improving on conventional performance of this incredibly significant class of THz emitters will help facilitate new and better THz technologies across the diverse scope of possible applications.

2.4 Optimizing the THz – Sample Interaction

The quality of the THz – sample interaction is crucial for maintaining strong signal detection and accurate interpretation of the data. We discuss several important aspects of the spectrometer which can be tuned to ensure robust sample measurements.

2.4.1 Tuning THz Optics

After the terahertz pulses are generated, the first important optics are an optical beam block and THz polarizer (Figure 2.11). Because THz-TDS spectrometers often focus the THz beam onto the sample, it is vital to ensure that no optical light bleeds into

the THz relay to avoid sample damage from higher energy photons. A linear polarizer is similarly critical for our measurements, as the analysis of anisotropic materials requires clean input polarization onto the sample. We employ a high resistivity (>10 kOhm)

Figure 2.11. Wire grid polarizer with 12.5 μm spacing (left) and mounted high resistivity (>10 kOhm) silicon wafer (right).

double-side polished 2-inch silicon wafer as a THz transparent beam block and the PureWave wire grid polarizer (PW005-012-050) which is rated up for use up to 6 THz.

The polarization pure THz signal is transported by a gold coated off-axis parabolic (OAP) mirror relay which is carefully aligned to ensure minimal aberration of the THz focus. These optics can be very challenging to align by hand, as slight deviations in their pointing have large impact on their focusing or collimating quality. Our relay was aligned using the 800 nm terahertz generation beam with neutral density filters for safety. Beam quality throughout the OAP relay was confirmed by using a white card to observe nicely circular and constant collimation at long distances (>12 inches), as well as symmetrically circular focusing and divergence. We focus down on the sample to maximize the THz field strength, which is a common method in THz-TDS instruments due to the behavior of Gaussian beam propagation. That is, ultrafast lasers, and therefore generated THz beams, can be viewed as having a spatially distributed irradiance pattern which can be represented by a Gaussian

function. This type of beam exhibits diffraction-limited focusing, where the minimum possible spot size before the beam shape alters into a diffraction pattern is determined by the wavelength of the beam. At the diffraction-limited focus, or beam waist, the beam exhibits flat wavefronts which allow us to use the plane wave solutions for THz – sample interactions. This plane wave type propagation generally occurs over the physical distance it takes for the cross section of the beam waist to double, also known as the Rayleigh length. These parameters are extremely important to characterize in a THz spectrometer, as they set limitations on how small or thick a sample can be before the plane wave solutions used in analysis are no longer valid. For example, in our setup, we focus down a 2-inch-wide Gaussian shaped THz beam with bandwidth ranging from 0.4 THz to 6 THz onto a sample placed at the 3-inch focal distance. At 0.4 THz, the diffraction limited beam waist and depth-of-field (2x Rayleigh length) would be ~1.5 mm in diameter and ~4.4 mm long, respectively. At 6 THz, the values would be ~100 µm in diameter and ~300 µm long, respectively. We see that, in conventional transmission setups, sample area is primarily limited at lower frequencies, while sample thickness is limited at higher frequencies. Additionally, short focal length OAP mirrors can induce polarization mixing at the several percent level which decreases polarization purity. These types of important considerations help guide the design of the terahertz experiment around the sample.

2.4.2 Sample Alignment

Another critical aspect towards optimizing the transmission measurement is the careful alignment of beam normal incidence to the sample. All alignment of THz

beams is made somewhat more complicated by the lack of ability to physically see THz light. In our setup, we again use the neutral density filtered 800 nm beam to carefully align the sample by spatially overlapping the back reflection of the incident light off the sample (or a mirror) with its incident spot. Utilizing an iris placed between the OAP and the sample, and centered around the incident 800 nm beam, we can use an IR viewer to accurately position the sample so that the back reflected light passes neatly through the iris center. If the sample is too weakly reflecting, a reference material can be used to align the sample holder, so that the sample can be easily swapped with the mirror reference to the correct position. This method is easily aided by photodiodes or imaging setups, where a quantitative value can be used to assess pointing off the sample surface.
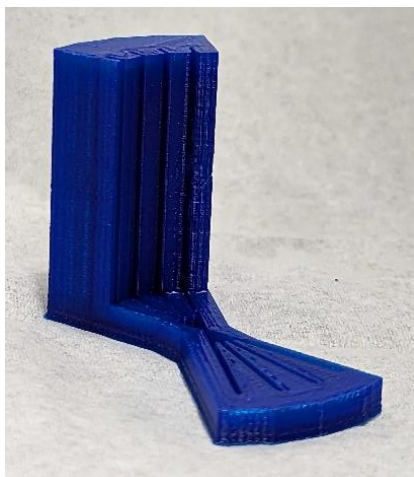
Figure 2.12. Custom 3D printed holder designed to slot complementary frames with mounted samples at precise angles.

Accurately positioning (within ~1° error) the sample and reference materials greatly impacts the successful extraction of the material parameters which are derived from incidence angle dependent transfer functions. A 3D printed sample holder is employed in our instrument to facilitate precise rotations about the center axis, so that large oblique incidence angles are well controlled (Figures 2.12 and 2.13). This holder is mounted on an automated translation stage which facilitates alternating measurements between a reference and sample when positioned directly adjacent to

each other (Figure 2.14). As our spectrometer collects data throughout the day, our system will be exposed to laser drift and therefore errors from changes in beam pointing. Continuously alternating the sample and reference scans allows us to maintain consistent experimental error in both datasets, leading to more accurate confidence intervals in analysis.[32] The alternative measurement procedure, where all the scans for either sample or reference are collected first, can lead to datasets which present unintended changes in the experiment environment as real trends. Our precise sample alignment, custom holder, and alternating scanning procedure help to dramatically improve the signal strength and confidence of the oblique incidence measurements.
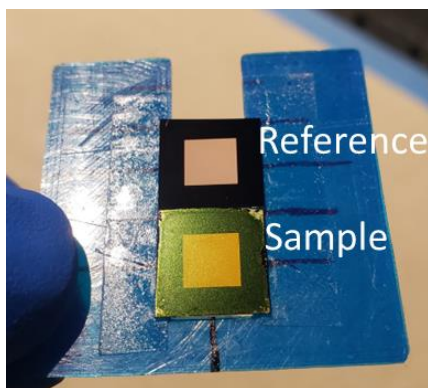

Figure 2.13. Custom 3D printed sample holder designed to slot into complementary frame at precise angles.

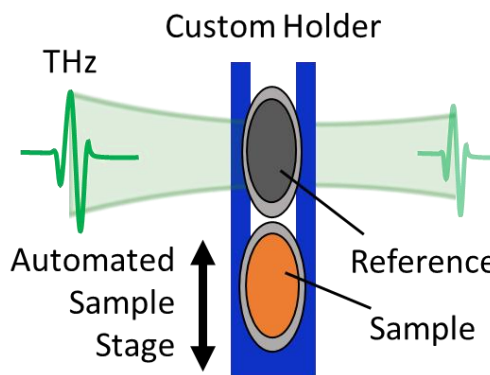**Figure 2.14. Diagram showing alternating THz transmission through a reference and sample mounted on our custom 3D printed holder, which is moved into the THz beam by an automated stage.**

2.5 Development and Implementation of THz Detection Methods

We now describe approaches to collect the THz pulses that we have generated, interacted with the sample, and transported to the detector. It so happens that the

processes for generating THz beams can also be implemented to detect THz beams through reciprocal operation. For example, the electro-optic crystals used for optical rectification can also be used for THz detection with only minor changes. In our experiments, we have employed the detection mechanisms known as electro-optic sampling (EOS) and air-biased coherent detection (ABCD). Both these techniques employ a heterodyne detection scheme, where the collected signal contains the amplitude and phase modulation of a reference optical probe beam ("local oscillator") in response to THz interactions.

2.5.1 Electro-Optic Sampling (EOS)

Electro-optic sampling of terahertz pulses relies on the linear electrooptic effect, also known as the Pockel's effect, which describes a change in material refractive index under an applied electric field. Like optical rectification, electro-optic sampling is also a nonlinear optical process, where the strength of the interaction is dependent of the second order electric susceptibility of the detection material. The following discussion is based off an informative book chapter from Ingrid Wilke and Suranjana Sengupta.[20]

The Pockel's effect only exists in materials which do not possess a center of inversion in their crystal symmetry (that is, materials which are non-centrosymmetric), as well as in materials whose symmetry breaks under a relevant stimulus (such as an external electric field).

Zincblende $\bar{4}$3m cubic crystal structures, like those of ZnTe, GaP, GaAs, and InP, possess the requisite symmetry as well as large electro-optic coefficients which determine the strength of the refractive index change from the incident THz pulse. As the optical probe pulse colinearly propagates through EO crystal at the same time as the THz electric field, the probe becomes modulated by the phase delay created from the change in crystal refractive index. This phase delay (Γ) is specifically related to the r_{41} electro-optic in these zincblende crystals through the relation:

$$\frac{2\pi n_0^3 r_{41} E_{THz} L}{\lambda}$$

where λ is the wavelength of the optical probe, L is the crystal thickness, and E_{THz} is the THz electric field. As with all nonlinear optical processes, this interaction occurs specifically under phase-matched conditions between the optical pulse and the THz field, which is described by the same coherence length used in the optical rectification discussion presented in section 2.3.1. Due to this phase-mismatch, thinner crystals generally yield higher bandwidths while thicker crystals lead to higher detection amplitudes. We use <110>-oriented ZnTe and GaP crystals with 3.9 pm/V and 0.97 pm/V r_{41} EO coefficients, respectively, at 800 nm.

Electro-optic changes to the 800 nm beam were collected by a balanced detection scheme. After the EO crystal, the optical probe is sent through a quarter wave plate and a polarizing beam splitting cube to send the orthogonal polarization components

into separate silicon photodiodes. The current signals from the photodiodes are sent into the lock-in amplifier and subtracted. With the THz beam blocked, the quarter wave plate is used to make the 800 nm beam as circularly polarized as possible and therefore produce a baseline around zero amplitude signal. As the probe line scans the measurement window, the optical pulses experience a THz-induced birefringence in the EO crystal that then rotates the probe polarization and changes the relative intensity in the photodiodes. The intensity change seen by the photodiodes was derived by Planken et al.[33] as:

$$\Delta I(\alpha, \varphi) = I_p \frac{\omega n^3 E_{THz} r_{41} L}{2c} (\cos(\alpha) \sin(2\varphi) + 2 \sin(\alpha) \cos(2\varphi))$$

where L is the crystal length, I_p is the probe intensity, c is the velocity of light in vacuum, and ω is the angular frequency of the probe pulse. The detection method is accurate for the range of THz field strengths in a given EO crystal which are not strong enough to induce additional nonlinear optical effects. While EO crystals are a robust, reliable, and easily implemented solution for THz generation and detection, they possess strong transverse optical phonon absorptions which greatly reduce the useable bandwidths to generally below 3 THz for ZnTe and 6 THz for GaP for moderate THz field strengths (<100 kV/cm) and are quite sensitive to signal saturation at high THz field strengths.

2.5.2 Air-Biased Coherent Detection (ABCD)

In contrast to EOS, bandwidths in air-biased coherent detection (ABCD) are often limited only by the surrounding optics and input powers. The ABCD method uses

the inert atmosphere of the THz spectrometer (i.e., nitrogen or dry air) to generate nonlinear optical interactions between the probe and THz pulses. While it is possible to back calculate ultrabroadband THz spectra in EOS methods, after employing approximations for the crystal response and navigating strict phase matching conditions and testing for saturation effects, ABCD is by far the most widely employed technique to measure the THz pulse directly and coherently. In principle, ABCD capability is only limited to the input pulse duration and optical power since there is no damage threshold or counteracting effect to impede THz detection. As with the section on two-color plasma, the following discussion is referenced from the highly relevant thesis of Alessandro Tomasino.[26]

Air-biased coherent detection leverages both electric and THz field-induced second harmonic generation (EFISH and TFISH, respectively) to measure phase-sensitive changes to a local oscillator (optical probe). Specifically, the EFISH and TFISH processes are both third order nonlinear effects that describe the breakdown of isotropy in a centrosymmetric substance under an applied electric field. This transient anisotropy enables the second order nonlinear process of SH generation for an optical pulse traveling through the biased medium:

$$E_{DC}^3 \chi_e^{(3)} \rightarrow \chi_e^{(2)}$$

In the case of EFISH, the electric field bias is static, whereas in TFISH the electric field bias is approximately constant within a single cycle of the optical probe (1 THz $\ll$ 374 THz (800 nm) in our setup). The spatial and temporal overlap of the electric

field (THz or DC) and optical probe can be described as a four-wave mixing process (Kerr effect) where the dominant output is specifically from a difference frequency process. The SH generation signal, then, can also be termed as a DFG signal ($2\omega_p = \omega_{DFG} + \omega_{THz}$).

In ABCD, a high voltage electric field is applied to an air gap between two electrodes where a weak optical probe is made to focus. The 800 nm optical probe is converted into 400 nm by static electric field induced DFG in the anisotropic air layer, while the THz pulse is also made to focus into the electrode gap. The simultaneous electric bias fields create an intensity dependence on the DFG signal modeled as:

$$I_{DFG}^{total} \propto (E_{DFG}^{total})^2 = \left(\chi_{e\,xxxx}^{(3)} I_P\right)^2 \left[E_{THz}^2 + \left(E_{bias}^{DC}\right)^2 \pm 2E_{THz}E_{DFG}^{total}\right]$$

where $\chi_{e\,xxxx}^{(3)}$ is the third order susceptibility when all three waves have the same polarization along the x-axis, and IP is the intensity of the 800 nm probe light. The sign dependence between electric fields represents their phase difference. At this point, we can modulate the static bias field at half the fundamental laser frequency to eliminate the incoherent terms above to yield:

$$I_{DFG}^{total} \propto 2(\chi_{e\,xxxx}^{(3)} I_P)^2 E_{bias}^{AC} E_{THz}$$

where E_{bias}^{AC} is the modulated electric field, and the resulting DFG 400 nm signal is measured by a Thorlabs PMM01 photomultiplier tube. A lock-in amplifier reads the photomultiplier tube current at the modulation frequency. The E_{bias}^{DC} is oscillating at

twice the modulation frequency and therefore not picked up by the lock-in amplifier. The heterodyne scheme constructed through E_{bias}^{AC} allows for coherent detection at any bias level, which allows for low-to-modest probe fluences for strong detection (~70 µJ in our case). From this configuration, we see how there are no additional influences on the detection capability except for the probe pulse duration. That is why ABCD methods have demonstrated bandwidths as high 100 THz.[24]

Figure 2.15 shows the nitrogen atmosphere time- and frequency-domain spectra of our custom spintronic THz emitter on three different detection methods. Specifically, we can compare the pulse shapes and frequency bandwidths detected by electro-optic sampling on a 700 µm thick ZnTe crystal and 100 µm thick GaP crystal, as well as by air biased coherent detection using 1 mm wide electrodes biased so that the air gap was near breakdown voltage (e.g., 18-20 kV/cm). We observe ultrabroad bandwidths (≥10 THz) from ABCD while both EOS methods exhibit strong phonon absorption at higher frequencies. The time-domain spectra from both GaP EOS detection and ABCD show "clean" single cycle pulse shapes (no oscillatory features) with short temporal widths, indicating wide frequency bandwidths. However, the ABCD spectra are much stronger in amplitude than the GaP EOS spectra (not shown due to normalization), which accounts for the greater signal-to-noise, and thus available power, at higher frequencies. In practice, for common THz-TDS experiment setups, the available THz signal is limited by various noise and error. We include a hypothetical threshold in Figure 2.15 to indicate where these noise limitations, solely from our measurement experience, often prohibit accurate THz
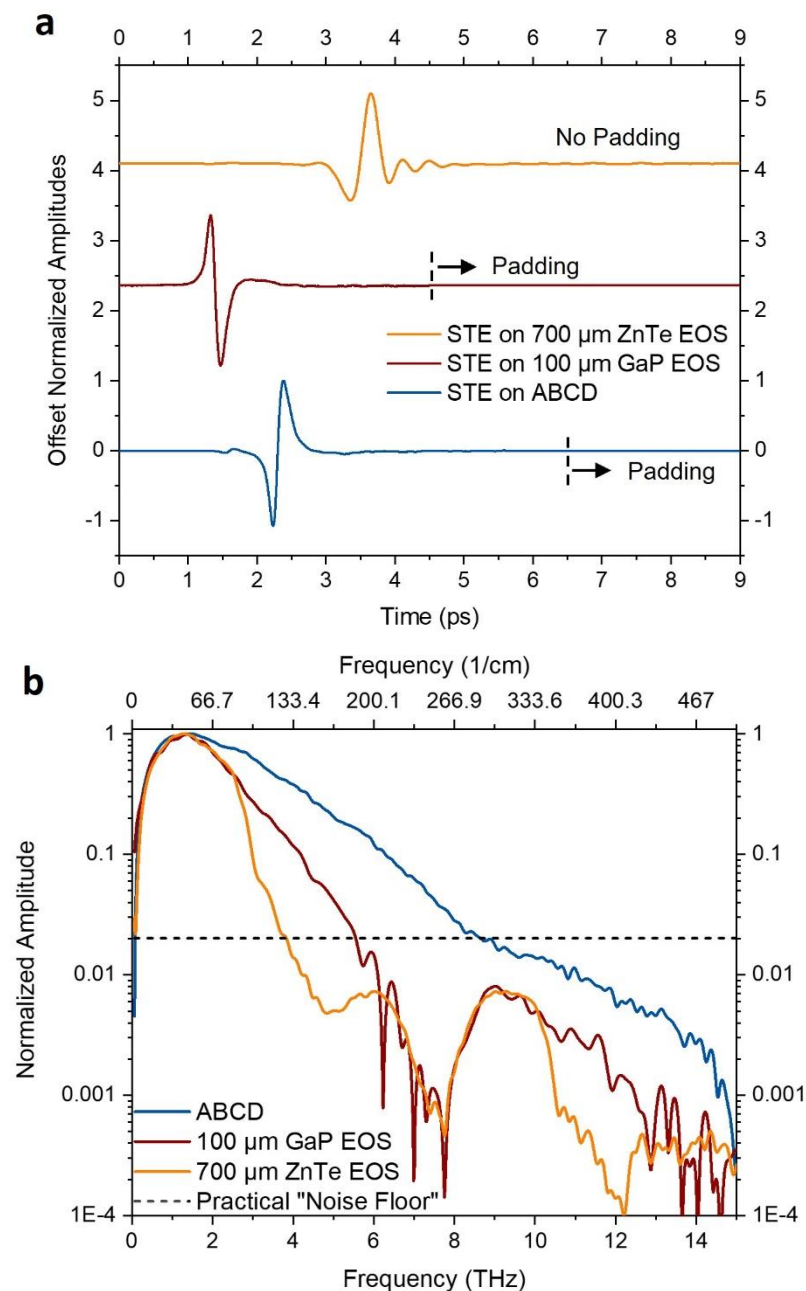
Figure 2.15. Terahertz time-domain (a) and frequency-domain (b) spectra comparing popular detection methods applied to a pulse from a custom spintronic terahertz emitter (STE). All spectra are normalized to their own max amplitudes and processed without a windowing function. A practical "noise floor" is suggested as an example threshold of typically useable power for accurate THz spectroscopy in common experiments. We also demonstrate padding of time-domain spectra with zeros to desired temporal lengths for increased frequency resolution (Sec. 2.6.2).

analysis at higher frequencies. Though anecdotal, this practical "noise floor" can give the reader a better idea of what to expect from THz-TDS analysis across diverse experimental setups. Of course, proper mitigation of error sources, as well as tailored sample preparation, can dramatically improve the analysis bandwidth for any detection method.

2.6 Processing THz Spectra

Several important processing steps are necessary to produce high quality frequency-domain transmission spectra which can be analyzed to yield complex material parameters. For instance, the raw time-domain traces are calibrated, averaged, windowed by an apodization function, Fourier transformed, and characterized for standard deviation properties before preparing the THz transmission spectrum for analysis. At this point, it is intuitive to understand how sometimes subtle differences within the THz emission, interaction, and detection mechanisms can lead to significant impacts on resulting data through important spectrometer features like bandwidth, accuracy, strength, resolution, and more. Even though the processing and characterization of THz spectra are vital to understanding limitations within the data or spectrometer, reporting of this information is not yet standard practice in THz fields. More rigorous interpretation of data collected from spectrometers across various labs necessitates the transparency of both the processing procedures and characterization metrics. To that end, we now discuss in detail how we convert raw

time-domain spectra into analysis ready frequency-domain transmission data. All the data processing and analysis occurs in a series of python scripts written by the author for this purpose (see Appendix B for a guide to this script construction).

2.6.1 Delay Stage Considerations

In our setup, the probe pulse is swept over the terahertz pulse at a constant speed, typically 10-50 µm/s, using a mechanical delay stage. The chosen temporal window (e.g., 6.7 ps or ~1 mm delay line distance) can be scanned an arbitrary number of times to produce a well-averaged time-domain spectrum. Mechanical delay stages, however, can incur a nonzero amount of jitter in the probe pointing and pulse arrival times between scans. This jitter manifests as error in the THz spectral amplitude and phase, respectively. For instance, the pointing jitter imposes misalignment in the spatial overlap between the probe and THz beams on the detector, which in turn modulates the signal amplitude. Additionally, the inherent beam drift in the laser output, due to thermalization of the laser optics over time, can exacerbate the amplitude error. This type of error can be ameliorated with the proper choice of scanning characteristics, such as the number of scans and the scanning speed. If the inherent laser drift is stable over the full experiment time, for example, higher averaging from slower speed scans will generally produce less standard deviation in the amplitude.

Delay line positioning jitter, on the other hand, induces error in the phase component of the THz pulse. Positioning jitter can arise from various aspects of delay stage

operation, such as inconsistent acceleration into constant scanning speed or small variations (mechanical or electrical) in the "start" and "stop" positions. Jitter of this nature produces time-domain spectra where the THz pulses are shifted forwards and backwards relative to their "true" position on the time axis. The uncertainty around this absolute THz pulse temporal position can lead to large phase error in the final transmission spectrum. While highly refined delay lines can provide more accurate and reliable time-axis measurements, costs of these devices can be prohibitive. To mitigate the phase error in our setup, we capture absolute delay positions of the sample and reference THz pulses by briefly, but finely, stepping the probe pulse around a sharp feature on each THz pulse, for example a peak or inflection (from an amplitude sign change). The absolute delay line positions are used to calibrate the temporal distance between the reference and sample spectra which greatly enhances the accuracy of our measurements. Incorporation of this phase calibration is discussed in more detail in subsequent sections.

2.6.2 Averaging, Padding, and Windowing

In a typical THz-TDS experiment, the processed time-domain spectra are formed from an average of many individual scans which are first baseline corrected so that the noise floor preceding the THz pulse starts as close to zero as possible. Changes in the noise floor could arise from baseline offsets through the generation or detection mechanisms, and the baseline correction allows for proper estimations of the field amplitude if the correction is applied consistently. Another important step before

averaging the scans together is the phase alignment of all scans to a representative trace. For instance, in a dataset containing 40 sample scans of THz time-domain spectra, the first THz trace can be used to set a relative time axis around which the other 39 traces are temporally shifted forwards or backwards to resolve temporal jitter. Given an unambiguous feature in the THz pulse, such as the point between the minimum and maximum pulse peaks where the signal amplitude is equal to zero (referred to as the inflection point), the alignment of all traces can dramatically reduce error in the average pulse shape and overall phase deviation. The THz pulse shifting, and subsequent time-domain processing, is accomplished by interpolating each time trace onto an arbitrary time axis to facilitate precise and consistent alignment of the scans. The interpolated and aligned scans are averaged together before subsequent padding and apodization (windowing). This method is only valid for both reference and sample scan datasets when precise calibration measurements (see previous section) are performed as well.

When measuring the THz pulse, care is taken to choose an adequately long time-axis so that the THz signal falls to the noise floor within the scan range. In doing so, we can approximate the THz trace as an arbitrarily long scan by adding zeros after the experimental range (Figure 2.1x). The benefit of this 'padding' on the measured THz scan is in artificially enhancing the resolution of the resulting frequency-domain spectrum. Too much padding of the data, however, can result in inaccurate spectra interpretations. In our data processing, the spectra were often padded out to 50 ps, which results in a frequency resolution (or data spacing) of 20 GHz. Separately, we

can multiply the averaged THz trace with a windowing function, which is often used to exclude unwanted signal contributions from, for instance, etalons or water absorption features. Apodization has a rich history in digital signal processing, and we typically use a Tukey window function in our data processing to make the data continuous between the experimental noise floor and the padded zeros. Strong caution must be used when deciding on the windowing range and function type, though, as it is very easy to modulate the experimental spectral shape such that the resulting features in the frequency spectra are artificially broadened or frequency shifted. That said, windowing can be a powerful tool for investing specific temporal signals by isolating them from the rest of the data.

The averaged, windowed time-domain spectra are then Fourier transformed, using standard Fast FT algorithms, to produce frequency-domain THz spectra. This processing routine is carried out on the reference dataset first before the subsequent sample traces. We take advantage of the processing order to perform an important phase calibration of the sample time-domain average relative to the reference. That is, we use the previously acquired absolute temporal positions of the THz pulses to manually, temporally shift the sample spectra at that calibrated distance away from the reference. This calibration procedure has become invaluable for our ability to reliably measure phase shifts in thin films, for instance, where the shifts can be as small as $\lesssim 1$ fs. To understand the reliability of our calibrated data across the experimental bandwidth, we can perform characterizations of the standard deviation behavior.

2.6.3 Standard Deviation, SNR, and DNR

Quantitative analysis of the error present in our measurements is vital to understand in what portion of the collected THz spectrum we can be most confident. The work of Withayachumnankul and Naftaly provide some excellent references for these types of characterizations, and here we will limit our scope to discussing standard deviation, signal-to-noise ratio (SNR), and the dynamic-noise-range (DNR).[34] The standard deviation of the data must be processed separately for the time-domain and frequency-domain data because the Fourier transform of the time-domain spectra does not translate to the frequency-domain. Therefore, instead of only processing the average THz time-domain spectra as in section 2.6.2, we now pad and apply apodization to every scan before taking their Fourier transforms. The standard deviation is then calculated from frequency-dependent fluctuations around the average frequency spectra. The standard deviation is a useful property to understand the experimentally induced error in the measurement, as well as to calculate the absolute measurement sensitivity over the frequency range from the SNR:

$$SNR = \frac{\bar{E}}{s_E}$$

where $\bar{E}$ is the average amplitude value. The SNR represents the minimum detectable signal change and thus is critical to justifying any interpretations of weak spectral features. In a complementary fashion, the DNR tells us about the maximum possible signal change detectable by the measurement:

$$DNR = \frac{E_{\text{max}}}{N_{rms}}$$

where N_{rms} represents the root-mean-square noise floor of the instrument. The DNR is often calculated to understand the useable bandwidth of the THz spectrometer. Reports of THz-TDS measurements with especially weak or ambiguous spectral features should include these characterization data to provide a deeper understanding about the spectrometer influence on the analyzed sample behavior.

2.6.4 Transmission Spectrum Preparation

The last processing step before extracting material parameters is the preparation of the transmission amplitude and phase spectra. As we previously discussed, the experimental transmission spectrum is acquired by dividing the complex-valued frequency-domain spectra of the sample by the reference. This division yields a transmission response, $T(\omega)$, which is composed of an amplitude coefficient, $A(\omega)$, that represents the transmission amplitude ratio, and a phase term, $\Delta\phi(\omega)$, that represents the shift of the THz light as it passes through the sample.

$$T(\omega) = \frac{E_{sam}(\omega)}{E_{ref}(\omega)} = A(\omega)e^{i\Delta\phi(\omega)}$$

$$A(\omega) = |T(\omega)|$$

$$\Delta\phi(\omega) = \arg(T)$$

where we can isolate these components of the transmission spectrum by taking its magnitude and argument accordingly. While this level of processing is sufficient for

the amplitude, we must look at the phase shift processing a bit more carefully. The methodology presented here largely follows an excellent tutorial by Jepsen for processing THz-TDS phase.[35] Firstly, the phase values of a sufficiently thick sample which result from a generic argument function are often wrapped between values of π and $-\pi$, creating discontinuous jumps across the frequency spectrum that would hinder the extraction of material parameters. After unwrapping the phase by adding or subtracting multiples of 2π, another issue presents itself in the accuracy of the low frequency phase information. In THz-TDS analysis, we assume that at $0\,Hz$ the phase shift is also zero. We experience a large degree of noise, however, at the ends of our experimental bandwidth that can induce 2π phase offsets. Similar to the issue with phase unwrapping, these low frequency phase offsets must be accounted for in order to prevent incorrect material parameter extraction. The offset is accomplished by using a portion of the THz response from the lower frequencies with highest SNR and minimal absorption features to extrapolate a straight line down to $0\,Hz$. If necessary, we can then manually subtract or add the multiple of 2π from the entire phase shift spectra. In addition to these concepts, Jepsen introduces a more rigorous procedure for acquiring the correctly processed phase spectra. Encouragingly, though, our experience tells us that the conventional processing procedures described here typically yield the same result as the more rigorous processing routine. In any case, we now have the requisite amplitude and phase spectra for the isolated THz transmission response through the sample, and we can finally begin to analyze these data for material properties.

2.7 Extraction of THz Material Parameters

While the acquisition of THz spectra is a valuable for understanding low-energy infrared excitations in all kinds of matter, the ability to extract the full complex material parameters without invoking contact-based methods or Kramers-Kronig relations is one of the most advantageous features of this spectroscopy. This section represents the last phase of THz-TDS, where we apply analytical solutions or numerical fitting to the experimental THz spectra, through the predetermined transfer functions, to recover intrinsic sample properties. The scope of these developments will continue to be focused on transmission measurements.

2.7.1 Analytical Solutions to the Transfer Function

The opportunity to apply an analytical formula in data fitting is a large advantage in both computational time and interpretation of the results. We can derive analytical forms of the transfer function for samples that are very weakly absorbing and mounted at normal incidence to the THz beam.[34] The simplification of the generalized transfer function for a single layer slab, for instance, leads to the elimination of polarization dependency (in the case of an isotropic system), angle sensitivity, and the inclusion of etalons (in a sufficiently thick sample or narrow time window):

$$H(\omega) = \frac{4n_s(\omega)}{(n_s(\omega) + 1)^2} \cdot e^{-k_s(\omega)\frac{\omega l}{c}} \cdot e^{-j[n_s(\omega)-1]\frac{\omega l}{c}}$$

where $n_s(\omega) + i * k_s(\omega) = \tilde{n}_{sample}(\omega)$ of some thickness l. We see that only the real component of the sample refractive index is used for the Fresnel reflection coefficient, and that $n_{ref} = n_{nitrogen} = \sim 1$. From here, we can simply take the argument and magnitude of the analytical function to isolate the behavior of the real and imaginary refractive index components, respectively.

$$\angle H(\omega) = -(n_s(\omega) - 1)\frac{\omega l}{c}$$

$$n_s(\omega) = 1 - \frac{c}{\omega l}\angle H(\omega)$$

$$\ln(|H(\omega)|) = \ln\left(\frac{4n_s(\omega)}{(n_s(\omega) + 1)^2}\right) - \kappa_s(\omega)\frac{\omega l}{c}$$

$$\kappa_s(\omega) = \frac{c}{\omega l}(\ln\left(\frac{4n_s(\omega)}{(n_s(\omega) + 1)^2}\right) - \ln(|H(\omega)|)$$

$$\alpha_s(\omega) = 2\frac{\omega\kappa_s(\omega)}{c}$$

The ability to invert this transfer function to produce direct results for n_s and κ_s is a feature of analytical solutions and thus demonstrates their utility in practical THz measurements.[34] We can also use the simplified forms of this transfer function to qualitatively understand how the real component of the refractive index n_s is proportional to the phase shift of the transmission spectra, while the imaginary component κ_s is proportional to the magnitude. We also observe this trend of proportionality in the application of generalized transfer functions from section 2.2.3. It can be helpful to use the experimental transmission spectra as a first pass

assessment of the probable material parameter shapes and trends before any analysis steps. The use of analytical solutions is most suited for >10 μm thick THz transparent materials often implemented as windows and substates, such as high-resistivity silicon, insulating gallium arsenide, silicon nitride, z-cut quartz, fused silica, manganese oxide, sapphire, Teflon, high density polyethylene, diamond, and more. The analytical solutions can be advantageously prioritized in cases where the appropriate sample and measurement scheme are implemented.

2.7.2 Numerical Fitting of the Transfer Function

In cases where the sample properties are unknown, strongly absorbing, or where other nuances must be considered, it is ideal to begin instead with the generalized transfer functions. In contrast to the analytical solutions, the generalized transfer functions present the well-known inversion problem in spectroscopic methods, where a model cannot be directly inverted to solve for certain unknowns (e.g., n_s and κ_s). To apply the generalized model to experimental data requires the process of essentially guessing refractive index values at each frequency point and comparing the model transmission function results to the amplitude and phase data of the experimental transmission spectra. More specifically, an error function is derived such that the fitting is deemed accurate if the error between the transfer function and the transmission spectrum are below a valid threshold (e.g., 10^{-10}).

$$\delta(n, \kappa) = \delta A^2 + \delta \phi^2$$
$$\delta A = \ln(|T(\omega)|) - \ln(|T_{meas}(\omega)|)$$
$$\delta \phi = \arg(T(\omega)) - \arg(T_{meas}(\omega))$$

This error function was implemented for THz analysis by Duvillaret in 1996 and still maintains popularity in current applications of THz spectroscopy.[36-37] We see that the error is frequency-resolved and nonlinearly dependent on both the amplitude and phase differences from the transfer function. Given this metric, we can employ one of the many existing numerical fitting algorithms to minimize transfer function error at every data point in our useable bandwidth. The data in this thesis was extracted using a Nelder-Mead fitting algorithm. An example of optical parameter extraction using numerical fitting is shown in Figure 2.16. After preparing the transmission function amplitude and phase offset as previously described, we iterate the numerical fit at each frequency in our dataset until the error between our fit and the data is satisfactorily low. The undoped, ~280 μm thick silicon wafer used in this example represents a common substrate material employed in THz-TDS. Thus, acquiring the data in Figure 2.1x is often a prerequisite step before sample analysis can take place. The extracted refractive index of this silicon wafer is expectedly non-dispersive with a real component around 3.42.

To minimize pitfalls or breaks in the fitting process it is important to identify sufficient initial guesses for the parameter extraction. It is also a well-known fact that parameter extraction in THz-TDS is highly sensitive to the accuracy of sample thickness. Thickness uncertainties of even 1% can yield significantly different
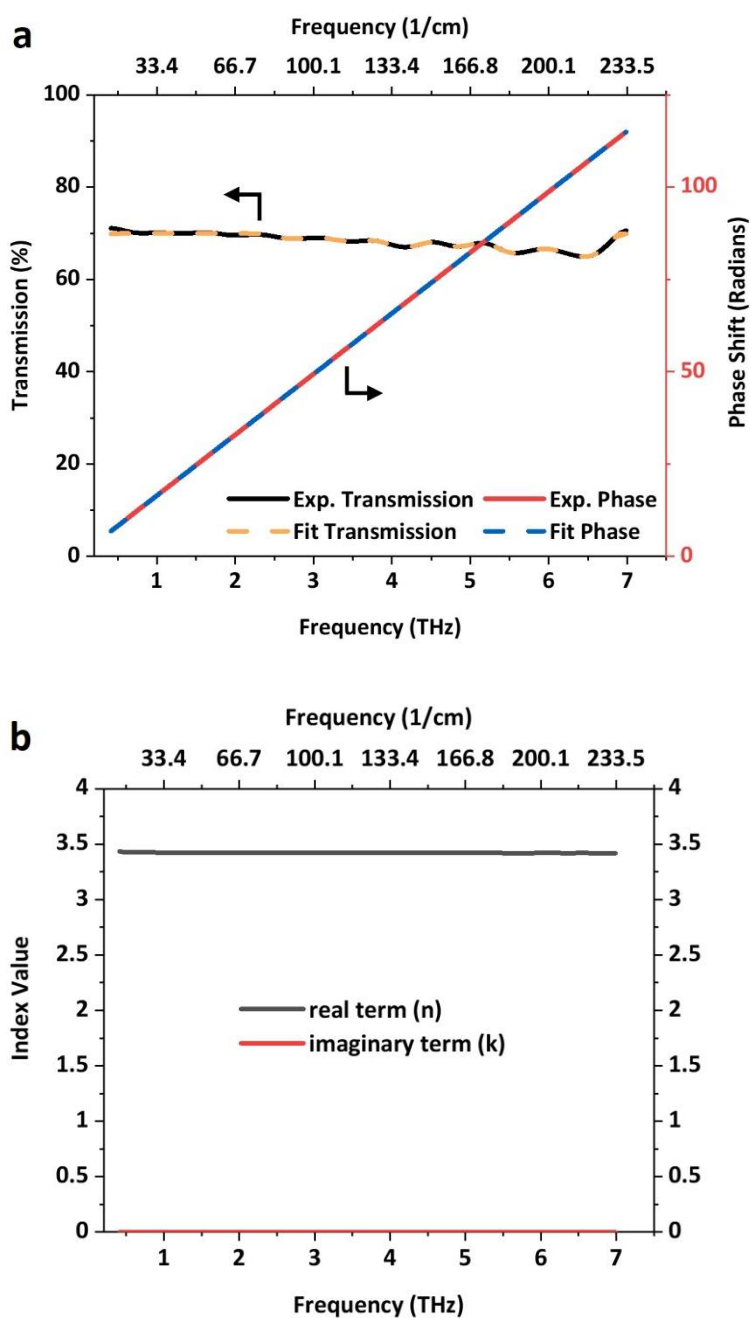
Figure 2.16. Numerical fitting parameter extraction applied on ~280 μm thick undoped silicon wafer with broadband frequency-domain spectra (a) and non-dispersive refractive index solution (b).

refractive index values depending on the sample properties. From a successful fitting, the complex refractive index output represents the experimental material parameters of the sample given that specific thickness. Alternatively, if the refractive index is already known, the numerical fitting approach can also be used to find the sample thickness quite accurately, as is used in the characterization of paint layers in automotive and aviation industries.[38] It is not recommended, however, to fit for thickness and refractive index at the same time, as this situation could lead to less accurate determination of both properties. Overall, the numerical fitting approach provides a brute force method of extracting material properties by iteratively guessing refractive index (or permittivity or conductivity) values across the full spectral range. In themselves, these experimental parameters are valuable for examining the charge carrier behavior in the system through resonances and other spectral features. An even deeper analysis, however, can be accomplished with an additional and final modeling step.

2.7.3 Applying Physical Models to Experimental Parameters

Once the "experimental" material parameters are extracted from analytical formulae or numerical fitting, we can apply well-established physical models to better characterize the THz spectra. While the specific model chosen should consider the fundamental nature of THz excitation in the sample, some of the most common models for materials are the Drude and Lorentz oscillator models. These functions describe different cases of charge transport based on classical laws of motion.

In the Drude model, electrons in a solid are treated as a free electron gas where they are not bound to specific atoms but can move freely throughout. These electrons experience collision events with lattice ions and other electrons which cause instantaneous and random scattering. We use Newton's equation of motion to describe the movement of these electrons under an applied electric field E:

$$m_e \frac{dv}{dt} = -eE - m_e \frac{v}{\tau}$$

where m_e is the electron mass, v is the electron velocity, e is the electron charge, and τ is the average time between collisions. By setting the left-hand side equal to zero, we can find a steady-state drift velocity, which describes the average drift experienced by the electrons under the electric field. We can then use the current density relationship and Ohm's law to arrive at the electrical conductivity, J, of the material:

$$J = -nev_d = -ne\left(-\frac{e\tau}{m_e}E\right) = \sigma E$$

$$\sigma = \frac{ne^2\tau}{m_e}, or \ \sigma = \frac{ne^2}{m_e}\frac{1}{\Gamma - i\omega} \ for \ E \ \propto e^{-i\omega t}$$

where J is the current density, n is the concentration of electrons, and Γ is the scattering rate $1/\tau$. Despite the classical approximations of the Drude model, it is an enduringly useful function for modeling the behavior of metals. At low optical frequencies, the Drude model predicts that a material with a large concentration of

free carriers will act like a perfect reflector. At high frequencies, however, the Drude contribution to the conductivity is expected to be almost non-exist. These two scenarios describe simple metallic and insulating systems moderately well, and the point at which the material switches from one state to the other is known as the plasma frequency, ω_p. This frequency is specifically defined for when the real part of the material's dielectric permittivity goes to zero, which can be approximated as:

$$\omega_p = \sqrt{\frac{ne^2}{\varepsilon_0 m_e}}$$

Below the plasma frequency, light is not able to pass the through the material and instead will be reflected. Above this frequency, the material acts transparent. The Drude model can easily be combined with the Lorentz oscillator model through a simple addition of terms.

In contrast to the Drude model which considers only instantaneous and random scattering of charges, the Lorentz oscillator model is used to describe the harmonic resonance of a material to oscillating electric field. In this analogy, an electron within an atom or molecule is treated as a charged particle connected to a spring. The restoring force of the spring represents the electron's response to an electric field. We can use the previously presented material electric polarization P to find the relationship of the dielectric permittivity with the applied electric field E. The oscillating form of the dielectric permittivity is then:

$$\tilde{\varepsilon} = \varepsilon_\infty + \frac{\omega_p}{(\omega_o^2 - \omega^2) - i\omega/\tau}$$

where ε_∞ is the background dielectric constant at high frequencies relative to the resonance frequency, ω_0 is the natural oscillator frequency, ω_p is the plasma frequency from before, and τ is the relaxation time. In this complex-valued formalism, the imaginary part represents the time delay between the driving electric field and the response of the electronic response of the material. As with the Drude model, despite classical approximations, the Lorentz oscillator model does an often-adequate job at characterizing resonant features within THz spectra (Figure 2.17). Absorptions from phonons or other quasiparticles are well represented by this simple function, and for samples which display both metallic and resonantly absorbing features, we can easily combine both models. Another useful form of the Lorentz oscillator model is shown below, with ε_{st} representing the low frequency, or "static" dielectric constant, S representing the oscillator strength, and $\gamma = 1/\tau$.

$$\tilde{\varepsilon}_{total} = \varepsilon_\infty + (\varepsilon_{st} - \varepsilon_\infty) \sum \frac{S * \omega_o}{(\omega_o^2 - \omega^2 - i\gamma\omega)}$$

We can implement these two widely useful models to directly fit the extracted THz material parameters to understand either the Drude-like or Lorentz-like nature of the charge carriers present in the system. Furthermore, we can use these or any similar physical model to bypass the numerical fitting all together. For instance, we would "parametrize" the fitting to occur through physical model inputs only, instead of
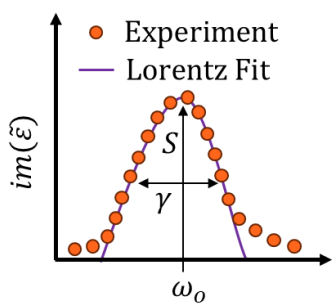
Figure 2.17. Representation of Lorentz oscillator model fit to resonance peak.

iterating at each frequency point to recover the exact features of the experimental spectrum. The benefit of this parameterized approach is that one can significantly reduce fitting times due to fewer variables that need to be fit across the spectrum, and that one can directly analyze the fitting quality of the physical model to the experimental spectrum. In any case, this section represents the last section in the THz analysis phase, where we now have the requisite tools to investigate an immense variety of samples with unknown properties.

CHAPTER 2 BIBLIOGRAPHY

1. Lüpke, F.; Cuma, D.; Korte, S.; Cherepanov, V.; Voigtländer, B. Four-Point Probe Measurements Using Current Probes with Voltage Feedback to Measure Electric Potentials. *J. Phys. Condens. Matter* **2018**, *30* (5), 054004. https://doi.org/10.1088/1361-648X/aaa31e.

2. Plociennik, P.; Zawadzka, A.; Korcala, A.; Wisniewski, K.; Lukasiak, Z. Temperature Dependent Conductivity of Thin Films Perovskite Obtained by PVD Method. In *2019 21st International Conference on Transparent Optical Networks (ICTON)*; IEEE, 2019; pp 1–1. https://doi.org/10.1109/ICTON.2019.8840323.

3. Beard, M. C.; Turner, G. M.; Schmuttenmaer, C. A. Transient Photoconductivity in GaAs as Measured by Time-Resolved Terahertz Spectroscopy. *Phys. Rev. B* **2000**, *62* (23), 15764–15777. https://doi.org/10.1103/PhysRevB.62.15764.

4. Pattengale, B.; Neu, J.; Ostresh, S.; Hu, G.; Spies, J. A.; Okabe, R.; Brudvig, G. W.; Schmuttenmaer, C. A. Metal–Organic Framework Photoconductivity via Time-Resolved Terahertz Spectroscopy. *J. Am. Chem. Soc.* **2019**, *141* (25), 9793–9797. https://doi.org/10.1021/jacs.9b04338.

5. Yamashita, G.; Matsubara, E.; Nagai, M.; Kim, C.; Akiyama, H.; Kanemitsu, Y.; Ashida, M. Sensitive Monitoring of Photocarrier Densities in the Active Layer of a Photovoltaic Device with Time-Resolved Terahertz Reflection Spectroscopy. *Appl. Phys. Lett.* **2017**, *110* (7). https://doi.org/10.1063/1.4975631.

6. Hopfe, V.; Bussemer, P.; Richter, E.; Klobes, P. P- and s-Polarized FTIR Reflectance Spectroscopy at Oblique Incidence by Kramers-Kronig Transformation. *J. Phys. D. Appl. Phys.* **1992**, *25* (2), 288–294. https://doi.org/10.1088/0022-3727/25/2/024.

7. Chen, X.; Yin, G.; Zhao, N.; Yang, R.; Xia, M.; Feng, C.; Chen, Y.; Dong, M.; Zhu, W. Turbidity Compensation Method Based on Mie Scattering Theory for Water Chemical Oxygen Demand Determination by UV-Vis Spectrometry. *Anal. Bioanal. Chem.* **2021**, *413* (3), 877–883. https://doi.org/10.1007/s00216-020-03042-4.

8. Neu, J.; Schmuttenmaer, C. A. Tutorial: An Introduction to Terahertz Time Domain Spectroscopy (THz-TDS). *J. Appl. Phys.* **2018**, *124* (23). https://doi.org/10.1063/1.5047659.

9. Withayachumnankul, W.; Fischer, B. M.; Lin, H.; Abbott, D. Uncertainty in Terahertz Time-Domain Spectroscopy Measurement. *J. Opt. Soc. Am. B* **2008**, *25* (6), 1059. https://doi.org/10.1364/JOSAB.25.001059.

10. Withayachumnankul, W.; Fischer, B. M.; Abbott, D. Material Thickness Optimization for Transmission-Mode Terahertz Time-Domain Spectroscopy. *Opt. Express* **2008**, *16* (10), 7382. https://doi.org/10.1364/OE.16.007382.

11. Ammerman, S. E.; Jelic, V.; Wei, Y.; Breslin, N. J.; Hassan, M.; Everett, N.; Sun, Q.; Pigendoli, C. A.; Ruffieux, P.; Fasel, R.; Cocker, T. L. THz-STM of Atomically Precise Graphene Nanoribbons. In *2020 45th International Conference on Infrared, Millimeter, and Terahertz Waves (IRMMW-THz)*; IEEE, 2020; pp 1–2. https://doi.org/10.1109/IRMMW-THz46771.2020.9370853.

12. Dorney, T. D.; Baraniuk, R. G.; Mittleman, D. M. Material Parameter Estimation with Terahertz Time-Domain Spectroscopy. *J. Opt. Soc. Am. A* **2001**, *18* (7), 1562. https://doi.org/10.1364/JOSAA.18.001562.

13. Oughstun, K. E.; Palombini, C. L. Fresnel Reflection and Transmission Coefficients for Temporally Dispersive Attenuative Media. *Radio Sci.* **2018**, *53* (11), 1382–1397. https://doi.org/10.1029/2018RS006646.

14. Carnio, B. N.; Attiaoui, A.; Assali, S.; Moutanabbir, O.; Elezzabi, A. Y. Extracting the Complex Refractive Index of an Ultrathin Layer at Terahertz Frequencies With No Prior Knowledge of Substrate Absorption Loss. *IEEE Trans. Terahertz Sci. Technol.* **2022**, *12* (4), 385–391. https://doi.org/10.1109/TTHZ.2021.3140196.

15. Landry, J.P. Optical oblique -incidence reflectivity difference microscopy: Application to label-free detection of reactions in biomolecular microarrays. *UC Davis PhD Thesis* **2008**. https://www.proquest.com/docview/304647384.

16. Loata, G. C.; Thomson, M. D.; Löffler, T.; Roskos, H. G. Radiation Field Screening in Photoconductive Antennae Studied via Pulsed Terahertz Emission Spectroscopy. *Appl. Phys. Lett.* **2007**, *91* (23). https://doi.org/10.1063/1.2823590.

17. Zernike, F.; Berman, P. R. Generation of Far Infrared as a Difference Frequency. *Phys. Rev. Lett.* **1965**, *15* (26), 999–1001. https://doi.org/10.1103/PhysRevLett.15.999.

18. Balos, V.; Wolf, M.; Kovalev, S.; Sajadi, M. Optical Rectification and Electro-Optic Sampling in Quartz. *Opt. Express* **2023**, *31* (8), 13317. https://doi.org/10.1364/OE.480339.

19. Nahata, A.; Heinz, T. F. Generation of Subpicosecond Electrical Pulses by Optical Rectification. *Opt. Lett.* **1998**, *23* (11), 867. https://doi.org/10.1364/OL.23.000867.

20. Wilke, I., & Sengupta, S. Nonlinear Optical Techniques for Terahertz Pulse Generation and Detection — Optical Rectification and Electrooptic Sampling. In *Terahertz Spectroscopy: Principles and Applications*. 1st ed., CRC Press, **2007**, 41–72.

21. Schneider, A.; Neis, M.; Stillhart, M.; Ruiz, B.; Khan, R. U. A.; Günter, P. Generation of Terahertz Pulses through Optical Rectification in Organic DAST Crystals: Theory and Experiment. *J. Opt. Soc. Am. B* **2006**, *23* (9), 1822. https://doi.org/10.1364/JOSAB.23.001822.

22. Song, Q.; Lin, Q.; Wang, H.; Zhong, H.; Cai, Y.; Zheng, S.; Chen, Z.; Lu, X.; Zeng, X.; Shangguan, H.; Wang, H.; Xu, S. Efficient Nearly-Circularly-Polarized Terahertz Generation from an Air Plasma Pumped by Collinear and Circularly Polarized Two-Color Laser Fields. *Phys. Rev. A* **2020**, *102* (2), 023506. https://doi.org/10.1103/PhysRevA.102.023506.

23. Kress, M.; Löffler, T.; Eden, S.; Thomson, M.; Roskos, H. G. Terahertz-Pulse Generation by Photoionization of Air with Laser Pulses Composed of Both Fundamental and Second-Harmonic Waves. *Opt. Lett.* **2004**, *29* (10), 1120. https://doi.org/10.1364/OL.29.001120.

24. Sun, W.; Wang, X.; Zhang, Y. Terahertz Generation from Laser-Induced Plasma. *Opto-Electronic Sci.* **2022**, *1* (8), 220003–220003. https://doi.org/10.29026/oes.2022.220003.

25. Fülöp, J. A.; Tzortzakis, S.; Kampfrath, T. Laser-Driven Strong-Field Terahertz Sources. *Adv. Opt. Mater.* **2020**, *8* (3). https://doi.org/10.1002/adom.201900681.

26. Tomasino, Alessandro. Ultra-broadband coherent detection of terahertz pulses via CMOS-compatible solid-state devices. *UNIPA PhD Thesis* **2018**.

27. Rouzegar, R.; Brandt, L.; Nádvorník, L.; Reiss, D. A.; Chekhov, A. L.; Gueckstock, O.; In, C.; Wolf, M.; Seifert, T. S.; Brouwer, P. W.; Woltersdorf, G.; Kampfrath, T. Laser-Induced Terahertz Spin Transport in Magnetic Nanostructures Arises from the Same Force as Ultrafast Demagnetization. *Phys. Rev. B* **2022**, *106* (14), 144427. https://doi.org/10.1103/PhysRevB.106.144427.

28. Rouzegar, R.; Chekhov, A. L.; Behovits, Y.; Serrano, B. R.; Syskaki, M. A.; Lambert, C. H.; Engel, D.; Martens, U.; Münzenberg, M.; Wolf, M.; Jakob, G.; Kläui, M.; Seifert, T. S.; Kampfrath, T. Broadband Spintronic Terahertz Source with Peak Electric Fields Exceeding 1.5 MV/Cm. *Phys. Rev. Appl.* **2023**, *19* (3), 034018. https://doi.org/10.1103/PhysRevApplied.19.034018.

29. Seifert, T.; Jaiswal, S.; Martens, U.; Hannegan, J.; Braun, L.; Maldonado, P.; Freimuth, F.; Kronenberg, A.; Henrizi, J.; Radu, I.; Beaurepaire, E.; Mokrousov, Y.; Oppeneer, P. M.; Jourdan, M.; Jakob, G.; Turchinovich, D.; Hayden, L. M.; Wolf, M.; Münzenberg, M.; Kläui, M.; Kampfrath, T. Efficient Metallic Spintronic Emitters of Ultrabroadband Terahertz Radiation. *Nat. Photonics* **2016**, *10* (7), 483–488. https://doi.org/10.1038/nphoton.2016.91.

30. Matsunaga, T.; Mag-Usara, V. K.; Ejiri, K.; Tetsukawa, S.; Liu, S.; Agulto, V. C.; Nishitani, S.; Nishitani, M.; Yoshimura, M.; Nakajima, M. High Intensity Spintronic Terahertz Emitter with ITO and Microsheet Glass Structure. In *2022 47th International Conference on Infrared, Millimeter and Terahertz Waves (IRMMW-THz)*; IEEE, **2022**; pp 1–2. https://doi.org/10.1109/IRMMW-THz50927.2022.9895759.

31. Zhang, X.; Jiang, Y.; Xu, Y.; Liu, F.; Rui, G.; Wang, A.; Zhao, W. Unidirectional Spintronic Terahertz Emitters with High Efficiency. *Opt. Lett.* **2022**, *47* (24), 6381. https://doi.org/10.1364/OL.476809.

32. Withayachumnankul, W.; O'Hara, J. F.; Cao, W.; Al-Naib, I.; Zhang, W. Limitation in Thin-Film Sensing with Transmission-Mode Terahertz Time-Domain Spectroscopy. *Opt. Express* **2014**, *22* (1), 972. https://doi.org/10.1364/OE.22.000972.

33. Planken, P. C. M.; Nienhuys, H.-K.; Bakker, H. J.; Wenckebach, T. Measurement and Calculation of the Orientation Dependence of Terahertz Pulse Detection in ZnTe. *J. Opt. Soc. Am. B* **2001**, *18* (3), 313. https://doi.org/10.1364/JOSAB.18.000313.

34. Withayachumnankul, W.; Naftaly, M. Fundamentals of Measurement in Terahertz Time-Domain Spectroscopy. *J. Infrared, Millimeter, Terahertz Waves* **2014**, *35* (8), 610–637. https://doi.org/10.1007/s10762-013-0042-z.

35. Jepsen, P. U. Phase Retrieval in Terahertz Time-Domain Measurements: A "How to" Tutorial. *J. Infrared, Millimeter, Terahertz Waves* **2019**, *40* (4), 395–411. https://doi.org/10.1007/s10762-019-00578-0.

36. Duvillaret, F.; Garet, F.; Coutaz, J.-L. A Reliable Method for Extraction of Material Parameters in Terahertz Time-Domain Spectroscopy. *IEEE Journal of*

Selected Topics in Quantum Electronics **1996**, *2* (3), 739–746. https://doi.org/10.1109/2944.571775.

37. Pupeza, I.; Wilk, R.; Koch, M. Highly Accurate Optical Material Parameter Determination with THz Time-Domain Spectroscopy. *Optics Express* **2007** *15* (7), 4335-4350. https://doi.org/

38. Ellrich, F.; Bauer, M.; Schreiner, N.; Keil, A.; Pfeiffer, T.; Klier, J.; Weber, S.; Jonuscheit, J.; Friederich, F.; Molter, D. Terahertz Quality Inspection for Automotive and Aviation Industries. *J. Infrared Milli Terahz Waves* **2020** *41*, 470–489. https://doi.org/10.1007/s10762-019-00639-4.

C h a p t e r   3

SYNTHESIS AND CHARACTERIZATION OF HIGH-QUALITY HYBRID PEROVSKITE THIN FILMS

3.1 Motivation

Anthropogenically-induced climate change is a multifaceted problem which demands diverse, synergistic solutions. Solar energy approaches aim to mitigate harmful reliance on non-renewable resources and reduce greenhouse gas emissions through sustainable fuel and electricity generation. Though enough energy exists in 1.5 hours of global sunlight to power all human electrical demand for over a year, recorded as 18 terawatts of power consumption in 2019[1], we have only recently been able to provide ~3% of our energy needs with photovoltaics (PV). Furthermore, while over 90% of active PV technology is based on silicon (Si), there exists intrinsic challenges in processing the raw silica (SiO_2) materials to manufacture the ultrapure, large area silicon wafers necessary for high-quality solar cells. These challenges lead to industrial methods which, for 1 kg of processed Si, often demand temperatures above 1400°C which can consume 27 kg of carbon and emit ~84 kg of carbon dioxide (CO_2) to the atmosphere.[1] Considering the projected, rapid increase in PV demand, and depleting supply of natural silica deposits (e.g., in the form of sand), it is imperative that we invest in fundamental research on alternative photovoltaic materials such that sustainable energy frontiers can expand.[1-2]

Among the most promising candidates, hybrid organohalide perovskites have demonstrated competitive solar cell efficiencies from remarkably low-cost synthetic routes and also complement existing silicon PV technology in the form of tandem devices by achieving efficiencies surpassing 31%.[3] Technoeconomic analysis of hybrid perovskite PV made from roll-to-roll production through spray-deposition and laser annealing shows remarkably low projected full module costs around $0.15 per watt compared to crystalline silicon module costs around $0.3 per watt.[4] Moreover, the entire fabrication process of hybrid perovskite PV modules can be electrified to facilitate virtually no CO_2 emissions.[5] The greatest barrier to large-scale hybrid perovskite commercialization is undoubtedly their inherent environmental instability to heat, light, water, and oxygen. Overcoming such degradation is thus a major ongoing effort which demands fundamental investigation of perovskite light-matter interactions to guide device-level engineering.

In this chapter, we discuss our efforts to synthesize high quality hybrid perovskite thin films and to perform valuable characterizations of THz dynamics which are known to strongly influence perovskite charge conduction.[6-7] We examine both bulk and two-dimensional (2D) hybrid perovskite structures to reveal optically active phonon excitations which are readily interpreted through published theoretical studies.[8] Furthermore, when synthesized onto 200 nm thin silicon nitride substrates, we uncover a change in the perovskite THz response which effectively increases our detection of the phonon structure in thin films. Rigorous interrogation

of intrinsic hybrid perovskite photodynamics represented in this work is critical to realize their potential in revolutionary renewable energy technology.

3.2 Bulk Hybrid Organic Inorganic Perovskites

The term perovskite is used to categorize a specific crystal structure with ABX_3 stoichiometry, named in honor after the Russian minerologist Lev Perovski. Hybrid organic inorganic perovskite structures incorporate an organic molecule into the A site cation and an inorganic element as the B site cation, typically charged balanced by a halide anion (Fig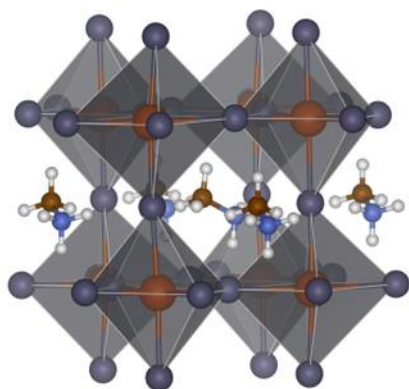ure 3.1).[6-7] Since the 2009 report by Kojima et al.[9] showing 3.8% solar energy conversion efficiency in hybrid perovskite, this research field has produced an expansive forest of semiconducting materials with compelling properties that are highly tunable through their composition. For instance, hybrid perovskites exhibit order of magnitude larger absorption coefficients than silicon, possess >5 µm charge carrier diffusion

Figure 3.1. Crystal structure of methylammonium lead iodide (MAPbI₃) perovskite.

lengths, show carrier lifetimes up to 10 µs, and mobilities up to 40 cm^2/Vs.[10] These materials are easily solution processable with temperatures below 150°C. They also show remarkable tolerance to ionizing radiation, which makes them compelling candidates for space-based photovoltaics when also considering their low mass

density.[11] Since their early development, hybrid perovskite materials have found useful or potential applications as solar cells, LEDs, lasers, photodetectors, nonlinear optical components, energy storage devices, and more.[6-7] An interesting aspect which unites the diverse compositions in this material class is the presence of strong electron-phonon coupling to their excited state dynamics.[6]

Low frequency THz vibrations in hybrid perovskites have been shown to dramatically influence charge-carrier transport and relaxation. Time-resolved optical pump measurements show how resonances in the excited state conduction originate from THz energy excitations.[12] Moreover, time-dependent theoretical calculations have extracted timescales of carrier scattering which result from phonon interactions. Raman and terahertz studies of prototypical hybrid perovskites reveal strong excitations of inorganic octahedral cage bending and rocking modes below ~3 THz (~100 cm^{-1}).[12-13] While now well understood that these vibrational excitations are strongly tied to the charge conductivity behavior, the explicit nature of these THz excitations exhibit nontrivial change with perovskite composition. Moreover, the structure can be tuned to dramatically weaken phonon coupling all together. It is essential, then, to characterize the fundamental structure-function relationships which dictate the impact of THz vibrations in the excited state system.

In addition to revealing the underlying structural mechanisms guiding charge transport, it is important to explore avenues towards protecting hybrid perovskites from the numerous instabilities which impede current application development.

While several different approaches have gained traction in enhancing perovskite stability, passivation of the surface by two-dimensional perovskite materials is among the most promising. Recently, for example, there was a demonstration of 30% improved photoconversion efficiencies in 3D perovskites passivated by 2D Dion-Jacobsen phase perovskite when tested over 1000 hours.[14] Rigorously investigating both 3D and 2D perovskites will be crucial towards their future implementation in optoelectronic technologies.

3.3 Two-dimensional Hybrid Perovskites

Layered, or 2D hybrid perovskite are composed of alternating hybrid perovskite planes and organic ligand layers (Figure 3.2). These materials are typically classified by the inorganic octahedra thickness of the perovskite layer (n number), and, like their 3D counterparts, 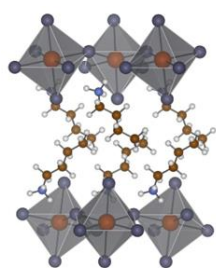command widely tunable physical properties tied to their elemental composition and ligand choice.[8,15-17] A further classification is the phase of the 2D perovskite, which can either be Ruddlesden-Popper (RP), Dion-Jacobsen (DJ), or Alternating Cation in the Interlayer (ACI).[8] The most studied phases for optoelectronics are the RP and DJ phases. The RP phase is

Figure 2.2. Butylammonium lead iodide (BA$_2$PbI$_4$) perovskite.

formed from two identical monoammonium ligands that bind ionically at the perovskite interface and through weak covalent interactions between themselves. The DJ phase is formed from one diammonium ligand which instead binds only to the perovskite interfaces on both sides of the ligand.[14] The DJ phase perovskites demonstrate higher charge conduction properties than the RP phase systems but are still largely underexplored in the literature. We will focus on the RP phase perovskites in this work due to their wide relevance in perovskite photophysics studies.[17]

Charge carrier phonon coupling is substantial enough in 2D perovskites to actively drive lattice-bound excitons, or exciton polarons, which dominate their ultrafast relaxation properties.[18] Research over the past few years has revealed that not only do the ligand molecules strongly influence the nature of the carrier-phonon coupling, but also that both the inorganic and organic THz energy vibrations play a role in photoexcited carrier dynamics. For example, while ~2 THz energy resonances appear in optical pump – probe experiments analyzing electronic state transitions, temperature resolved photoluminescence measurements show a stronger influence from ~4 THz organic ligand modes in guiding trap states responsible for white light generation.[15,18-19] Direct access to this critical energy range has been predominantly limited to Raman investigations, where indirect scattering is the only path for phonon excitation. Therefore, THz time-domain spectroscopy is a well-suited and complementary tool for fully interrogating the lattice dynamics which reportedly dictate excited state behavior.[19] Beyond this initial characterization, it will be vital to

understand how the intrinsic 2D perovskite structure is itself impacted by the ligand choice. Though some preliminary THz studies in 2D perovskites have laid an important groundwork, there remain many unanswered questions in understanding the explicit behavior of the inorganic and organic lattice.[20-21] Subsequently, we aimed to capture the ligand dependent vibrational properties of representative 2D perovskites by THz transmission spectroscopy. To proceed, we required high quality samples with well aligned layers for the most accurate analysis.

3.4 Optimized Thin Film Synthesis from Spin Coating

3D and 2D Hybrid perovskites can be synthesized from multiple approaches with varying advantages and disadvantages. Single crystal growth techniques can yield relatively large area (>1 cm) samples with high phase purity, layer alignment, and large thickness (>0.5 cm) (Figure 3.3). Inverse cooling methods are most often employed for single crystal, however, which require very stable and slow drops in temperature (1°C/hour) over many days.[22] Further, significant solvent and/or reaction

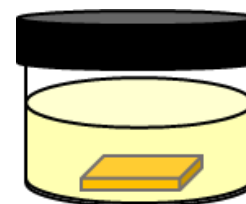**Figure 3.3. Perovskite Single crystal growth.**

engineering is required to direct the crystal growth axis with high degrees of control. That is because the self-assembling process in the formation of crystal growth thermodynamically favors specific orientations of the perovskite planes, especially in layered perovskites.[8]
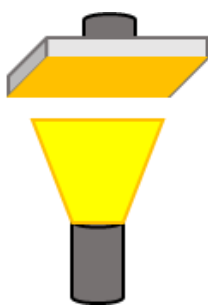
Figure 3.4. Perovskite thermal evaporation.

A developing route of synthesizing perovskites is through thermal evaporation, where perovskite precursor components are evaporated onto a substrate in a vacuum chamber and then annealed (Figure 3.4).[23] The advantages of this method are the finer controls over unform thickness on large area substrates, which is more difficult with solution-based processing. Thermal evaporation is also easily integrable with industry processes, can yield thin films with generally less pinholes, and can adjust the film formation rate.[23] While there has been recent success in generating 24% efficient 3D perovskite solar cells from thermal evaporation, the general quality of optoelectronic devices like LEDs is not yet competitive with other techniques.[24] Additionally, thermal evaporation requires longer synthesis times than solution processing and has issues with impurities contaminating deposition.

On academic laboratory scales, solution-based deposition methods like spin coating provide a rapid way of fabricating relatively large (>1 cm) films with tunable thickness and good reproducibility. In one step spin coating, the powdered perovskite precursors are dissolved into the same solvent and deposited onto the substrate at one time before annealing the sample (Figure 3.5). There are also two step spin coating methods where the perovskite precursors are individually prepared and then deposited onto the substrate sequentially. One step spin coating methods have generally shown more success in producing higher stability, higher uniformity perovskite films. The drawbacks of spin coating include difficulty integrating with
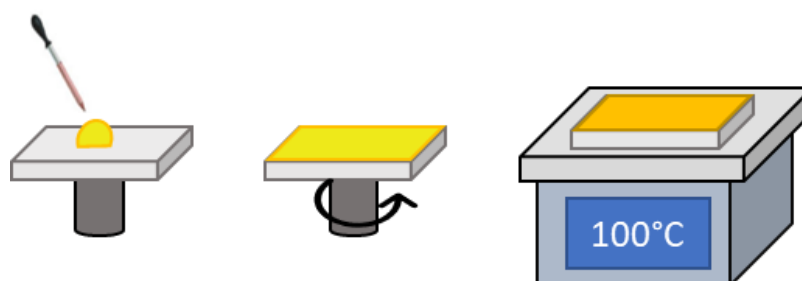
Figure 3.5. One step perovskite spin coating and annealing.

industrialization and less uniform thickness over the entire substrate area, especially for larger substrates. Another significant consideration in spin coating is the influence of nearly every variable in the synthetic process, such as the cleanliness of the substrate, solvent chemistry, spin coating parameters, annealing conditions, relative atmospheric conditions, contamination in the precursors, exposure to light, and so on.[23] Despite these disadvantages, we chose to pursue spin coating for fabrication of perovskite films due to the accessibility of necessary equipment, speed and tunability of fabrication, as well as potential reliability of perovskite quality over multiple depositions.

While the chosen materials for our study are among the most intensively researched hybrid perovskite systems, there is not yet a commonly accepted best practice spin coating procedure. Instead, much effort has been placed into learning how to manipulate the synthetic pathways to change layer alignment, phase purity (only one n-layer throughout), and to mitigate certain defects.[8] In n = 1 2D and 3D hybrid perovskite, phase purity comes along for free, as there are no competing precursors formed in solution. Phase purity for higher layer 2D n > 1 perovskites, however, is

more challenging. Further, layer alignment in n = 1 perovskite films is preferentially

parallel to the substrate, in contrast with the n = 4 2D system whose layer alignment

favors the direction perpendicular to the substrate. Despite these constraints in n = 1

perovskite synthesis, the influence of the fabrication procedure variables can still

drastically influence the quality of the resulting films. For instance, it is possible to

produce higher percentages of randomly aligned grains which simultaneously

impacts surface quality, charge conduction, and stability towards high humidity. As

there are few studies in the literature which systematically interrogate ideal spin

coating conditions for these very popular hybrid perovskites, it became necessary to

screen multiple fabrication procedures and determine the best one. We were

specifically interested in understanding the impact of 2D perovskite composition on

the most reliable routine for high quality thin films, as well as the possibilities of

uniformly rotating the layer alignment.

To start, we chose 3 solvent and 4 spin coating conditions which were notably used

in the literature to either improve film quality or to enhance preferential layer

alignment.[8] For context on the general synthetic process, stoichiometric amounts of

perovskite precursors are dissolved into a solvent and then left overnight to stir at

70°C. Substrates are cleaned via 10 min separate sonifications with isopropyl alcohol

and acetone before a minimum 10 min ozone plasma cleaning. Precursor solutions

are deposited onto substrates, the perovskites are spun at 6000 rpm for 20 seconds,

and then they are annealed at 100°C for 10 min. For the screening process, we chose

neat DMF (dimethylformamide), a DMF:DMSO (dimethylsulfoxide) mixture (3:7),

and neat gamma-Butyro lactone (GBL) as three test solvents. For spin coating procedures, we chose anti-solvent, slow crystallization, hot casting, and room temperature "normal" spin coating conditions. The addition of DMSO to DMF was chosen for reports on improving thin film crystallinity, while GBL solvent was demonstrated to facilitate single crystal formation and larger grain sizes. The anti-solvent spin coating technique developed out of 3D perovskite thin film optimizations. In this procedure, the perovskite is prepared as normal until, during the active spin cycle, a solvent in which the perovskite is immiscible is deposited onto the pre-annealed film to promote early crystallization of the perovskite. Indeed, this method shows consistent success in 3D perovskite films. The slow crystallization method was reported to facilitate 2D perovskite layers aligning perpendicular to the substrate, although the most significant impact was seen in the higher dimensional perovskite films. This synthetic procedure involves letting the perovskite film sit longer on the spin coater after the cycle for some undisclosed amount of time before annealing the film as usual. We chose ~150 seconds for this step. We mixed all solvents with all spin coating procedures to produce 18 total variations of each 2D perovskite system (36 samples in total). All thin films were deposited on sapphire wafers cleaned and processed the same way. Moreover, the thin film made from DMF solvent at room temp. spin coating conditions represented a control sample, due to the popularity of this routine in the literature at the time.

Figure 3.6 shows pictures of the resulting screening, where we can immediately observe differences in surface wetting between the variations. As a note, the color
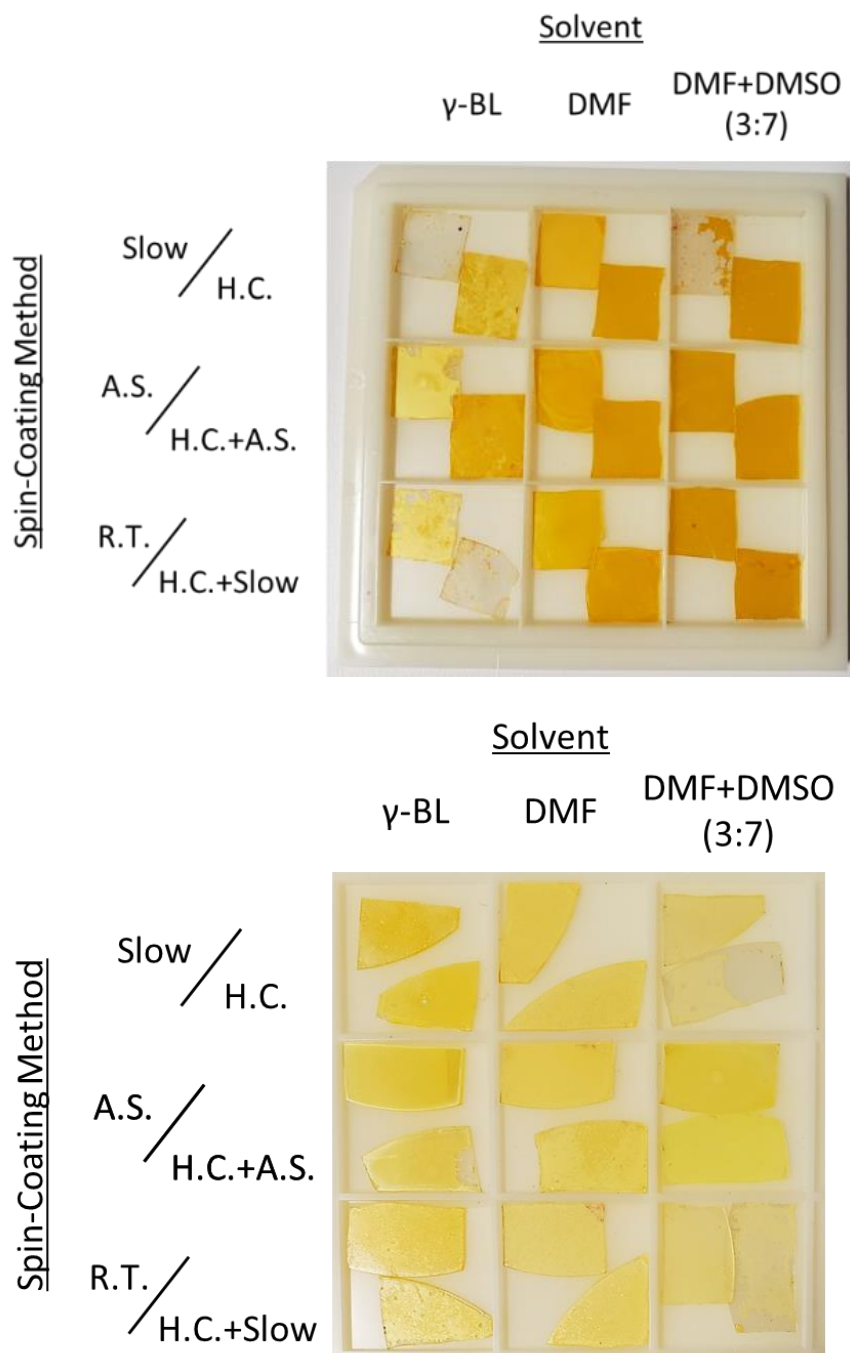
Figure 3.6. Image showing BA_2PbI_4 (top) and PEA_2PbI_4 (bottom) perovskite thin films on sapphire substrates resulting from screened synthetic conditions.

gradient shown in the thin film images are an effect of room light hitting the samples at an angle. Interestingly, we can observe by eye that the film coverage and morphologies appear different between the two perovskite compositions. To characterize the film quality more rigorously, however, we employed x-ray diffraction (XRD) and UV-Visible (UV-Vis) transmission experiments. Figure 3.7 shows representative characterization data from UV-Vis that reveals distinct exciton peaks and sharp, regularly space peaks from XRD (discussed further below). These x-ray features result from the intrinsically layered architectures of these 2D perovskites, and they also facilitate a means to cross compare all the synthetic variations. For instance, we performed a generalized peak analysis across the samples by taking the relative peak amplitudes and linewidths of the exciton peak and first x-
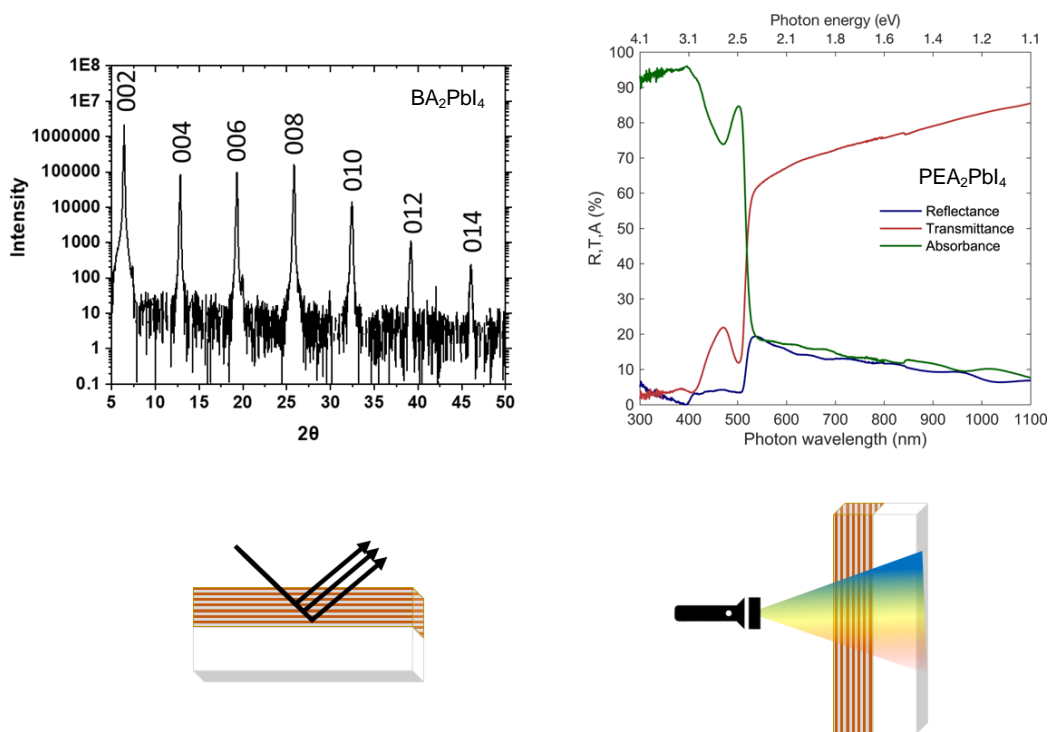

Figure 3.7. The X-ray diffraction spectrum of BA$_2$PbI$_4$ (left) and UV-Visible absorption spectrum of PEA$_2$PbI$_4$ (right) thin films made at 1 molar concentration.

ray diffraction peak. These features are correlated to the crystalline quality of the films through the ability to either support strong and long-lived excitons or possess high layer uniformity and smoothness for strong XRD peaks. It follows that stronger, narrow characteristic peaks would represent more pronounced film quality.

Figure 3.8 shows the results comparing peak amplitudes for both perovskite systems. In looking over all the samples, we identified candidate spin coating methods for best quality thin films. Intriguingly, however, the seemingly optimal procedures were not matched for both perovskite compositions. Nevertheless, we chose the candidate methods to proceed forward and through further tuning of additional fabrication variables (substrate cleaning, precursor preparation, etc.) we were able to recover extremely well aligned and high quality thin films. Figure 3.8 also shows the results of spin coating large area (2×2 cm) silicon wafers with the individually optimized 2D perovskite thin films. Excitingly, in the lab we observe uniform specular reflection off both samples across the entire area of the wafer.

We also observe intensely strong grouping of XRD peaks without a significant contribution from any irregular peaks (shown at the end of this section). These results suggest that the dominant alignment of layers is parallel to the substrate across the randomly distributed polycrystalline domains. Along with the strong exciton peaks observed in the UV-Visible spectrum, it appears we have found optimized spin coating routines which are perovskite composition dependent. Although the influence of the organic ligand on various 2D perovskite material properties is
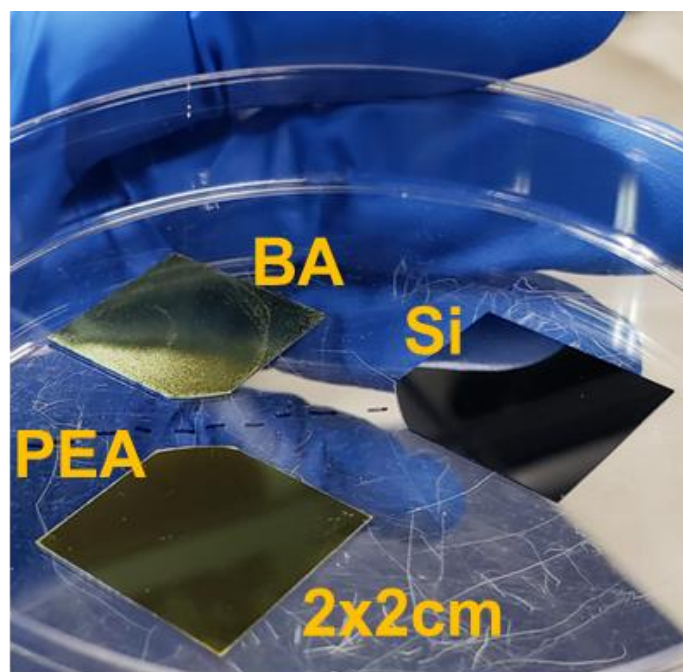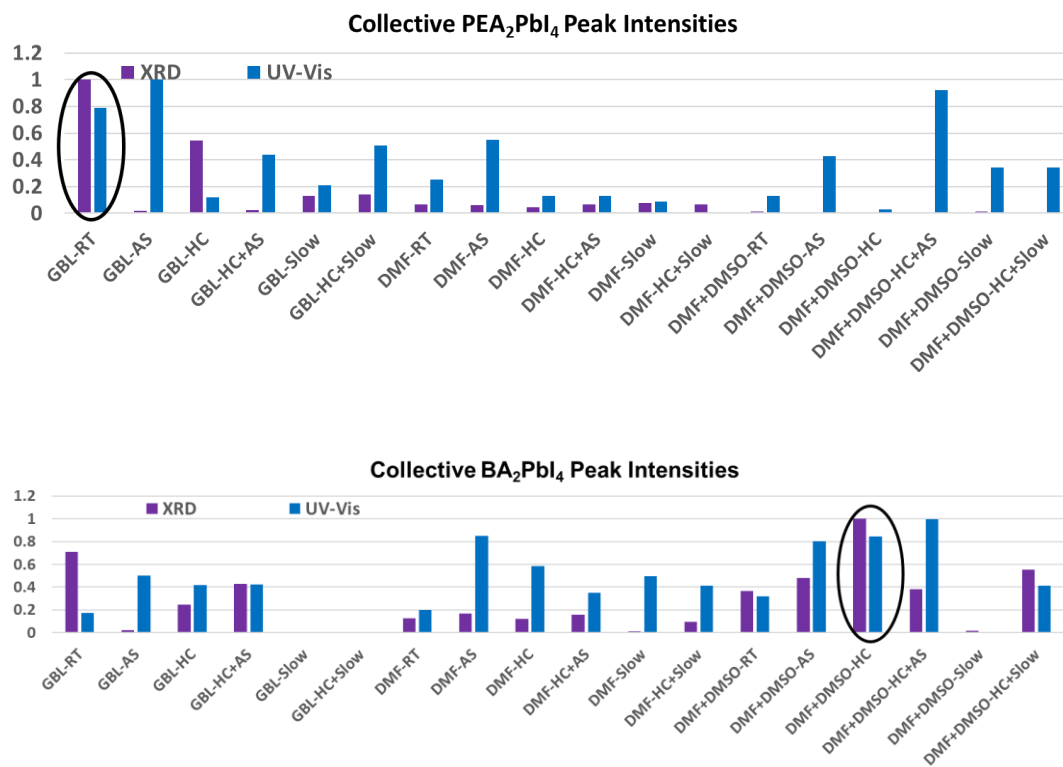
Collective PEA₂PbI₄ Peak Intensities

Collective BA₂PbI₄ Peak Intensities

Figure 3.8. Peak intensities from synthetic screening characterization (top), and large area perovskite thin films with specular reflection (bottom).
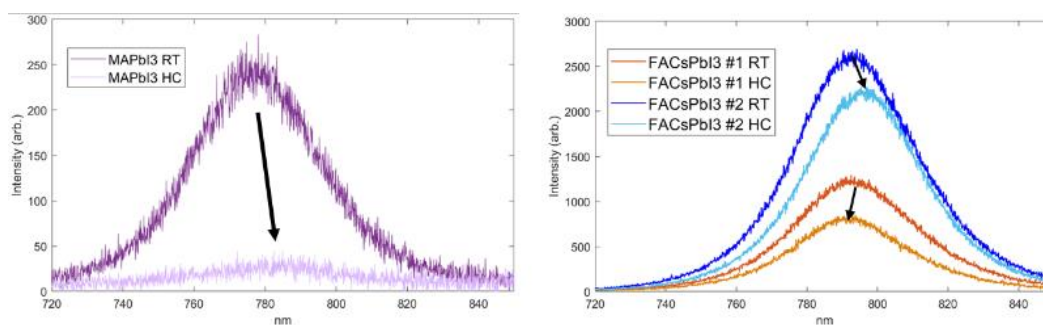
Figure 3.9. Photoluminescence spectra of room temp. and hot cast 3D perovskites MAPbI$_3$ and formamidinium (85%) cesium (15%) lead iodide (FACsPbI$_3$).

commonly known, the impact of ligand on material fabrication has yet to be reported. Furthermore, the generalized peak analysis provided a successful path towards identifying the conditions for reliably producing high quality large area thin films.

Spin coating methodology in the 3D system was less explored in our work, but early tests were run to identify better synthetic conditions. For instance, the hot casting method was compared with room temperature spin coating deposition for MAPbI$_3$ and FACsPbI$_3$ thin films (Figure 3.9). Despite having some success in the literature, our set of fabrication variables appeared to negatively react with the hot casting method, as shown by the decreased photoluminescence spectra. However, this decreased photoluminescence could be caused by numerous differences (from literature) throughout the synthetic process, such as how the substrates are specifically cleaned, the atmospheric conditions of the annealing environment, and many other influences.
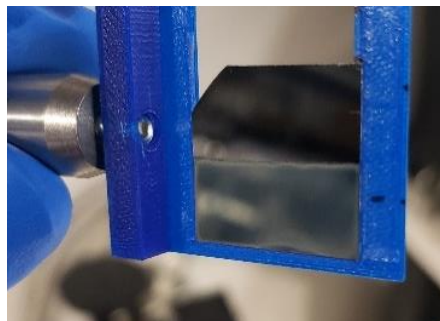

Figure 3.10. MAPbI$_3$ thin film on silicon with specular reflection.

Continuing with optimization of room temperature methods, we were ultimately able to produce specularly reflecting thin films of these 3D perovskites as well (Figure 3.10). We now detail synthetic procedures for the thin film 2D perovskites used in this work.

Synthetic procedure of n = 1 phenethylammonium lead iodide (PEA_2PbI_4) thin films: A 2 M precursor solution was first prepared in a nitrogen glovebox by dissolving 2.766 g of lead iodide and 2.988 g of phenethylammonium iodide in 3 mL of gamma-butyrolactone. This solution was stirred overnight at 80°C before being filtered through a 0.2 µm polytetrafluoroethylene syringe filter to remove any remaining particulates. Immediately prior to spincoating, high tensile strength, 200 nm thick silicon nitride windows (Norcada, part # QX10500DS) were cleaned in an ozone chamber for 12 min before transferring into the glovebox. The substrate was fully covered by precursor solution and spun at 6000 rpm for 20 seconds before annealing at 100°C for 10 min. The resulting ~950 nm thick films were characterized by a Rigaku SmartLab x-ray diffractometer, a Cary 5000 UV-Visible-NIR spectrometer, and an Ambios XP2 profilometer.

Synthetic procedure of n = 1 butylammonium lead iodide (BA_2PbI_4) thin films: A similar process as that used for PEA_2PbI_4, was followed, except the 2 M precursor solution was made by dissolving 2.766 g of lead iodide and 2.418 g of butylammonium iodide into 3 mL of a solvent mix from (3:7) N,N-dimethylformamide and dimethylsulfoxide. After transferal into the glovebox, the

cleaned substrate was preheated for 1 hour at 100°C before depositing the perovskite solution, spinning at 6000 rpm for 20 seconds and annealing at 100°C for 10 min. The resulting films were ~1.2 µm thick and characterized in the same fashion as for PEA$_2$PbI$_4$.

It is important to note that, when using substrates like sapphire or silicon wafers with >100 µm thicknesses, the cleaning process begins with >10 min each sonication baths in acetone then isopropyl alcohol. Additionally, to change the thickness of the perovskite film, we simply altered the precursor stock concentration.

Lastly, and most encouragingly, the 2M thin film X-ray and UV-Visible characterization data (Figures 3.11 and 3.12) show that crystalline quality is
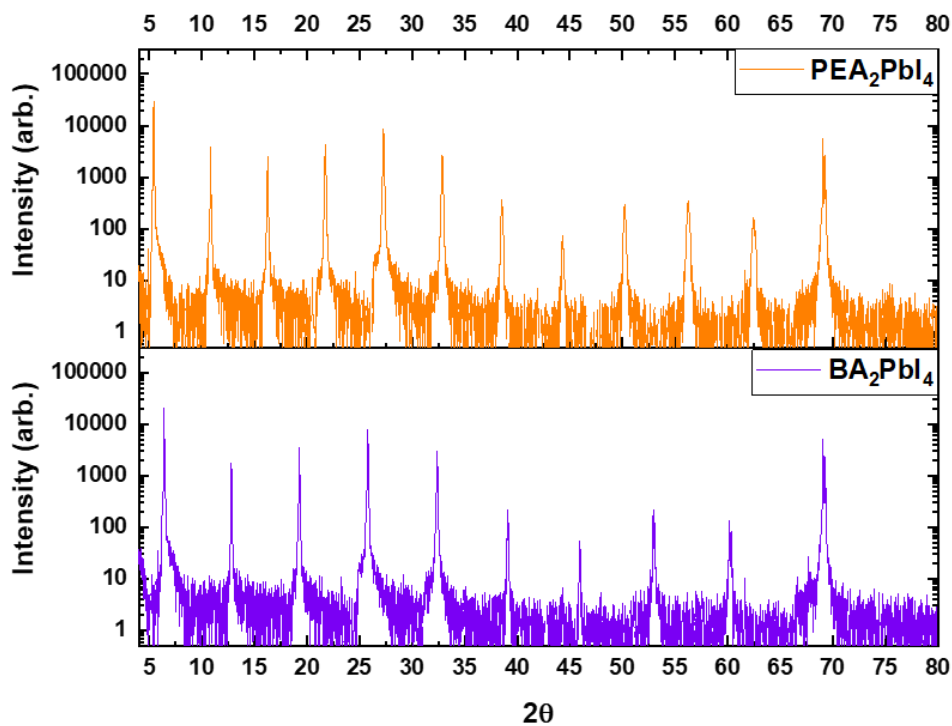

Figure 3.11. Thin film 2D perovskite X-ray diffraction from a 2M stock solution.
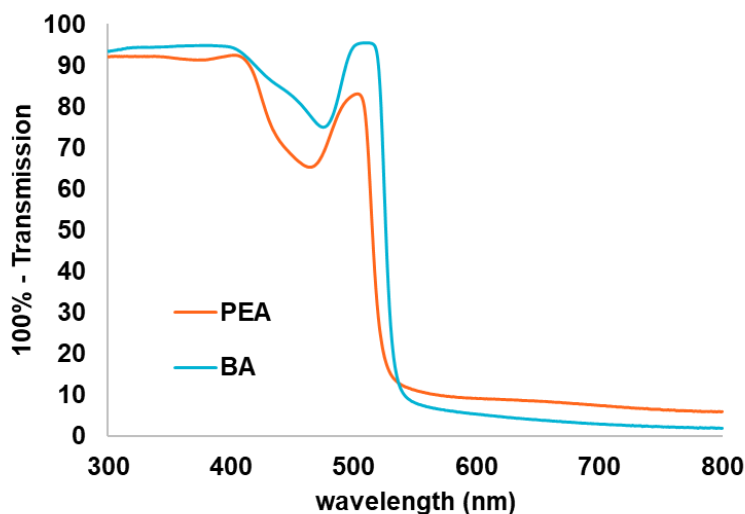
Figure 3.12. Thin film 2D perovskite UV-Visible transmission from 2M stock solution.

maintained at higher thicknesses after employing the previously optimized spin coating methods.

3.5 Enhanced THz Detection in Perovskite Coated Si_3N_4 Thin Films

3.5.1 Substrate Induced Phase Error

To accurately extract material parameters in THz-TDS, it is critical to have good knowledge of the sample thickness. With thin films supported on thick substrates, it can be equally important to know the thickness difference between the substrate used as reference and the substrate holding the sample. For most THz transparent substrates, with typical thicknesses around 100 µm to 1 mm, the fabrication process leaves a thickness tolerance quoted as high as 10%. This means that when using a

Thick Substrate

Position 1   Position 2

$\updownarrow t_1$ $\updownarrow t_2$

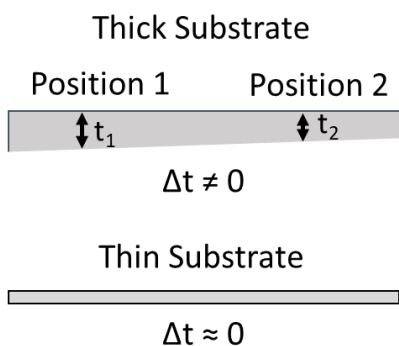$\Delta t \neq 0$

Thin Substrate

$\Delta t \approx 0$

Figure 3.13. Depiction of wedge-shaped thickness in optically thick substrate compared to optically thin substrates.

reference and sample substrate from different parent wafers, the transfer function must account for the difference in substrate thickness as accurately as possible. For thin films with high refractive index, like those expected for perovskite, error in the substrate thickness on the order of 1 micron can lead to a large uncertainty in the extracted material parameters. An additional consideration is that all wafers are only produced to a mechanically tolerated degree of flatness, meaning that each substrate wafer in our study possesses an intrinsic wedge shape (Figure 3.13). For sufficiently large areas of thin films and correspondingly large wedge angles, the thickness difference across the substrate area can become variable in micron scales, which further adds to complications in the data extraction. After trying to accommodate this error in "standard" thickness substrates like sapphire and high resistivity silicon, we decided to seek out thinner substrates. We specifically looked for solutions where the relative thickness difference, both across the substrate and between substrates, would be orders of magnitude lower than for the previous ~250 – 350 µm thick substates. We found that high tensile strength silicon nitride (Si_3N_4) was an ideal material for this purpose.

3.5.2 Enhanced THz Detection in PVSK coated Si_3N_4

We implemented high tensile strength (1 GPa) 5×5 mm silicon nitride substrates from Norcada (part # QX10500DS) that had thicknesses around 200 nm. These are

amorphous materials with very low dispersion ($\kappa \approx 0$) in our THz range and a relatively high real refractive index, measured at $n \approx 3.6$. This real index value is likely influenced by the high tensile strength fabrication, as low stress grown Si_3N_4 shows a real refractive index of $n \approx 2.3$. Because these new Si_3N_4 substrates were so thin and effectively non-absorbing, we were able to capture "substrate free" measurements of our perovskite samples while also observing enhancement of the detected THz signal. Figure 3.14 shows the normal incidence THz transmission spectra for our MA, BA, and PEA perovskite thin films being uniformly lower on Si_3N_4 substrates when compared to the spectra on undoped silicon wafer. This decreased transmission trend was consistent across

Figure 3.14. Uniform decrease in transmission from using 200 nm silicon nitride substrates instead of ~280 um undoped silicon.

numerous perovskite spin coating depositions where thin film variation ranged +/- 100 nm. The change in transmission could be due to a constructive multilayer thin film interference effect from reflections off the perovskite/Si_3N_4 and Si_3N_4/air interfaces. Another possibility is enhanced absorption in the perovskite layer from the THz pulse being more strongly reflected off the Si_3N_4 interfaces back into the
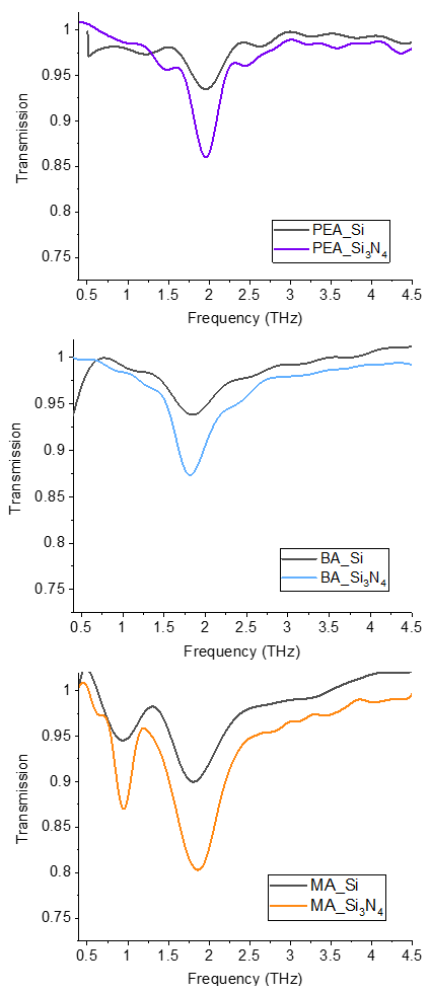
perovskite thin film. Because the Si_3N_4 refractive index is only slightly higher than for silicon ($n \approx 3.4$) or sapphire ($n \approx 3.08$), however, it seems more likely that constructive interference is responsible for the enhanced detection effect and not the intrinsic Si_3N_4 material properties alone. While more thorough testing is required to gain solid conclusions, we proceeded with confidence after successfully measuring the same perovskite refractive indices regardless of chosen substrate.

The material parameter extraction is aided not only by the additional signal-to-noise from the Si_3N_4 substrates, but also by the minimal thickness variation across the silicon nitride window. For instance, to further optimize the measurement, we synthesized thicker, ~1 µm 2D perovskite films using a 2M solution instead of the previous 1M. The extra perovskite thickness expectedly increases signal amplitude while simultaneously putting the thickness error of the substrate wedge (<10 nm) at or below the thickness error of the perovskite sample. These advantages represent significant advances in the THz TDS field, as the benefits of thin film, lossless substrates for THz transmission have not been thoroughly explored in the literature. Furthermore, the increased refractive index of Si_3N_4 under strain is an active research area, and our results provide relevant data for their behavior in the far-infrared.

3.6 Analyzing In-Plane Perovskite THz Dynamics

3.6.1 Normal Incidence MAPbI$_3$ Control

Now that we have discussed measurement optimization to yield highly sensitive THz data, we can begin exploring measurement results. Figure 3.15 shows the room temperature transmission amplitude spectra of methylammonium lead iodide on a sapphire substrate, superimposed with spectra captured from other THz studies. We observe characteristic phonon modes around 1 and 2 THz which represent the previously mentioned rocking and bending excitations of the inorganic octahedral lattice. Moreover, our spectrometer can detect much higher frequencies than the
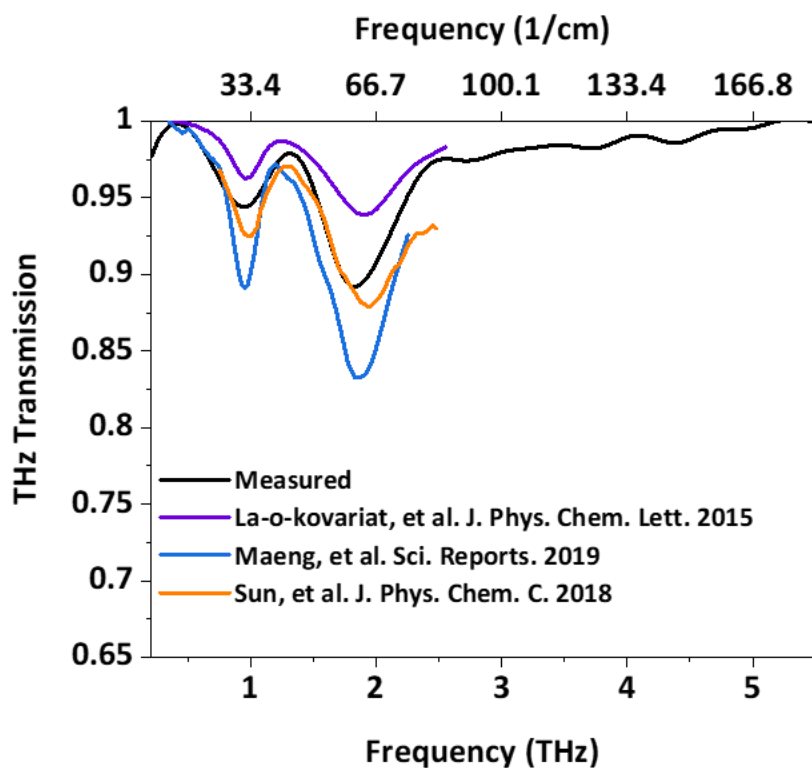

Figure 3.15. Terahertz transmission data on MAPbI$_3$ adapted from noted sources and compared with our data.

generally available THz literature for MAPbI$_3$, although this material is well characterized by Fourier transform infrared spectroscopy and other methods. In contrast to the upcoming 2D perovskite spectra, we see practically no THz resonances after the inorganic phonons up through ~5 THz, where transmission of this ~350 nm sample becomes too weak to further interpret. This behavior is widely supported by previous studies, where the only other expected peak in MAPbI$_3$ films would originate from 4 THz longitudinal optical phonon excitation at oblique incidence. Successfully measuring the MAPbI$_3$ spectrum represents a valuable reference for the capability of our spectrometer and for our perovskite synthesis techniques.

3.6.2 Normal Incidence Layered Perovskite Spectra

The next part of the discussion is adapted from a recently prepared manuscript for journal submission. All spectra in this section result from phenethylammonium and butylammonium lead iodide perovskite samples mounted at normal incidence to THz radiation within an inert nitrogen atmosphere under ambient pressure and temperature conditions. In this configuration, the THz electric field is only sensitive to interactions polarized parallel to the perovskite layers and therefore we selectively interrogate in-plane lattice dynamics (Figure 3.16). As studies
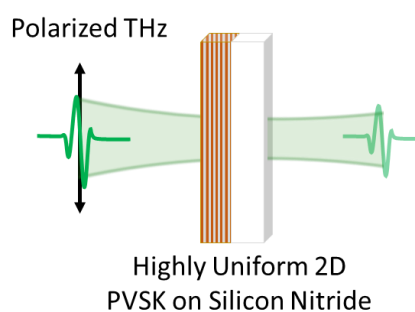
Figure 3.16. Alignment of THz electric field with 2D perovskite layers at normal incidence.
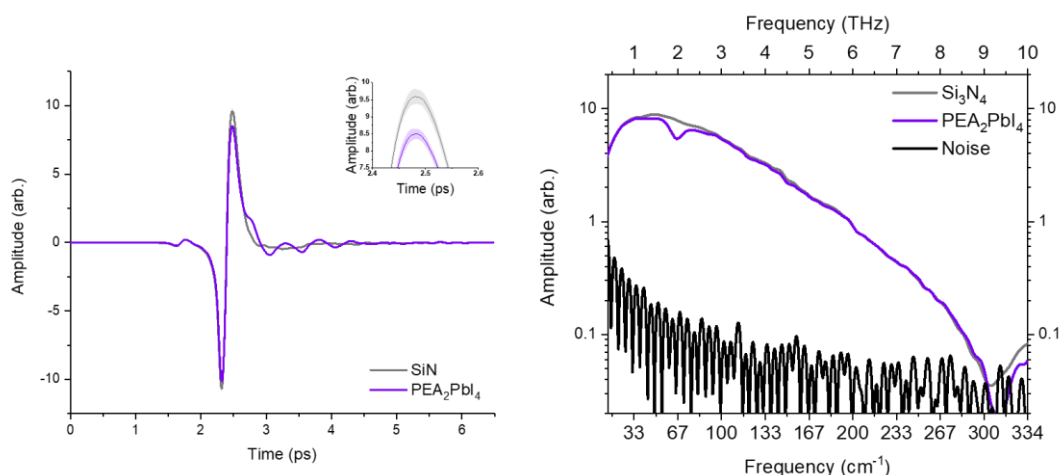
Figure 3.17. Time-domain (left) and frequency-domain (right) spectra of bare silicon nitride thin film substrate (200 nm) and spin coated phenethylammonium lead iodide (PEA$_2$PbI$_4$, ~950 nm) perovskite sample.

investigating electron/exciton - phonon coupling often probe charge transport propagating parallel to the perovskite plane, these in-plane results are highly relevant. Figure 3.17 shows the time-domain and frequency-domain amplitude spectra for the bare silicon nitride substrate and ~1 µm thin PEA$_2$PbI$_4$ deposited onto silicon nitride. Our spintronic THz emitter provides single cycle pulses that allow us to nicely resolve oscillations in the sample time-domain spectra which simultaneously indicate sharp phonon resonances in the frequency-domain. After significant optimization to the measurement setup from development on the spectrometer and sample synthesis, we also obtain low standard deviation in our time-domain scans (Figure 3.17 inset). This signal-to-noise is crucial for extracting meaningful optical parameter information from these thin film samples. The normal incidence amplitude and phase transmission spectra from both thin film perovskites are depicted in Figure 3.18a. Both these spectra are particularly significant, because they provide unambiguous visualization of infrared vibrations typically associated with excited-state coupling in
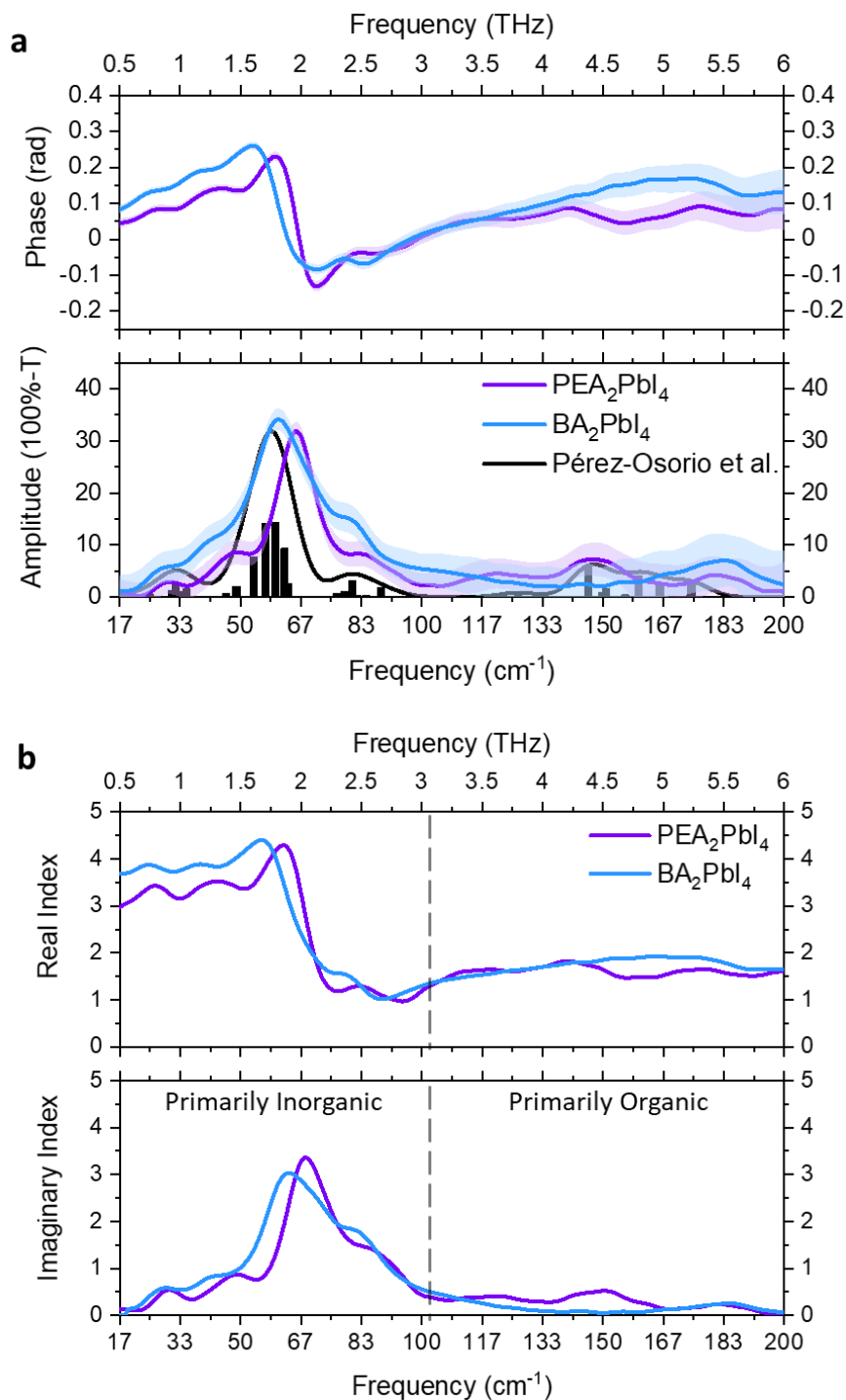
Figure 3.18. Normal incidence THz transmission (a) and refractive index values (b) for n = 1 layered perovskite thin films.

these 2D perovskites.[15,25] We find a rich collection of THz resonances that are notably influenced by the chosen organic ligands. Relative to the PEA_2PbI_4 spectrum, for instance, the observed BA_2PbI_4 peak broadening could result from stronger phonon scattering off the more distorted inorganic BA_2PbI_4 lattice.[26] This effect, induced by the flexible alkyl ligand chains, is consistent with literature findings comparing these systems.[8,26] The complex refractive index polarized parallel to the perovskite plane is shown in Figure 3.18b. We observe similar trends in material parameters for these 2D perovskites, having relatively larger values at lower THz frequencies which decrease at higher energies.

To deepen our interpretation of the experimental spectra, we draw insight from previously published density functional perturbation theory (DFPT) calculations on hybrid perovskites. The 2015 study by Pérez-Osorio et al. offers a thorough analysis of a calculated infrared spectrum for the prototypical methylammonium lead iodide ($MAPbI_3$) bulk hybrid perovskite which proves relevant to our work.[27] Despite originating from a three-dimensional perovskite structure, we observe remarkable similarities between their DFPT calculated THz spectrum and our own data (Figure 3.18a). For instance, all spectra exhibit a central peak accompanied by at least two side bands before collectively decreasing in activity near ~110 cm^{-1} (3.3 THz) and subsequently displaying smaller amplitude excitations above ~110 cm^{-1}. Given this overlap of spectral features, we prioritize the infrared mode assignments from Pérez-Osorio et al. to elucidate the origin of our characteristic peaks. Specifically, the pronounced phonons below 110 cm^{-1} reportedly comprise a multitude of bending,

rocking, and stretching modes from the lead iodide octahedral network, while excitations above ~110 cm^{-1} are predominantly attributed to collective organic ligand motions. These general spectral classifications are well-supported by both 2D perovskite Raman and photoexcited pump – probe studies.[17-19] Characterizing our experimental spectra in this framework implies that we detect "bulk-like" lead-iodide modes confined to one inorganic octahedra thickness (n = 1) which are derived from dimensionally unconstrained MAPbI$_3$ (n = ∞). Phonon mode confinement is a common property of superlattice structures and evidence of its existence in n = 1 2D perovskites was recently presented by Chen et al. through DFPT calculations and Raman spectroscopy.[28] We consequently ascribe our in-plane THz spectra to excitations by "primarily inorganic" and "primarily organic" phonons which are mostly confined to their respective 2D perovskite layers, as well as energetically separated in frequency space. This qualitative mode assignment of our spectra can help explain the observed blue shift of the PEA$_2$PbI$_4$ inorganic peaks to higher THz frequencies. A relatively more rigid lead iodide lattice supported by the phenethylammonium covalent bonds would require higher energy to mechanically vibrate compared to the more flexible lattice of the BA$_2$PbI$_4$ perovskite.

The resolution and interpretation of these photodynamically coupled THz modes represents a significant advancement in our understanding of room temperature, ligand-dependent vibrational behavior in 2D perovskites. This work serves as a necessary stepping stone for future investigations into layered perovskite excited state phenomena, and further promotes the continued study of their intrinsic

structure-function relationships. For instance, we still do not have a clear understanding about how direction-dependence in the lattice would impact THz activity.

CHAPTER 3 BIBLIOGRAPHY

1. Maldonado, S. The Importance of New "Sand-to-Silicon" Processes for the Rapid Future Increase of Photovoltaics. *ACS Energy Lett.* **2020**, *5* (11), 3628–3632. https://doi.org/10.1021/acsenergylett.0c02100.

2. Powell, D. M.; Fu, R.; Horowitz, K.; Basore, P. A.; Woodhouse, M.; Buonassisi, T. The Capital Intensity of Photovoltaics Manufacturing: Barrier to Scale and Opportunity for Innovation. *Energy Environ. Sci.* **2015**, *8* (12), 3395–3408. https://doi.org/10.1039/C5EE01509J.

3. Chin, X. Y.; Turkay, D.; Steele, J. A.; Tabean, S.; Eswara, S.; Mensi, M.; Fiala, P.; Wolff, C. M.; Paracchino, A.; Artuk, K.; Jacobs, D.; Guesnay, Q.; Sahli, F.; Andreatta, G.; Boccard, M.; Jeangros, Q.; Ballif, C. Interface Passivation for 31.25%-Efficient Perovskite/Silicon Tandem Solar Cells. *Science* **2023**, *381* (6653), 59–63. https://doi.org/10.1126/science.adg0091.

4. Martin, B.; Amos, D.; Brehob, E.; van Hest, M. F. A. M.; Druffel, T. Techno-Economic Analysis of Roll-to-Roll Production of Perovskite Modules Using Radiation Thermal Processes. *Appl. Energy* **2022**, *307*, 118200. https://doi.org/10.1016/j.apenergy.2021.118200.

5. Rolston, N.; Scheideler, W. J.; Flick, A. C.; Chen, J. P.; Elmaraghi, H.; Sleugh, A.; Zhao, O.; Woodhouse, M.; Dauskardt, R. H. Rapid Open-Air Fabrication of Perovskite Solar Modules. *Joule* **2020**, *4* (12), 2675–2692. https://doi.org/10.1016/j.joule.2020.11.001.

6. Fu, J.; Ramesh, S.; Melvin Lim, J. W.; Sum, T. C. Carriers, Quasi-Particles, and Collective Excitations in Halide Perovskites. *Chem. Rev.* **2023**, *123* (13), 8154–8231. https://doi.org/10.1021/acs.chemrev.2c00843.

7. Jena, A. K.; Kulkarni, A.; Miyasaka, T. Halide Perovskite Photovoltaics: Background, Status, and Future Prospects. *Chem. Rev.* **2019**, *119* (5), 3036–3103. https://doi.org/10.1021/acs.chemrev.8b00539.

8. Li, X.; Hoffman, J. M.; Kanatzidis, M. G. The 2D Halide Perovskite Rulebook: How the Spacer Influences Everything from the Structure to Optoelectronic Device Efficiency. *Chem. Rev.* **2021**, *121* (4), 2230–2291. https://doi.org/10.1021/acs.chemrev.0c01006.

9. Kojima, A.; Teshima, K.; Shirai, Y.; Miyasaka, T. Organometal Halide Perovskites as Visible-Light Sensitizers for Photovoltaic Cells. *J. Am. Chem. Soc.* **2009**, *131* (17), 6050–6051. https://doi.org/10.1021/ja809598r.

10. Kim, J. Y.; Lee, J.-W.; Jung, H. S.; Shin, H.; Park, N.-G. High-Efficiency Perovskite Solar Cells. *Chem. Rev.* **2020**, *120* (15), 7867–7918. https://doi.org/10.1021/acs.chemrev.0c00107.

11. Huang, J.; Yuan, Y.; Shao, Y.; Yan, Y. Understanding the Physical Properties of Hybrid Perovskites for Photovoltaic Applications. *Nat. Rev. Mater.* **2017**, *2* (7), 17042. https://doi.org/10.1038/natrevmats.2017.42.

12. Mayers, M. Z.; Tan, L. Z.; Egger, D. A.; Rappe, A. M.; Reichman, D. R. How Lattice and Charge Fluctuations Control Carrier Dynamics in Halide Perovskites. *Nano Lett.* **2018**, *18* (12), 8041–8046. https://doi.org/10.1021/acs.nanolett.8b04276.

13. Jiang, Y.; Wang, X.; Pan, A. Properties of Excitons and Photogenerated Charge Carriers in Metal Halide Perovskites. *Adv. Mater.* **2019**, *31* (47). https://doi.org/10.1002/adma.201806671.

14. Zhang, F.; Park, S. Y.; Yao, C.; Lu, H.; Dunfield, S. P.; Xiao, C.; Uličná, S.; Zhao, X.; Du Hill, L.; Chen, X.; Wang, X.; Mundt, L. E.; Stone, K. H.; Schelhas, L. T.; Teeter, G.; Parkin, S.; Ratcliff, E. L.; Loo, Y.-L.; Berry, J. J.; Beard, M. C.; Yan, Y.; Larson, B. W.; Zhu, K. Metastable Dion-Jacobson 2D Structure Enables Efficient and Stable Perovskite Solar Cells. *Science* **2022**, *375* (6576), 71–76. https://doi.org/10.1126/science.abj2637.

15. Li, J.; Lu, G.; Xie, H.; Jiang, X.; Fang, Z.; Zeng, Y.-J.; He, H.; Ye, Z. Effect of Electron–Phonon Coupling on the Color Purity of Two-Dimensional Ruddlesden–Popper Hybrid Lead Iodide Perovskites. *J. Phys. Chem. C* **2023**, *127* (13), 6380–6388. https://doi.org/10.1021/acs.jpcc.2c08609.

16. Ruan, Z.; Jiang, S.; Zhang, Q.; Luo, Y. Phononic Fine-Tuning in a Prototype Two-Dimensional Hybrid Organic–Inorganic Perovskite System. *J. Phys. Chem. Lett.* **2022**, *13* (24), 5480–5487. https://doi.org/10.1021/acs.jpclett.2c01290.

17. Straus, D. B.; Kagan, C. R. Photophysics of Two-Dimensional Semiconducting Organic–Inorganic Metal-Halide Perovskites. *Annu. Rev. Phys. Chem.* **2022**, *73* (1), 403–428. https://doi.org/10.1146/annurev-physchem-082820-015402.

18. Thouin, F.; Valverde-Chávez, D. A.; Quarti, C.; Cortecchia, D.; Bargigia, I.; Beljonne, D.; Petrozza, A.; Silva, C.; Srimath Kandada, A. R. Phonon Coherences Reveal the Polaronic Character of Excitons in Two-Dimensional Lead Halide Perovskites. *Nat. Mater.* **2019**, *18* (4), 349–356. https://doi.org/10.1038/s41563-018-0262-7.

19. Mauck, C. M.; France-Lanord, A.; Hernandez Oendra, A. C.; Dahod, N. S.; Grossman, J. C.; Tisdale, W. A. Inorganic Cage Motion Dominates Excited-State Dynamics in 2D-Layered Perovskites (C x H 2 x +1 NH 3) 2 PbI 4 (x = 4–9). *J. Phys. Chem. C* **2019**, *123* (45), 27904–27916. https://doi.org/10.1021/acs.jpcc.9b07933.

20. Folpini, G.; Gatto, L.; Cortecchia, D.; Devetta, M.; Crippa, G.; Vozzi, C.; Stagira, S.; Petrozza, A.; Cinquanta, E. Ultrafast Charge Carrier Dynamics in Quantum Confined 2D Perovskite. *J. Chem. Phys.* **2020**, *152* (21). https://doi.org/10.1063/5.0008608.

21. Burgos-Caminal, A.; Socie, E.; Bouduban, M. E. F.; Moser, J.-E. Exciton and Carrier Dynamics in Two-Dimensional Perovskites. *J. Phys. Chem. Lett.* **2020**, *11* (18), 7692–7701. https://doi.org/10.1021/acs.jpclett.0c02425.

22. Wang, S.; Chen, Y.; Yao, J.; Zhao, G.; Li, L.; Zou, G. Wafer-Sized 2D Perovskite Single Crystal Thin Films for UV Photodetectors. *J. Mater. Chem. C* **2021**, *9* (20), 6498–6506. https://doi.org/10.1039/D1TC00408E.

23. Bae, S.-R.; Heo, D. Y.; Kim, S. Y. Recent Progress of Perovskite Devices Fabricated Using Thermal Evaporation Method: Perspective and Outlook. *Mater. Today Adv.* **2022**, *14*, 100232. https://doi.org/10.1016/j.mtadv.2022.100232.

24. Li, H.; Zhou, J.; Tan, L.; Li, M.; Jiang, C.; Wang, S.; Zhao, X.; Liu, Y.; Zhang, Y.; Ye, Y.; Tress, W.; Yi, C. Sequential Vacuum-Evaporated Perovskite Solar Cells with More than 24% Efficiency. *Sci. Adv.* **2022**, *8* (28). https://doi.org/10.1126/sciadv.abo7422.

25. Fu, J.; Li, M.; Solanki, A.; Xu, Q.; Lekina, Y.; Ramesh, S.; Shen, Z. X.; Sum, T. C. Electronic States Modulation by Coherent Optical Phonons in 2D Halide Perovskites. *Adv. Mater.* **2021**, *33* (11). https://doi.org/10.1002/adma.202006233.

26. Seitz, M.; Magdaleno, A. J.; Alcázar-Cano, N.; Meléndez, M.; Lubbers, T. J.; Walraven, S. W.; Pakdel, S.; Prada, E.; Delgado-Buscalioni, R.; Prins, F. Exciton Diffusion in Two-Dimensional Metal-Halide Perovskites. *Nat. Commun.* **2020**, *11* (1), 2035. https://doi.org/10.1038/s41467-020-15882-w.

27. Pérez-Osorio, M. A.; Milot, R. L.; Filip, M. R.; Patel, J. B.; Herz, L. M.; Johnston, M. B.; Giustino, F. Vibrational Properties of the Organic–Inorganic Halide Perovskite CH 3 NH 3 PbI 3 from Theory and Experiment: Factor Group Analysis, First-Principles Calculations, and Low-Temperature Infrared Spectra. *J. Phys. Chem. C* **2015**, *119* (46), 25703–25718. https://doi.org/10.1021/acs.jpcc.5b07432.

28. Chen, Y.; Mahata, A.; Lubio, A. D.; Cinquino, M.; Coriolano, A.; Skokan, L.; Jeong, Y.; Razzari, L.; De Marco, L.; Ruediger, A.; De Angelis, F.; Colella, S.; Orgiu, E. Phonon Analysis of 2D Organic-Halide Perovskites in the Low- and Mid-IR Region. *Adv. Opt. Mater.* **2022**, *10* (16). https://doi.org/10.1002/adom.202100439.

Chapter 4

UNCOVERING ENERGY-LOCALIZED THZ ANISOTROPY IN 2D PEROVSKITES

4.1 Motivation

This chapter is adapted from a recently prepared manuscript for journal submission.

The presence or absence of anisotropy, meaning direction-dependence, critically influences a material's response to stimuli. Two-dimensional (2D) hybrid perovskites possess intrinsic structural anisotropy which significantly affects their excitations across the electromagnetic spectrum.[1-4] For instance, Ruddlesden-Popper (RP) phase perovskites used for x-ray scintillators were recently reported to have anisotropic current density and x-ray sensitivity with differences of >100× in magnitude.[2] Similarly, anisotropic excitation and Raman absorption has also been observed in layered perovskite systems. Curiously, though, anisotropy studies into RP phase perovskite thermal conductivity have revealed significantly weak behavior. This distinction between anisotropy of thermally conducting phonons and electronically conducting phonons is unclear in literature. Moreover, the anisotropy of photodynamically coupled THz energy modes has not been thoroughly explored.

The terahertz (THz) range modes in hybrid perovskites comprise inorganic and organic phonon excitations which strongly couple to and modulate electronic excited-state properties, thus broadly impacting material performance.[5-15] Charge conduction in 2D perovskite devices is primarily optimized for transport parallel to

the perovskite layer, thereby avoiding enhanced carrier scattering which results from transport perpendicular to the layers. Key insights about how electron-phonon coupling influences transport in that perpendicular direction, however, could be revealed by THz frequency material parameters polarized perpendicular to the perovskite planes. Furthermore, the comparison of orthogonally polarized THz excitations could uncover important relationships in inter-phonon coupling in the highly uniform thin films produced in this thesis work. Consequently, we rigorously investigate the fundamental nature and anisotropic strength of optically active THz resonances in benchmark $n = 1$ RP phase perovskites to uncover elusive phonon properties governing the photodynamics of these materials.

4.2 Experiment Design and Development

To resolve anisotropy in our 2D perovskite thin films, we can construct experiments which incorporate either a rotation of the sample or an incidence angle change of the polarized THz light. We are limited to these two experimental options due to difficulties in synthesizing $n = 1$ RP phase perovskites with layers uniformly oriented off-parallel to the substrate (see Chapter 3.4). We chose to prioritize rotations of the sample relative to a fixed incident THz beam by implementing a custom 3D printed sample holder, as described in Chapter 2.
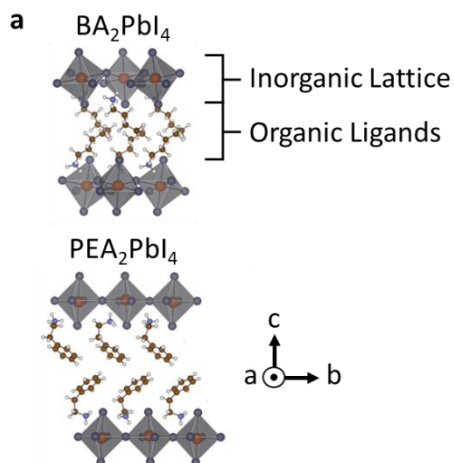
4.2.1 Benchmark Systems: n = 1 Layered Perovskites

Figure 4.1. Benchmark layered n = 1 perovskites: butylammonium lead iodide (top) and phenethylammonium lead iodide (bottom).

Organic spacers exhibiting stronger bonds, like the covalent forces between aromatic ligands, facilitate more rigidity within the perovskite structure and minimize tilting of the octahedral perovskite network.[1,8,11,13,16] Less-flexible inorganic lattices reduce charge carrier scattering and thus facilitate higher conductivity compared to layered perovskites with alkyl ligands that possess only weak Van der Waals interactions.[16] Numerous studies highlight the importance of investigating a variety of 2D perovskite compositions to comprehensively understand the whole material class.[1,6,8,15-16] In this context, we focus on the extensively studied Ruddlesden-Popper phase n = 1 butylammonium lead iodide (BA_2PbI_4) and phenethylammonium lead iodide (PEA_2PbI_4) perovskite systems (Figure 4.1).[1] These benchmark materials feature contrasting degrees of distortion imposed on their lead iodide octahedral lattice, which in turn shapes the terahertz vibrational dynamics guiding anisotropic photoexcited charge transport in layered perovskites. To directly assess the terahertz activity and potential anisotropy, we employ oblique incidence THz time-domain spectroscopy with polarization control.

We synthesized high-quality, approximately ~1 µm thin films of BA_2PbI_4 and PEA_2PbI_4 perovskite using optimized spin coating procedures and 200 nm thin silicon nitride substrates. These polycrystalline films host ~1- 10 µm diameter grains with randomly distributed in-plane crystallographic orientation, such that grains are rotated about c-axis in Figure 4.1. Importantly, x-ray diffraction confirms that these thin films also host uniformly aligned perovskite inorganic layers which are parallel to the substrate across the entire film area (see Figure 3.13 in Chapter 3). Considering that our THz spot size is ≤1.5 mm in diameter, we assume the in-plane response (a-b axis of Figure 4.1) is directionally averaged and therefore that only two unique excitation dimensions exist in our samples (e.g., in-plane and out-of-plane).

4.2.2 Polarization-Sensitive Oblique Incidence Transmission

We selectively interrogate direction-dependent material parameters in anisotropic samples by utilizing polarization and incidence angle sensitivity. In this manner, we perform transmission geometry measurements at precise angles of incidence to obtain the first measurements of out-of-plane as well as in-plane thin film 2D perovskite THz excitations.

In our experiments, the linearly polarized incident THz electric field defines a plane-of-incidence (POI), around which there are three possible rotation directions of the sample: normal incidence around the POI, oblique incidence out of the POI, and oblique incidence into the POI. The first two possible rotations maintain a

parallel alignment between the THz electric field and the perovskite layers, thereby only sensing the in-plane dynamics. The THz transmission at these sample configurations is described by an electric field with transverse electric (TE) polarization (Figure 4.2a). The third rotation direction, however, aligns the electric field somewhere between parallel and perpendicular to the layers, thereby sensing a combination of in-plane and out-of-plane dynamics. This configuration is described by an electric field with transverse magnetic (TM) polarization and the contribution of each

Figure 4.2. Rotation of thin film perovskite around the plane-of-incidence (a), and into the plane-of-incidence (b).

orthogonal material parameter is determined by the angle of incidence (Figure 4.2b). For example, the TM 45° incidence THz transmission spectra of layered perovskite would exhibit an average THz response from equal contributions of the in-plane and out-of-plane lattice dynamics.

Since in-plane material parameter extraction from TE 45° incidence transmission should be the same as from normal incidence, we use this configuration as a control to ensure accurate implementation of our angle-dependent THz analysis (see section 2.2.3 in Chapter 2). We then employ TM 45° incidence THz transmission to collect directionally averaged dynamics and back calculate the out-of-plane material parameters through the following equations. Finally, we examine their
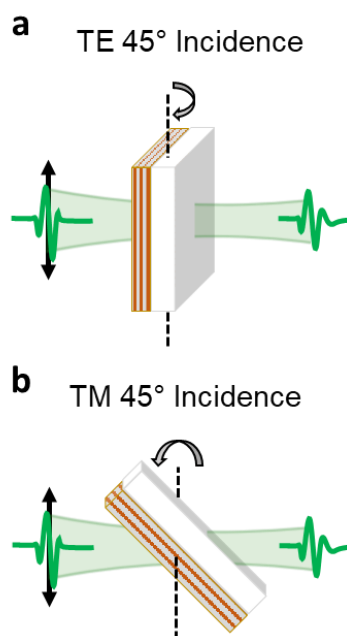
differences to obtain the broadband THz anisotropy, shown below as a birefringence.

$$\tilde{n}_{0°} = \tilde{n}_{TE_{45}°} = \tilde{n}_{in-plane}$$

$$\tilde{n}_{TM\_45°} = 0.5 \cdot \tilde{n}_{in-plane} + 0.5 \cdot \tilde{n}_{out-of-plane}$$

$$Birefringence = \Delta\tilde{n} = \tilde{n}_{in-plane} - \tilde{n}_{out-of-plane}$$

Here, $\tilde{n} = n + i \cdot \kappa$. Accuracy of these THz measurements relies on several key experimental factors. The quality of the 2D perovskite samples, uniformity of layers, and alignment of incidence angle collectively determine how well the final out-of-plane material parameters represent the system. Our high-quality thin films demonstrate consistent layer uniformity and are mounted in a custom 3D printed holder which allows for precise 45° rotation about the center.

4.3 Revealing Strong Energy-Localized Anisotropy

We start again with the MAPbI$_3$ spectra to build a solid foundation for the 2D perovskite measurements. Our ~350 nm polycrystalline thin film MAPbI$_3$ perovskite is expected to exhibit an isotropic response from oblique incidence THz transmission, as the tetragonal structure of the single crystal would be randomly distributed through the THz spot size (~1.5 mm). Figure 4.3 shows the normal incidence combined with oblique incidence transmission and refractive index

spectra measured at both TE- and TM-polarized THz waves. Encouragingly, we indeed recover consistent refractive index data for the oblique incidence measurements to within reasonable error limited by the sample thickness.

We also observe some notable differences in the TM-polarized spectra relative to the other two. Specifically, we see the rise of a THz excitation around 4 THz, which has been well-observed in the literature as belonging to a longitudinal optical (LO) phonon. This excitation is the outcome of coupling the obliquely incident electric THz field both parallel and perpendicular to the $MAPbI_3$ crystal surface.[17-18] The LO phonon is degenerate in energy with the previously observed 2 THz transverse optical (TO) phonon and their *combined* excitation leads to LO-TO splitting which shifts the LO phonon frequency to 4 THz. These results are

Figure 4.3. Extracted refractive index from oblique incidence THz transmission in methylammonium lead iodide perovskite.

corroborated by both experimentally measured IR spectra as well as density functional theory calculations by Pérez-Osorio et al.[18] Despite some signal limitations due to the 350 nm film thickness, this successful control measurement
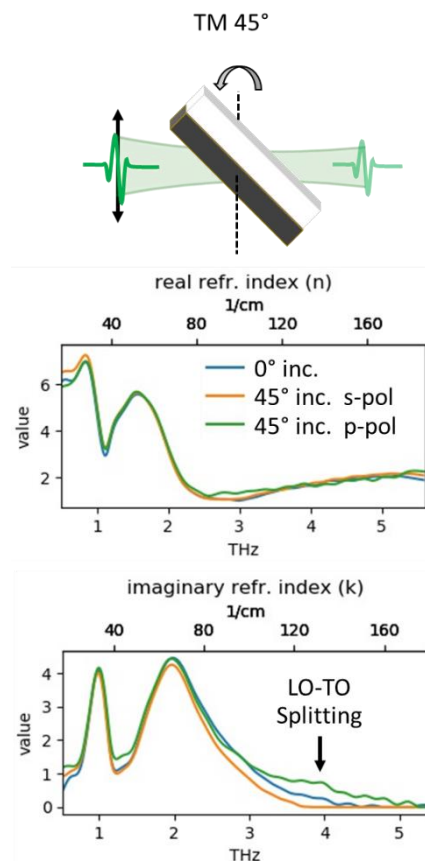
gives confidence to the 2D perovskite analysis through both the physical sample holder configuration as well as the generalized transfer function fitting.

Figure 4.4 displays the oblique incidence transmission spectra as well as the first reported out-of-plane polarized material parameters for these intensively researched n = 1 perovskite thin films. The measured amplitude and phase spectra follow well-understood trends for TE and TM interactions defined by Fresnel coefficients at oblique incidences.[19] The extracted orthogonal material parameters, however, display an interesting degree of similarity across the spectrum, with a
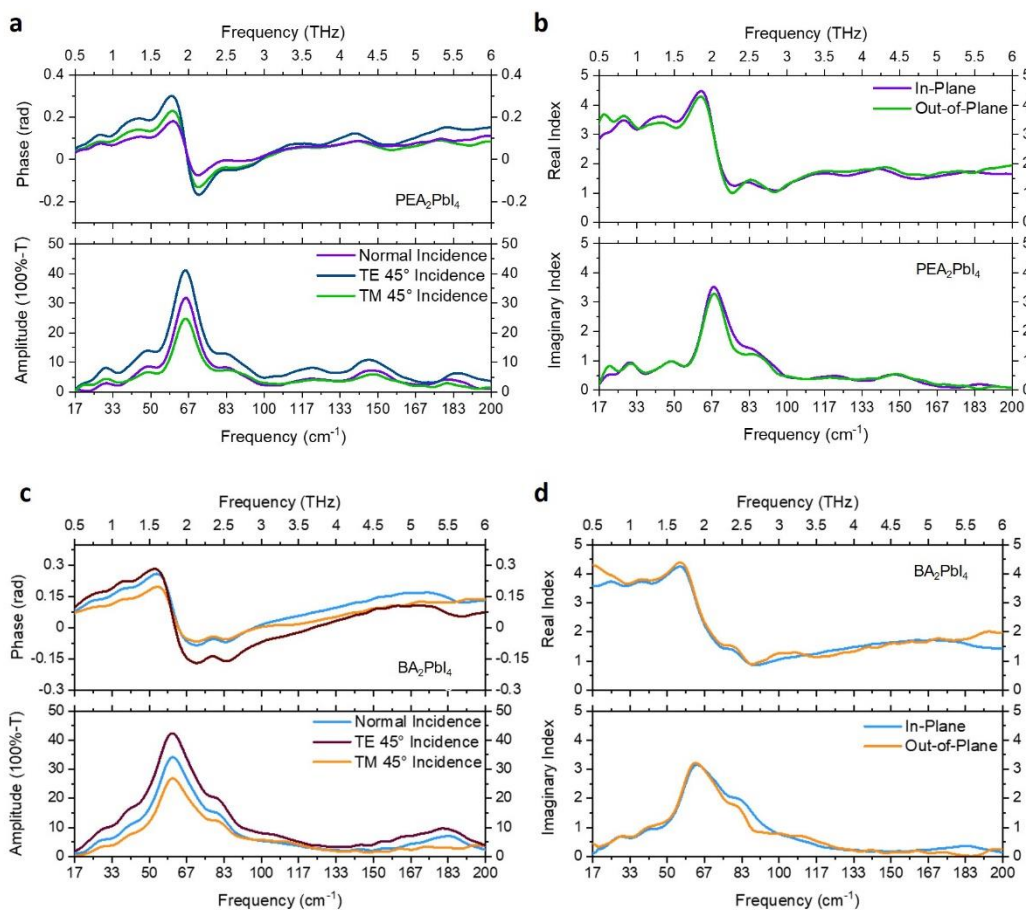

Figure 4.4. Oblique incidence THz transmission spectra and extracted refractive index for in-plane and out-of-plane directions in PEA$_2$PbI$_4$ (a,b) and BA$_2$PbI$_4$ (c,d).

notable exception around the resonances attributed to primarily inorganic lattice phonons. These findings suggest, again with notable exception, that the same vibrational modes observed in normal incidence spectra are also accessible from the out-of-plane excitation direction.

Close inspection of the visualized MAPbI$_3$ phonons from Pérez-Osorio et al. provides some insight into this behavior, as most of the THz modes host atomic displacements vibrating in orthogonal directions.[8,18,20] In our system, these orthogonal lattice motions could orient the phonon transition dipoles somewhere between parallel and perpendicular to the perovskite layers, thereby allowing for direct excitation from arbitrary incidence angles. Such ubiquitous transition dipole excitations, regardless of incident THz electric field polarization, would produce weaker optical anisotropy across the THz spectra. Based on our normal incidence characterization, these oblique incidence spectra suggest that both the primarily inorganic and primarily organic perovskite phonons possess orthogonally accessible transition dipoles.

In THz spectroscopy literature, anisotropy is reported as "strong" in samples with birefringence values $\Delta n, \Delta k \gtrsim 0.1$.[21] Due to the sensitive nature of weakly transmitting thin film THz measurements, we find $\Delta n, \Delta k \approx 0.1$ to also be our anisotropy detection threshold from the TE 45° incidence control data after accounting for the mean plus standard deviation (Figure 4.5a,b). Despite this
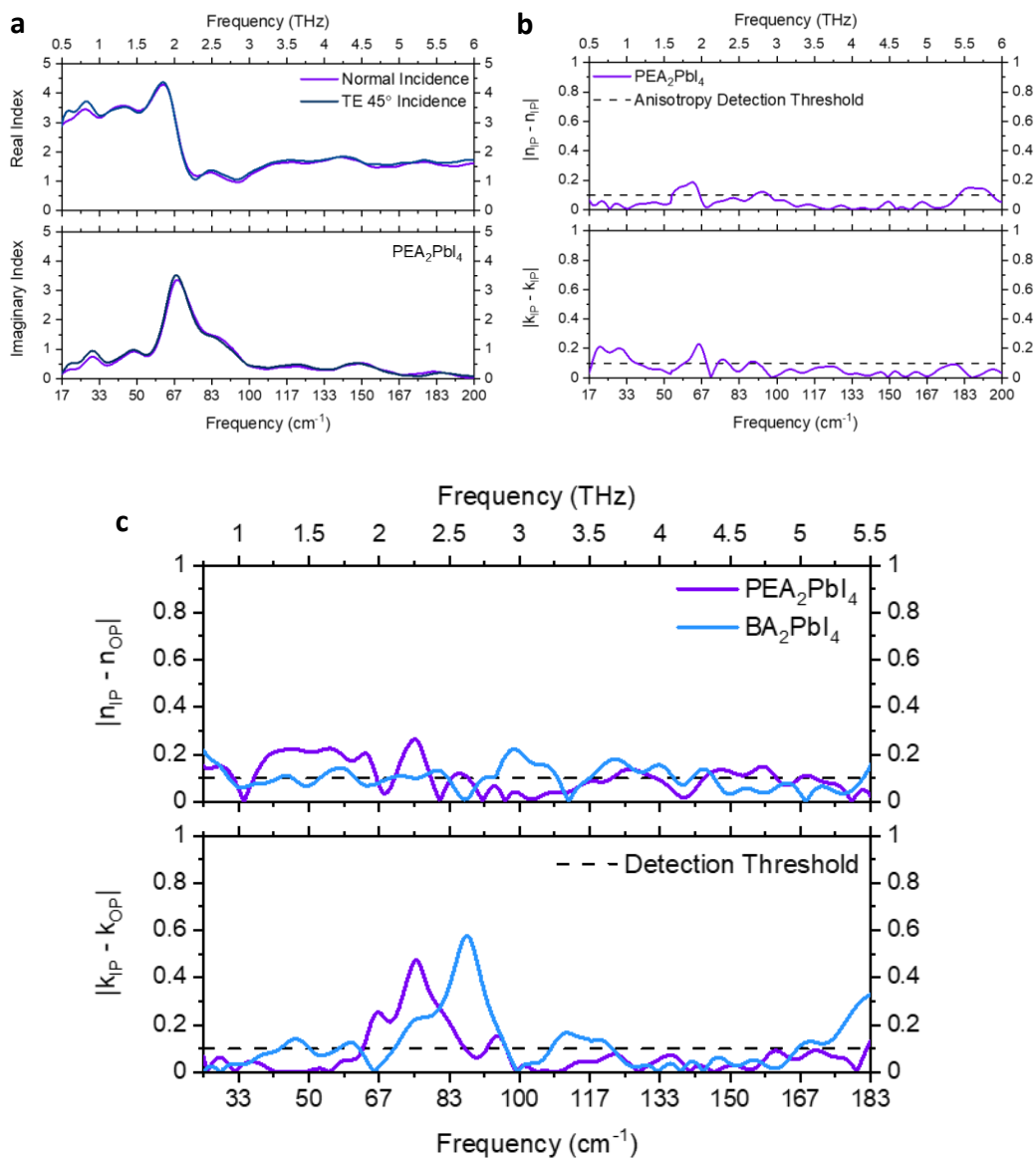
Figure 4.5. Extracted in-plane refractive index for PEA$_2$PbI$_4$ from normal and TE 45° incidence (a), leading to experimental detection limit of anisotropy (b), and the measured birefringence of both 2D perovskites (c).

experimental limit, we uncover moderately broadband 2D perovskite THz anisotropy with frequency-dependent birefringence ranging from weak to very strong ($\Delta n \approx 0.25$, $\Delta k \approx 0.5$) and arising in the primarily inorganic phonon region (Figure 4.5c). These exciting results immediately hold fascinating implications for

how THz anisotropy is energetically localized in these perovskite systems, as well as revealing possibilities for tuning this birefringence. In fact, the ligand dependence of the THz anisotropy shows an interesting reverse in the expected blue shift frequency trend described in Chapter 3.6.2. Specifically, we find the strongest birefringence located in phonon modes with slightly higher frequencies than the characteristic ~2 THz excitations. While the phonon excitations at normal incidence trend in frequency according to inoranic lattice stiffness imposed by the ligands, the anisotropy peaks trend in the opposite direction. We hypothesize that the highly directional phonon modes associated with these anisotropic peaks hold both inorganic and organic vibrational character in such a way as to orient the transition dipoles more parallel to the perovskite plane. The increased orthogonality of the phonon transition dipoles would reduce their excitation probability from an oblique incidence beam. Furthermore, we expect that THz-excited phonons travelling out-of-plane should encounter more scattering events off ligand-lattice interfaces than in-plane phonons, which could help explain the large anisotropic reductions in the imaginary refractive index.[5] A more focused theoretical study characterizing these directionally isolated ~2.5 THz modes would improve our understanding of their impact on charge carrier – phonon coupling. Such theoretical investigation could also improve understanding about how the anisotropic peak frequency shifts with organic ligand environment. Nevertheless, it is thanks to the development of our THz spectrometer and the high quality samples that we are able to resolve these intriguing, ligand-dependent anisotropic excitations which would otherwise be particularly challenging to capture in such thin films.

We can examine out-of-plane lattice dynamics in n = 1 layered perovskites even further, though, with work done on the lower energy phonons conducting thermal transport. Li et al., for instance, provide valuable insights from revealing "remarkably weak" anisotropy in thermal conductivity measurements of exfoliated BA_2PbI_4 single crystals.[5] Thermal conductivity is proportionate to the material heat capacity, phonon lifetime, and the square of average phonon group velocity. In this context, Li et al. discuss how weak interlayer bonding in BA_2PbI_4 leads to higher out-of-plane phonon scattering and, consequently, shorter out-of-plane phonon lifetimes than phonons traveling in-plane. However, preferentially out-of-plane ligand bond alignment leads to compensating phonon group velocities that, along with the large volume of organic ligand, act to reduce thermal conduction anisotropy. Li et al. describe these competing phonon effects as originating from both acoustic and optical phonons that reach frequencies as high as 0.5 THz. We thus also suspect that these low frequency BA_2PbI_4 optical phonons similarly exhibit orthogonal atomic motions which facilitate polarization-insensitive transition dipole excitations at oblique incidences to further weaken thermal conduction anisotropy. Regardless, Li et al. report a 1.5 anisotropic ratio (e.g., $\tilde{n}_{in-plane}/\tilde{n}_{out-of-plane}$) of thermal conductivity for this 2D perovskite single crystal. Given that we observe similar magnitude anisotropic ratios (not shown) for slightly our higher optical phonons, we speculate that these out-of-plane phonon transport effects reported by Li et al. may also impact the THz vibrational dynamics in our data. Together, the thermal conductivity and THz optical parameters paint a

cohesive picture of the low and high frequency phonon excitation anisotropy in n = 1 layered perovskites.

From oblique incidence THz transmission, we capture, with unprecedented clarity, characteristic far-infrared phonon modes crucial to layered hybrid perovskite excited-state dynamics.[6-15] We directly measure out-of-plane THz lattice dynamics in 2D perovskites for the first time to reveal interesting THz anisotropic behavior mediated by orthogonal excitations within the flexible 2D perovskite architecture. We find particularly strong anisotropy in primarily inorganic phonons associated with excited-state coupling that could hold deep implications regarding the fundamental nature of anisotropic 2D perovskite charge transport. While our results were captured from Ruddlesden-Popper phase layered perovskites, we anticipate similar behavior existing in the increasingly popular Dion-Jacobsen phase systems.[22] It is also worth noting that in-plane Raman anisotropy has been observed in single crystal layered perovskites.[23] Although our measurements were insensitive to this behavior, as previously discussed, exploring any in-plane THz anisotropy on large area single crystals would be a viable route towards fully characterizing the critical lattice dynamics of layered perovskite materials. Fundamentally understanding such unique properties is vital for effective hybrid perovskite development, so that we can deliver on their massive potential for low-cost, sustainable electronics.

CHAPTER 4 BIBLIOGRAPHY

1. Li, X.; Hoffman, J. M.; Kanatzidis, M. G. The 2D Halide Perovskite Rulebook: How the Spacer Influences Everything from the Structure to Optoelectronic Device Efficiency. *Chem. Rev.* **2021**, *121* (4), 2230–2291. https://doi.org/10.1021/acs.chemrev.0c01006.

2. Xiao, B.; Sun, Q.; Wang, F.; Wang, S.; Zhang, B.-B.; Wang, J.; Jie, W.; Sellin, P.; Xu, Y. Towards Superior X-Ray Detection Performance of Two-Dimensional Halide Perovskite Crystals by Adjusting the Anisotropic Transport Behavior. *J. Mater. Chem. A* **2021**, *9* (22), 13209–13219. https://doi.org/10.1039/D1TA02918E.

3. Lu, L.; Weng, W.; Ma, Y.; Liu, Y.; Han, S.; Liu, X.; Xu, H.; Lin, W.; Sun, Z.; Luo, J. Anisotropy in a 2D Perovskite Ferroelectric Drives Self-Powered Polarization-Sensitive Photoresponse for Ultraviolet Solar-Blind Polarized-Light Detection. *Angew. Chemie Int. Ed.* **2022**, *61* (26). https://doi.org/10.1002/anie.202205030.

4. Li, J.; Ma, J.; Cheng, X.; Liu, Z.; Chen, Y.; Li, D. Anisotropy of Excitons in Two-Dimensional Perovskite Crystals. *ACS Nano* **2020**, *14* (2), 2156–2161. https://doi.org/10.1021/acsnano.9b08975.

5. Li, C.; Ma, H.; Li, T.; Dai, J.; Rasel, M. A. J.; Mattoni, A.; Alatas, A.; Thomas, M. G.; Rouse, Z. W.; Shragai, A.; Baker, S. P.; Ramshaw, B. J.; Feser, J. P.; Mitzi, D. B.; Tian, Z. Remarkably Weak Anisotropy in Thermal Conductivity of Two-Dimensional Hybrid Perovskite Butylammonium Lead Iodide Crystals. *Nano Lett.* **2021**, *21* (9), 3708–3714. https://doi.org/10.1021/acs.nanolett.0c04550.

6. Li, J.; Lu, G.; Xie, H.; Jiang, X.; Fang, Z.; Zeng, Y.-J.; He, H.; Ye, Z. Effect of Electron–Phonon Coupling on the Color Purity of Two-Dimensional Ruddlesden–Popper Hybrid Lead Iodide Perovskites. *J. Phys. Chem. C* **2023**, *127* (13), 6380–6388. https://doi.org/10.1021/acs.jpcc.2c08609.

7. Kim, K.; Vetter, E.; Yan, L.; Yang, C.; Wang, Z.; Sun, R.; Yang, Y.; Comstock, A. H.; Li, X.; Zhou, J.; Zhang, L.; You, W.; Sun, D.; Liu, J. Chiral-Phonon-Activated Spin Seebeck Effect. *Nat. Mater.* **2023**, *22* (3), 322–328. https://doi.org/10.1038/s41563-023-01473-9.

8. Mauck, C. M.; France-Lanord, A.; Hernandez Oendra, A. C.; Dahod, N. S.; Grossman, J. C.; Tisdale, W. A. Inorganic Cage Motion Dominates Excited-

State Dynamics in 2D-Layered Perovskites (C x H 2 x +1 NH 3) 2 PbI 4 (x = 4–9). *J. Phys. Chem. C* **2019**, *123* (45), 27904–27916. https://doi.org/10.1021/acs.jpcc.9b07933.

9. Fu, J.; Li, M.; Solanki, A.; Xu, Q.; Lekina, Y.; Ramesh, S.; Shen, Z. X.; Sum, T. C. Electronic States Modulation by Coherent Optical Phonons in 2D Halide Perovskites. *Adv. Mater.* **2021**, *33* (11). https://doi.org/10.1002/adma.202006233.

10. Quan, L. N.; Park, Y.; Guo, P.; Gao, M.; Jin, J.; Huang, J.; Copper, J. K.; Schwartzberg, A.; Schaller, R.; Limmer, D. T.; Yang, P. Vibrational Relaxation Dynamics in Layered Perovskite Quantum Wells. *Proc. Natl. Acad. Sci.* **2021**, *118* (25). https://doi.org/10.1073/pnas.2104425118.

11. Duan, H.-G.; Tiwari, V.; Jha, A.; Berdiyorov, G. R.; Akimov, A.; Vendrell, O.; Nayak, P. K.; Snaith, H. J.; Thorwart, M.; Li, Z.; Madjet, M. E.; Miller, R. J. D. Photoinduced Vibrations Drive Ultrafast Structural Distortion in Lead Halide Perovskite. *J. Am. Chem. Soc.* **2020**, *142* (39), 16569–16578. https://doi.org/10.1021/jacs.0c03970.

12. Thouin, F.; Valverde-Chávez, D. A.; Quarti, C.; Cortecchia, D.; Bargigia, I.; Beljonne, D.; Petrozza, A.; Silva, C.; Srimath Kandada, A. R. Phonon Coherences Reveal the Polaronic Character of Excitons in Two-Dimensional Lead Halide Perovskites. *Nat. Mater.* **2019**, *18* (4), 349–356. https://doi.org/10.1038/s41563-018-0262-7.

13. Bourelle, S. A.; Camargo, F. V. A.; Ghosh, S.; Neumann, T.; van de Goor, T. W. J.; Shivanna, R.; Winkler, T.; Cerullo, G.; Deschler, F. Optical Control of Exciton Spin Dynamics in Layered Metal Halide Perovskites via Polaronic State Formation. *Nat. Commun.* **2022**, *13* (1), 3320. https://doi.org/10.1038/s41467-022-30953-w.

14. Herz, L. M. How Lattice Dynamics Moderate the Electronic Properties of Metal-Halide Perovskites. *J. Phys. Chem. Lett.* **2018**, *9* (23), 6853–6863. https://doi.org/10.1021/acs.jpclett.8b02811.

15. Ruan, Z.; Jiang, S.; Zhang, Q.; Luo, Y. Phononic Fine-Tuning in a Prototype Two-Dimensional Hybrid Organic–Inorganic Perovskite System. *J. Phys. Chem. Lett.* **2022**, *13* (24), 5480–5487. https://doi.org/10.1021/acs.jpclett.2c01290.

16. Seitz, M.; Magdaleno, A. J.; Alcázar-Cano, N.; Meléndez, M.; Lubbers, T. J.; Walraven, S. W.; Pakdel, S.; Prada, E.; Delgado-Buscalioni, R.; Prins, F. Exciton Diffusion in Two-Dimensional Metal-Halide Perovskites. *Nat. Commun.* **2020**, *11* (1), 2035. https://doi.org/10.1038/s41467-020-15882-w.

17. Sendner, M.; Nayak, P. K.; Egger, D. A.; Beck, S.; Müller, C.; Epding, B.; Kowalsky, W.; Kronik, L.; Snaith, H. J.; Pucci, A.; Lovrinčić, R. Optical Phonons in Methylammonium Lead Halide Perovskites and Implications for Charge Transport. *Mater. Horizons* **2016**, *3* (6), 613–620. https://doi.org/10.1039/C6MH00275G.

18. Pérez-Osorio, M. A.; Milot, R. L.; Filip, M. R.; Patel, J. B.; Herz, L. M.; Johnston, M. B.; Giustino, F. Vibrational Properties of the Organic–Inorganic Halide Perovskite CH 3 NH 3 PbI 3 from Theory and Experiment: Factor Group Analysis, First-Principles Calculations, and Low-Temperature Infrared Spectra. *J. Phys. Chem. C* **2015**, *119* (46), 25703–25718. https://doi.org/10.1021/acs.jpcc.5b07432.

19. Oughstun, K. E.; Palombini, C. L. Fresnel Reflection and Transmission Coefficients for Temporally Dispersive Attenuative Media. *Radio Sci.* **2018**, *53* (11), 1382–1397. https://doi.org/10.1029/2018RS006646.

20. Chen, Y.; Mahata, A.; Lubio, A. D.; Cinquino, M.; Coriolano, A.; Skokan, L.; Jeong, Y.; Razzari, L.; De Marco, L.; Ruediger, A.; De Angelis, F.; Colella, S.; Orgiu, E. Phonon Analysis of 2D Organic-Halide Perovskites in the Low- and Mid-IR Region. *Adv. Opt. Mater.* **2022**, *10* (16). https://doi.org/10.1002/adom.202100439.

21. Zeng, Z.; Mavrona, E.; Sacré, D.; Kummer, N.; Cao, J.; Müller, L. A. E.; Hack, E.; Zolliker, P.; Nyström, G. Terahertz Birefringent Biomimetic Aerogels Based on Cellulose Nanofibers and Conductive Nanomaterials. *ACS Nano* **2021**, *15* (4), 7451–7462. https://doi.org/10.1021/acsnano.1c00856.

22. Zhang, F.; Park, S. Y.; Yao, C.; Lu, H.; Dunfield, S. P.; Xiao, C.; Uličná, S.; Zhao, X.; Du Hill, L.; Chen, X.; Wang, X.; Mundt, L. E.; Stone, K. H.; Schelhas, L. T.; Teeter, G.; Parkin, S.; Ratcliff, E. L.; Loo, Y.-L.; Berry, J. J.; Beard, M. C.; Yan, Y.; Larson, B. W.; Zhu, K. Metastable Dion-Jacobson 2D Structure Enables Efficient and Stable Perovskite Solar Cells. *Science* **2022**, *375* (6576), 71–76. https://doi.org/10.1126/science.abj2637.

23. Dhanabalan, B.; Leng, Y.-C.; Biffi, G.; Lin, M.-L.; Tan, P.-H.; Infante, I.; Manna, L.; Arciniegas, M. P.; Krahne, R. Directional Anisotropy of the Vibrational Modes in 2D-Layered Perovskites. *ACS Nano* **2020**, *14* (4), 4689–4697. https://doi.org/10.1021/acsnano.0c00435.

Chapter 5

CONCLUSIONS

In this work, a state-of-the-art terahertz spectrometer was constructed and applied towards novel investigations of strongly coupled lattice dynamics in hybrid perovskite thin films. Terahertz pulses were generated by custom fabricated spintronic THz emitters, samples were configured in 3D printed precise rotation mounts, and the signal was detected through air-biased coherent detection. The THz spectrometer was shown to be capable of ultrabroadband detection with polarization-sensitivity at arbitrary angles of incidence onto a transmissive sample. Careful implementation of generalized transfer functions provided accurate material parameter extraction from complex multilayer systems like 2D perovskite thin films which exhibit strong THz absorbance. Optimized perovskite thin film quality was achieved after screening a wide variety of spin coating conditions and it was shown that ideal synthetic environment was dependent on perovskite composition. In developing better methods to study thin film THz transmission, we perform novel characterization of high tensile strength 100 nm silicon nitride windows and demonstrate enhanced THz detection for all perovskite samples when coated onto these substrates. An original THz study into the vibrational anisotropy of 2D perovskites was then performed using polarization-sensitive, oblique incidence THz transmission. We extracted THz material parameters polarized both parallel and perpendicular to the perovskite layers and calculate the broadband THz birefringence

for quantitative analysis. We discovered strong THz anisotropy localized in the vibrational modes dominated by the inorganic lattice with moderate to weak anisotropy elsewhere. The direction-dependent lattice dynamics were attributed to higher scattering of phonons traveling through the inorganic lattice – organic ligand interfaces, which explained the weakened absorptivity of the out-of-plane THz response. Our results hold deep implications for the previously elusive nature of out-of-plane electron-phonon coupling in 2D hybrid perovskites. Overall, our experiments demonstrate the powerful utility of oblique incidence THz TDS to interrogate sensitive anisotropic media like 2D materials and layered systems.

Appendix A

NOTES FOR AIR-BIASED COHERENT DETECTION SETUP

The following notes are derived from personal experience constructing an ABCD module after helpful discussions with Dr. Yoann Jestin. Both sections A.1 and A.2 can be used to consistently transition the detection mode of our THz spectrometer back to ABCD after, for instance, employing an electro-optic sampling scheme with ZnTe crystal.

A.1 Alignment of terahertz induced second harmonic (TFISH) generation

As described in section 2.5.2, terahertz induced second harmonic generation is the upconversion of an optical (e.g., ~800 nm) probe pulse when a temporally and spatially overlapped THz pulse causes transient anisotropy of the interaction medium. We use TFISH signal to optimize the THz – optical probe overlap before installation of the ABCD electrodes. First, the alignment and focusing of the THz beam is tuned, which in our case was exclusively handled by gold- or silver-coated mirrors with flat and off-axis parabolic (OAP) geometry. While the preceding THz beam alignment will strongly impact the strength of the THz detection, the THz focus at the optical probe overlap position is the most critical. Quality of the THz focusing can often be correlated to the quality of optical focusing through the THz beam path, for example if the THz emitter and optical beam block are removed from the path.

Both low and high fluence of the optical pump beam were used in the THz line to tune the THz optics for nicely centered pointing and optimal focusing. Due to the high photon energy and intense peak field strength of the 800 nm optical probe pulse, an air-based plasma will easily spark at the focal point of an OAP mirror which provides direct visualization of the focusing quality. It is extremely important, however, to consider appropriate safety measures when working with free space laser beams of any frequency, and especially so when intentionally sparking air-based plasmas. As with all laser safety, optical safety glasses and non-reflective attire are particularly vital. Low optical pump pulse energies of ~100 μJ or less are used to optimize the THz line into the final OAP mirror and subsequently down through the focal point. Optical pump energies as high as 0.5 mJ were used to tune the focusing quality by checking for any aberrations to the circular beam shape going through the focus. A step-by-step overview of the TFISH alignment process is provided below.

S1. Designate the beam height and path along the optical table grid for spatial and temporal overlap of the THz and probe pulses. Align the collimated optical probe beam along that path, with the assistance of irises, before adding the converging lens to focus the probe down at the pre-determined overlap position. It is extremely helpful to mount the converging lens on a three-axis translation stage to easily adjust the x-, y-, and z-direction of the probe pointing for small adjustments in the future. A diverging lens after the probe focus is often used to re-collimate the probe beam for convenient detection by, for example, a photodiode.

S2. Install the final THz OAP mirror so that the empty through-hole is centered on the optical probe beam, thus ensuring the correct height of the THz beam line. Remove the THz emitter, optical beam block, and any other THz optics from the THz beam path. Use a low optical pump energy (~100 µJ or less) and the same irises from S1 to set the THz beam along the pre-designated path. Match the focal positions of the THz beam and optical probe.

S3. Iterate between a high optical pump energy (~0.5 mJ) and low pump energy to tune the quality and position of the THz path focus, respectively, slightly adjusting/moving the last OAP mirror as necessary. The nicely collimated optical pump beam (from the unblocked THz line) should enter the OAP mirror and symmetrically converge down to a sharp focal point before symmetrically diverging afterwards. The focusing behavior of a misaligned OAP mirror can be diagnostic to the type of error. Horizontal mirror pointing error, for example, will cause the optical pump beam to preferentially focus down to a line shape directed along a horizontal or vertical axis relative to the optical table. Vertical mirror pointing errors will lead to beam focusing line shapes preferentially aligned diagonally between the horizontal and vertical beam axes, relative to the optical table.

S4. Using a low pulse energy for both the optical pump and probe beams, take a white card and check the spatial overlap. The two spots should focus on the same position along the optical path, overlap at the same point in space, and ideally follow collinear paths. If only slightly misaligned (<0.5 mm), either the probe lens or THz OAP knobs

can be adjusted. If large alignment error is present, move the position of the last OAP mirror and repeat S3. Once set, do not move the THz OAP mirror after this point. Critically, ensure that the THz and probe polarizations are parallel to one another for strongest TFISH generation.

S5. Install an appropriate photodiode (PD) or photomultiplier tube (PMT) for the relevant upconverted signal beam (e.g., ~400 nm in our case), add an optical filter to isolate the upconverted frequencies, and re-install the THz generation optics. If using a lock-in amplifier, employ an optical chopper to either the THz or probe line.

S6. Scan for temporal overlap between THz and optical probe with the measurement chamber under inert atmosphere and probe energies as low as 100 µJ to start. The advantage of TFISH is that increasing optical probe energy (e.g., above 100 µJ) will strengthen the resulting THz signal to aid the search for temporal overlap. Arbitrarily high probe energy can be used as long as the noise is sufficiently low on the upconverted light detector. Once the THz signal is acquired, tune up the peak power by very slightly adjusting the probe pointing through the converging lens.

The TFISH signal can be further optimized by reducing the optical probe power and continuing to adjust the probe pointing. Once maximum peak power is achieved, the electrodes can be installed for air biased coherent detection. If having difficulty with the TFISH alignment, it is recommended to adjust the overlap first through a more conventional detection scheme like electro-optic sampling and then go through the above steps using that alignment.

A.2 Electrode installation and biasing

With the spatial and temporal overlap between the THz and optical probe tuned, no further adjustment to the optical lines should be necessary. We proceed with the remaining steps to implement our ABCD setup.

S7. Remove the optical chopper and mount the electrodes so that the air gap between them is centered around the focal point of the final OAP mirror, and so the polarization of the THz field is parallel to the voltage bias direction. In other words, align the electrodes so that the direction across the free space gap matches the THz polarization. Furthermore, adjust or pre-set the distance between the two electrodes such that the voltage bias in the gap is close to 20 kV/cm, which is near the breakdown voltage of air (and nitrogen). Safety practices with high voltage electronics must be exercised and be cautious not to induce arcs between the electrodes. Also be careful not to damage the electrodes by focusing the optical probe beam down onto them.

S8. Connect the electrodes to the voltage source and power on the supply while both the THz and optical probe are blocked. The voltage bias should be delivered to the electrodes as an alternating bipolar square wave whose frequency is taken from the laser source. In our case, in the absence of an appropriate waveform generator, the TTL signal from our amplified laser system was first filtered to remove the DC offset (e.g., 0 – +5 V $\rightarrow$ -2.5 – +2.5 V) before amplification up to +/- 100 V (200 V$_{\text{peak-to-}}$

$_{peak}$). As with considering intense lasers, extreme caution should always be performed when dealing with high voltage experiments.

S9. Unblock the THz and probe beams. Scan the time-axis to capture the now heterodyned THz time-domain signal. Adjust the relative sensitivity of the PD or PMT, as well as the optical probe power, to maximize the signal-to-noise and dynamic range of the spectra.

Given a high voltage amplifier, for instance ~1 kV, the electrode air gap would be wide enough to keep the electrodes in place during the TFISH alignment. For maximum accuracy, it is recommended to optimize the THz peak intensity and bandwidth before any critical scans by adjusting the probe pointing only. Over month-long time scales, re-tuning the THz focusing quality through steps S2 – S4 can also be valuable.

A p p e n d i x   B

NOTES FOR THZ-TDS DATA PROCESSING

This section acts as a guide for constructing and understanding THz time-domain processing algorithms. At time of submission, the Python programs written for this thesis work are prohibitively specialized for data pipelines from the Blake lab spectrometer. It is thus more instructive to walk through the general functions necessary for successful material parameter extraction. Below are some suggested steps used to turn raw time-domain spectra (TDS) into frequency-domain refractive index spectra, but the exact order or nature of the program can be variable depending on computational demands. In our work, there were three general scripts for data processing. One to turn raw TDS into polished frequency-domain spectra (FDS), one to calculate frequency-domain transmission spectra and fit them, and another to house most of the functions implemented by the first two scripts. We begin with the code to convert TDS into FDS.

C1. Assign values to processing variables like reference and sample filenames, length of time-domain spectra padding, type and length of time-domain windowing, and relevant THz data frequency range.

C2. Load the time-domain scans of the reference and sample as independent dataset arrays or matrices.

C3. Remove any DC offset error from each time-domain scan. For instance, subtract the amplitude of the noise floor without THz signal from each scan to ensure that no THz signal is equivalent to zero amplitude TDS.

C4 (optional). Interpolate all spectra onto uniform time-axis with desired temporal length from zero padding (as described in section 2.6.2). We commonly use a time-axis padded out to 50 picoseconds with a 2 femtosecond step size. Phase error from delay line jitter can then be minimized by shifting all scans of the same dataset to a consistent temporal position (for example, shifting all reference scans to the maximum positive peak position of the first reference scan).

C5 (optional). If calibration is available for absolute phase shift between reference sample spectra, move all sample scans away from the designated reference feature with that predefined temporal distance. For example, if the calibration was measured from the distance between the maximum positive peaks of the reference and sample time-domain THz pulses, shift the raw time-domain scans with that distance between the same maximum positive peaks.

C6. Average all TDS of the same dataset together to form the averaged reference and sample traces. Optionally, take the standard deviation of each dataset for time-domain signal-to-noise (SNR) and dynamic range (DNR) calculations.

C7. Apply the windowing function to the averaged TDS so that the edges of the window fall to zero amplitude away from all relevant signal features. We most often implement the Tukey windowing function.

C8. Take the Fourier transform of the time-domain spectra and optionally normalize the sample frequency-domain spectra with the reference spectra.

C9 (optional). Fourier transform all the scans in the dataset to acquire the frequency-domain standard deviations for SNR and DNR calculations.

C10. Save the time-domain spectra and then the frequency-domain spectra at relevant bandwidths above the noise floor.

At this stage, we next employ the script to convert FDS into extracted material parameters.

C11. We again assign values to necessary and helpful parameters, such as sample thickness, fit initial guess, THz polarization, incidence angle, desired frequency range to fit over, and more.

C12. Load FDS of sample and reference, as well as refractive index data of the reference if it represents the sample's substrate.

C13. Acquire the sample transmission spectrum by taking the division of the sample FDS by the reference FDS.

C14. Obtain the transmission amplitude by taking the absolute value of the transmission spectrum from C13, which should be complex-valued. Obtain the transmission phase offset by taking the argument (e.g., arctan(transmission spectrum)). Unwrap the argument to avoid phase jumps in the output fit. If necessary, subtract off any low-frequency phase jumps which are a multiple of 2π. For more information, follow the phase processing tutorial mentioned in section 2.6.4.

C15. If applicable, apply analytical function to directly extract refractive index values as mentioned in section 2.7.1. Otherwise, iteratively apply numerical fitting at each frequency point as described in section 2.7.2.

C16. Different thicknesses and initial refractive index guesses will significantly impact the fitting efficiency and, potentially, the accuracy. Tune these parameters to optimize final data extraction before saving material parameter solutions.